ENGINEERING LOCALIZED SURFACE PLASMONS IN DOPED SEMICONDUCTOR NANOMATERIALS

A Dissertation
Presented to
The Academic Faculty

by

Dmitriy Boyuk

In Partial Fulfillment
of the Requirements for the Degree
Chemical Engineering PhD in the
School of Chemical and Biomolecular Engineering

Georgia Institute of Technology
August 2018

ENGINEERING LOCALIZED SURFACE PLASMONS IN DOPED SEMICONDUCTOR NANOMATERIALS

Approved by:

Dr. Michael A. Filler, Advisor
School of Chemical & Biomolecular Engineering
Georgia Institute of Technology

Dr. Chris Jones
School of Chemical & Biomolecular Engineering
Georgia Institute of Technology

Dr. Paul Kohl
School of Chemical & Biomolecular Engineering
Georgia Institute of Technology

Dr. Younan Xia
School of Chemistry
Georgia Institute of Technology

Dr. Wenshan Cai
School of Electrical & Computer Engineering
Georgia Institute of Technology

Date Approved: May 11, 2018

ACKNOWLEDGEMENTS

Foremost, I would like to thank my advisor, Dr. Michael Filler, for his inspiration early in my academic career and his support throughout the process of my graduate studies. I also recognize my committee members, Dr. Paul Kohl, Dr. Chris Jones, Dr. Wenshan Cai, and Dr. Younan Xia for their excellent feedback and support throughout the stages of my graduate studies. My research projects and dissertation improved tremendously as a result.

I would like to acknowledge the School of Chemical & Biomolecular Engineering at Georgia Institute of Technology, the National Science Foundation, and Institute for Electronics and Nanotechnology (IEN) for their support of my research studies. Specifically, I would like to thank Mr. Eric Woods, Mr. John Pham, Dr. Chris Yang, Mr. Tran-Vinh Nguyen, and Mr. Dean C. Sutter of IEN their technical assistance, training and support. Finally, I would like to thank all my family members for their support.

I owe a great deal of my success to the training and assistance by Filler group alumni: Dr. Li-Wei Chou, Dr. Nae Chul Shin, Dr. Ildar Musin, Dr. Saujan Siverem and Dr. Ho Yee Hui. I am thankful to all the Filler lab members I had the pleasure of working with throughout my PhD studies for creating a collaborative and pleasant work environment within the lab. Specially, would like to recognize Amar Mohabir and Gozde Tutuncuoglu for their friendship and support during the best and hardest times of my academic career. Lastly, I would like to thank my family for their love and support.

TABLE OF CONTENTS

CHAPTER 5.
Concluding Remarks

LIST OF FIGURES

LIST OF SYMBOLS AND ABBREVIATIONS

LSPR	Localized Surface Plasmon Resonance
SP	Surface Plasmon
EM	Electromagnetic
FE	Field Enhancement
DDA	Discrete Dipole Approximation
FDTD	Finite Difference Time Domain
NW	Nanowire
NC	Nanocrystal
CQD	Colloidal Quantum Dot
VLS	Vapor-Liquid-Solid
TEM	Transmission Electron Microscope
SEM	Scanning Electron Microscope
AFM	Atomic Force Microscope
UHV	Ultra-High Vacuum
ALD	Atomic Layer Deposition
CVD	Chemical Vapor Deposition

SUMMARY

The field of plasmonics has developed over the past two decades with noble metals as the primary platform of investigation. Localized surface plasmon resonances (LSPRs) supported by metal nanoparticles enable a myriad of technology applications. However, the utility of noble metal plasmonic materials is currently beset by their fixed dielectric properties, high cost and strong plasmon decay. Recently, extrinsically doped semiconductors have emerged as alternative plasmonic materials and open the door to new opportunities for mitigating plasmonic losses and harnessing infrared LSPRs in applications such as photodetection, optical interconnects, and chemical sensing. This dissertation begins with an overview of the surface plasmon phenomenon, followed by a discussion of the key plasmonic semiconductor nanomaterials and their associated challenges.

In Chapter 2, we show the impact of axially carrier density gradients on the spectral response of Si nanowires containing multiple resonators. Spatial control of carrier density is critical for engineering and exploring the interactions of localized surface plasmon resonances (LSPRs) in nanoscale semiconductors. Here, we couple *in situ* infrared spectral response measurements and discrete dipole approximation (DDA) calculations to show the impact of axially graded carrier density profiles on the optical properties of mid-infrared LSPRs supported by Si nanowires synthesized by the vapor-liquid-solid technique. The region immediately adjacent to each intentionally encoded resonator (*i.e.*, doped segment) can exhibit residual carrier densities as high as 10^{20} cm^{-3}, which strongly modifies both near- and far-field behavior. Lowering substrate

temperature during the spacer segment growth reduces this residual carrier density and results in a spectral response that is indistinguishable from nanowires with ideal, atomically abrupt carrier density profiles. Our experiments have important implications for the control of near-field plasmonic phenomena in semiconductor nanowires; they demonstrate methods for determining and controlling axial dopant profile within these systems.

In Chapter 3, we first demonstrate that embedding resonators in an anisotropic dielectric with a large permittivity can dramatically increase the LSPR coupling interaction strength and thereby, plasmonic spectral extinction and near-field intensity. We experimentally demonstrate this effect with Si nanowires containing two phosphorus-doped segments. The near-field decay length scaling factor is extracted from *in situ* infrared spectral response measurements using the "plasmon ruler" equation, and found to be ~4-5x larger than for the same resonators in isotropic vacuum or Si. Discrete dipole approximation (DDA) calculations support the observed coupling behavior for nanowires and show how it is affected by the resonator geometry, carrier density, and embedding material (*e.g.*, Si, Ge, GaAs, etc.). Our findings demonstrate that equivalent near-field interactions are achievable with a smaller total volume and at increased resonator spacing, offering new opportunities to engineer plasmon-based chemical sensors, catalysts, and waveguides.

Lastly in Chapter 4, we first demonstrate infrared photoconductivity within the Al_2O_3 coated ITO nanocrystal films. Our results suggest a direct relationship between infrared photocurrent in these materials and LSPR absorption in the same regime. Measurements using a broadband infrared source and a voltage bias of 10V, yield a

responsivity of 15 A/W and a detectivity of 1.2×10^8 $cmHz^{1/2}W^{-1}$. Remarkably, these films reliably sustain these photoconductive performance figures over months in ambient and prolonged time under electrical stress. Our results underline infrared LSPR absorption of doped semiconductor nanocrystals a promising alternative strategy for developing next generation infrared optoelectronic materials and technology.

CHAPTER 1. DOPED SEMICONDUCTOR PLASMONICS INTRODUCTION & BACKGROUND

1.1 Localized surface plasmon resonance phenomenon

1.1.1 Surface plasmon subwavelength confinement

The unique optical properties of metallic nanoparticles have fascinated scientist and philosophers from the Bronze Age to modern times. The stained glass of med-evil cathedrals derives its vibrant color from the interactions of metallic nanoparticles with light. Noble metal particles such as gold (Au), silver (Ag), copper (Cu), and aluminum (Al) have long been known to scatter light in the UV-visible region of the spectrum.[1] This unique optical response of metals, as well as their thermal and electrical conductivity, all stem from the large free carrier (electron) density available in these materials.

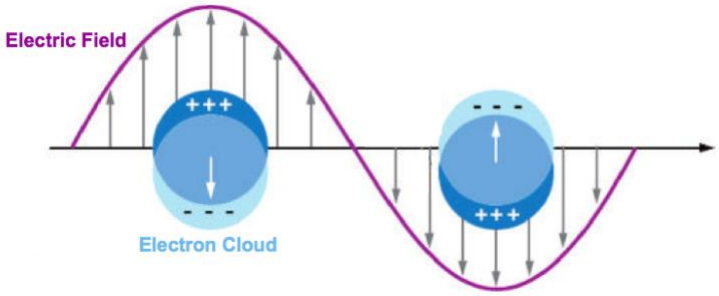

Figure 1.1. Localized surface plasmon resonance schematic where the free conduction electrons of a metal are excited into collective oscillation via coupling of incident light. Adapted from 4 and reprinted with permission.

Bulk metallic materials exhibit resonant collective free electron density oscillations at the metal-dielectric interface in response to an oscillating electric field referred to as surface plasmons.[2] These resonant modes arise at the surface boundary of

metallic material by effectively coupling the electric field of the incident electromagnetic (EM) wave to the internal degrees of freedom of the free charge carrier density.[2, 3] When electromagnetic wave strikes a subwavelength metallic particle with a diameter much smaller than the wavelength of the incident wave, the free carrier (electron) density is collectively subject to the force of the EM wave's electric field. The kinetic motion of free carriers in a surface plasmon oscillation results in a subwavelength confinement of optical modes at the nanoscale. Furthermore, at resonance, the surface plasmon oscillation strongly concentrates the diffuse electric field in EM waves into a subwavelength volume at the metal particle interfaces. The fundamentals of diffraction dictate that the propagation of light is obstructed when dimensions of the optical components become on the order of the wavelength of light. Surface plasmon oscillation modes, supported by subwavelength metallic objects, stem from an entirely distinct physical phenomenon. Optical radiation is strongly coupled to a localized field and can thereby surpass the diffraction limitations down to a single nanometer scale. Being able to squeeze light in to sub-wavelength volumes promises new opportunities for synergetic integration of propagating light and nanoscale devices. The plasmonic functionality of metallic nanomaterials is of interest in any application where sub-wavelength confinement is desired.[4] This resonant optical response of metallic nanomaterials is referred to as localized surface plasmon resonance (LSPR) and is the subject threading the investigations outlined in this dissertation. [5]

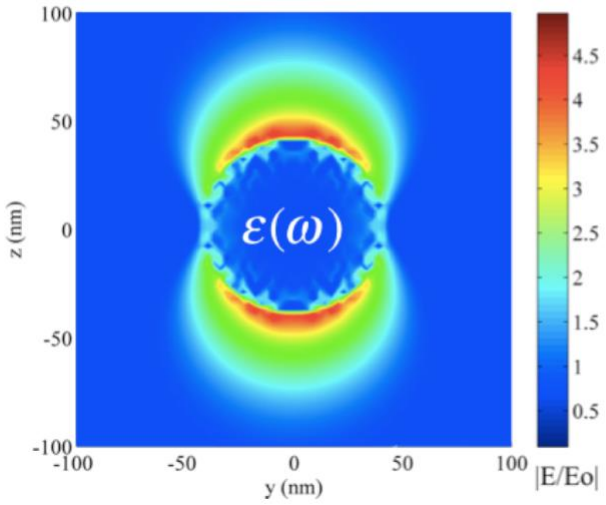

Figure 1.2 Electric field enhancement cross-section calculated using the discrete approximation simulation method for a 100 nm diameter Au sphere at the surface plasmon resonance excitation frequency.

1.1.2 The Drude model of permittivity

Gustav Mie first derived the electromagnetic scattering properties a spherical metal particle in 1908 and the theory was later extended to spheroid and cylindrical geometries. Collective charge density wave oscillation at a material surface, known as surface plasmons, are a direct result of free charge carrier density of a material. It is important to note that the collective vibrations of a crystal lattice, referred to as surface phonons, produce analogous oscillation behavior with lower resonance energies, typically in the far-infrared. The Drude model provides a simple and useful framework to understand electrical conductivity, and parameters governing the plasmon resonance phenomenon.[2,6]

The Drude response of conduction electrons of a metal can be described within the general Lorentz oscillator equation motion for a resonator as shown in equation 1.

$$\varepsilon(\omega) = \varepsilon_b \left(1 - \frac{\omega_p^2}{\omega_o^2 - \omega^2 + i\omega\gamma(\omega)}\right) \quad (1)$$

$$\omega_p = \sqrt{\frac{Ne^2}{\varepsilon_o m^*}} \quad (2)$$

ω_p is defined the bulk plasmon frequency, which determines the amplitude of oscillation and is expressed in terms of the free carrier density *N*, elementary charge -*e*, the permittivity of free space ε_o, and the effective carrier mass m^*. Furthermore, ε_b is the background dielectric permittivity and ω, ω_o, γ represent the frequency of oscillation, central frequency and damping rate of the resonator, respectively. By setting the resonator restoring force to zero ($\omega_o = 0$) in equation 1, we obtain a simplified Drude model representation of metal permittivity, which can be further separated into its real and imaginary components as shown in equations 3 – 5.

$$\varepsilon_m(\omega) = \varepsilon'_m(\omega) + i\varepsilon''_m(\omega) = \varepsilon_b \left(1 - \frac{\omega_p^2}{\omega^2 + i\omega\gamma}\right) \quad (3)$$

$$\varepsilon'_m(\omega) = \varepsilon_b \left(1 - \frac{\omega_p^2}{\omega^2 + \gamma^2}\right) \quad (4)$$

$$\varepsilon''_m(\omega) = \frac{\varepsilon_b \omega_p^2 \gamma}{\omega(\omega^2 + \gamma^2)} \quad (5)$$

Here, we assume that the free carriers of a material can be described well using just the effective mass m^* and an electron charge unit *e*. We additionally assume that the free carrier scattering rate g is defined for a specific material independent of the oscillation frequency ω.

The oscillating plasmonic motion of free charge carriers and the resulting polarizability in response to the external oscillating electric field has been shown to be well represented by the Drude model as outline above. In the spectral region where $\omega < \omega_p$, the $\mathcal{G}$ term is generally much smaller than ω and therefore, the magnitude of the real part of the dielectric function can take on large negative values. A whole range of plasmonic optical properties arise at the intersection of (i) large negative real permittivity and (ii) small imaginary permittivity conditions for metallic material. Most common highly conductive metals (i.e Au, Ag) satisfy these permittivity conditions in the UV-visible spectral range. Doped semiconductor nanomaterials, on the other hand, exhibit analogous plasmonic phenomenon typically in the infrared part of the spectrum.[7]

1.1.3 Surface plasmon damping

The plasmonic loss rates present a key challenge in the field of plasmonics limiting the application of this phenomenon in optoelectronics to a handful of technologies such as surface plasmon enhanced Raman scattering and biological molecule sensing.[2] The surface plasmon oscillation yields unrivaled sub-wavelength concentration of electric field at the surface of a nanomaterial. The sub-wavelength confinement of visible or infrared range optical modes is achieved in localized surface plasmon modes by coupling the electric field of a traverse electromagnetic wave (light wave) to the kinetic motion of free carriers sustain in a nanomaterial. The energy stored in kinetic motion of charge density can become large if the carriers are free to oscillate, a condition characterized by a large negative real permittivity magnitude, as outlined in the previous section. The speed of plasmonic free carrier motion is determined by the rate at

which the density is damped – the free carrier scattering rate g – assumed independent of oscillation frequency within the Drude model g is itself determined by many processes. These include: radiative damping, electron-electron scattering interactions, electron-lattice and ionized impurity or crystal defect scattering, interaction with inter-band transitions states in common noble metals as well scattering of surface imperfections and adsorbent molecules.[8, 9]

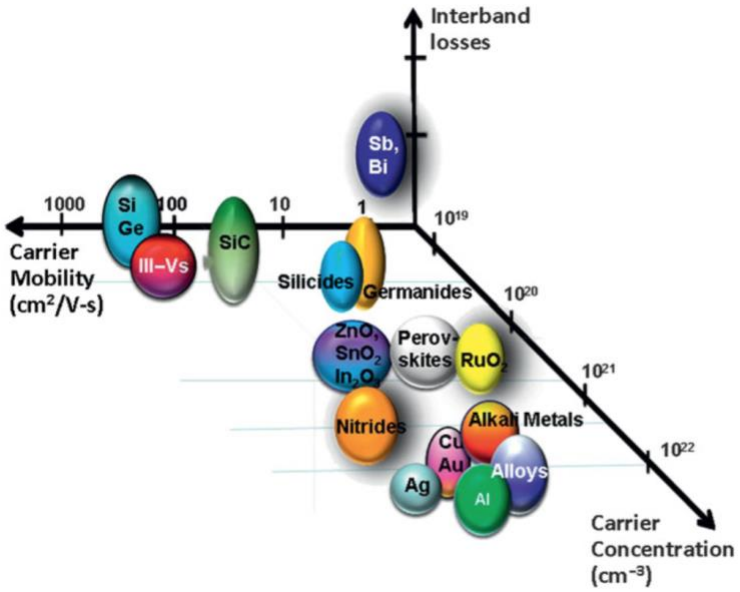

Figure 1.3 Materials design space available for plasmonics technology applications. Key parameters such as carrier concentration, carrier mobility or effective mass, and inter-band losses form the optimization phase space for next generation LSPR optoelectronics. Adapted from 9 and reprinted with permission.

Radiation damping arises from the scattering of light coupled to the oscillations of surface plasmons. [3] At the LSPR resonance frequency, the coupling and scattering of the light can become efficient by the same token. Nanoparticles with dimensions much smaller that the resonance wavelength, exhibit first order dipolar mode oscillation and are characterized by predominantly intrinsic absorption of light. However, as particle size

approaches the wavelength of oscillation, higher-order LSPR modes begin to dominate the in-coupling of light and the LSPR scattering cross-section can become greater than the absorption cross-section.[2]

In noble metals, g is primarily determined by the electron-electron damping rate due to the large intrinsic free carrier densities, typically on the order of 10^{23} cm^{-3}. Hence, a large portion of energy derived from LSPR optical extinction of a metallic particle is intrinsically damped within a few picoseconds and ultimately dissipated as heat on a scale of a nanoseconds.[10] The overall LSPR losses of metallic nanoparticles are typically weakly or negligibly dependent of geometry and dielectric environment within a narrow spectral regime.[9] Previous studies endeavored to mitigate loss by engineering the material structure or introducing optical gain media.[11] However, more recent findings suggest that manipulating the shape or size of a plasmonic particle cannot moderate absorption losses, as long as the structure remains substantially sub-wavelength.[12] The need to mitigate Ohmic losses in plasmonics has long been a key challenge in plasmonic materials research and has motivated the development of alternative doped semiconductor plasmonic materials systems over the last 5 years.[4, 8, 9]

1.1.4 Key challenges of metal-based surface plasmons

Significant leaps in understanding of plasmonic phenomena were undertaken over the past two decades. Initial studies of plasmonic light-matter interactions focused on the visible region of spectrum and utilized Au and Ag nanoparticles as the platform of investigation. The highly conductive noble metals were a natural choice due to their high electron density and corresponding large LSPR extinctions in the visible spectral range.[13]

A variety of noble metal nanoparticles with vastly diverse geometries, were engineered to support LSPRs in the UV though near-infrared region of the spectrum. The optical response of noble metal nanomaterials has been well characterized as a function of particle size, geometry, dielectric environment and inter-particle near-field coupling interactions.[14, 15] Despite the tremendous developments in synthesis and application, these noble metal plasmonic materials platform is fundamentally limited by its large fixed free carrier densities and practical considerations which beset the widespread implementation of LSPR functionality. We summarize the key challenges in traditional noble metal based plasmonics research as follows:

First, the intrinsic LSPR damping within the high electron density plasmon oscillations of metal particles, fundamentally limits the utility of these materials as nanoscale optical interconnects, waveguides, and optical sensors.[8] Free carrier densities on the order of 10^{23} cm^{-3} in Au and Ag yield electron damping rates on the order of 10^{14} s^{-1} at optical frequencies.[4] Large surface plasmon damping has long been considered a preeminent challenge in plasmonics.[9] However, recently plasmonic heating and energy conversion applications leveraging large plasmonic losses have emerged as well.[10, 16] LSPR loss mechanisms and the challenges associated with mitigating these process in metallic particles are discussed in the section above.

Second, metals exhibit intrinsically defined dielectric properties which cannot easily be tuned using the critical parameter of free carrier density. Although some modulation of metal carrier density has been demonstrated via charging/discharging processes, appreciable tunability of a metal particle LSPR frequency using this parameter

is not possible.[17] The optical response of metals is largely fixed upon material synthesis and dynamic post synthesis variation of LSPR properties is fundamentally limited.[18]

Lastly, energy sharing via coulombic coupling within arrays of plasmonic nanoparticles is critical for achieving large of electric field magnitude and confinement leveraged in plasmonic sensing and waveguiding applications.[19] In metal nanoparticle arrays, single nanometer control of inter-particle spacing and orientation is generally required for harnessing LSPR coupling interactions. This practical consideration fundamentally stems from LSPR damping limitations of metals. Additionally, defects and poor interfaces can also significantly contribute to shortening of LSPR excitation lifetime and thereby reducing the amplitude of oscillation, near-field enhancement magnitude, and the distance over which adjacent LSPRs can couple within extended array of plasmonic nanoparticles.[14]

1.1.5 Infrared plasmonics: applications and materials challenges

The field of plasmonics has now grown to encompass a wide range phenomena across UV to the infrared spectral regime. The lower energy part of the infrared spectral region, 2 μm > λ > 30 μm, facilitates a wide scope of important optoelectronic technologies such as molecular spectroscopy[20], infrared plant tissue imaging[21], night vision[22], and infrared energy harvesting.[23] There are many potential applications of LSPRs at longer wavelengths in the infrared and recent demonstrations of LSPR driven molecular sensing, infrared imaging and thermal emission have highlighted the utility of surface plasmons in this regime.

Early plasmonic chemical sensors in the visible range relied on the spectral shift of LSPR dielectric environment in accordance with equation 2 for detection surface binding molecules in question.[24] However, an analogous plasmonic sensing system in the mid-infrared range can facilitate direct probing of the adsorbent molecules using vibrational bonds and direct chemical identification without the need for differentiation based on the functional surface properties.[25] Additionally, plasmonics offer a new route for size reduction of infrared optoelectronics via efficient subwavelength confinement of long-wave optical modes in infrared lasers and efficient concertation of diffuse energy in infrared light via large LSPR absorption cross-section in infrared photodetectors.

As previously outlined, traditional metal plasmonic materials exhibit bulk plasma frequencies ω_p in the visible or UV range due to large carrier densities and correspondingly, large negative permittivity magnitudes. In order to extend the plasmonic resonance conditions for noble metals into the infrared, the early applications of infrared LSPRs utilized large, high aspect ratio geometries such nanorods[26] or various micro-scale lithographically fabricated metal surface gratings.[27] High aspect ratio particle geometry effectively stretches the longitudinal plasmon oscillation and red-shifts the resonance energy of this oscillation. However, as we approach the mid-infrared frequency range, the real permittivity magnitude of metals grows extremely large and these materials become near-perfect conductors unable to sustain subwavelength plasmonic resonance and corresponding electric field concentration at the particle surface.[27, 28] Subwavelength confinement of LSPR energy requires a material with real permittivity values on the order of its dielectric environment permittivity magnitude.[29] Hence, doped semiconductors offer a unique advantage as an alternative materials platform for LSPR

applications in the infrared. Semiconductor materials generally exhibit orders of magnitude lower free carrier densities and correspondingly smaller permittivity magnitudes, particularly in the infrared. Doped semiconductors, including group IV, group III-V, metal oxides and copper chalcogenide material have been demonstrated to yield sub-wavelength surface plasmon modes across the infrared frequency range and present a uniquely advantageous plasmonic materials platform in this regime.[30] Next, we review the development of these novel plasmonic materials and their associated challenges.

1.2 Plasmonic semiconductor nanomaterials

1.2.1 Introduction

LSPRs spectral response has been traditionally identified as the optical property of highly conductive metal particles. Doped semiconductors have recently emerged as an alternative plasmonic materials platform with unique opportunities to mitigate plasmon losses, actively modulate plasmonic properties via applied bias and electrochemistry, [31,32] and harness subwavelengths LSPRs across the infrared spectral range.[10] Recent studies of semiconductors nanomaterials suggest that virtually an infinite number of materials and particle geometries can be engineered to sustain surface plasmons.[31] In principal, it is only the availability of free charge carrier density and its interaction with electromagnetic radiation at the structure interfaces that is responsible for the subwavelength LSPR modes in metal and dielectric materials.[7]

Unlike the intrinsically fixed material properties of metals, semiconductors permit the modulation of free carrier density over a range of ~ 10^{10} – 10^{21} cm^{-3} via chemical doping, electrostatic gating, and optical excitation.[33, 34] This capability opens the door to actively tuning LSPR properties [35,36] as well as mitigating the electron scattering loss LSPR technology limitations.[9] Over the last decade, LSPRs have been shown in a wide range of semiconductor materials by generating free carrier density via (i) vacancy doping of binary or tertiary crystalline structures,[37, 38] (ii) aliovalent elemental substitution doping in covalently bonded lattices,[39, 40] and (iii) electrochemical redox potential shifting.[41, 42] Here, will survey the most prominent classes of plasmonic semiconductor nanomaterials studied for their LSPR properties primarily in the infrared part of the spectrum. We will discuss the plasmonic properties of materials shown in Figure 1.4, in the order as follows: (1) copper chalcogenides, (2) transparent conducting oxides, and (3) group IV and group III-V semiconductor nanomaterials.

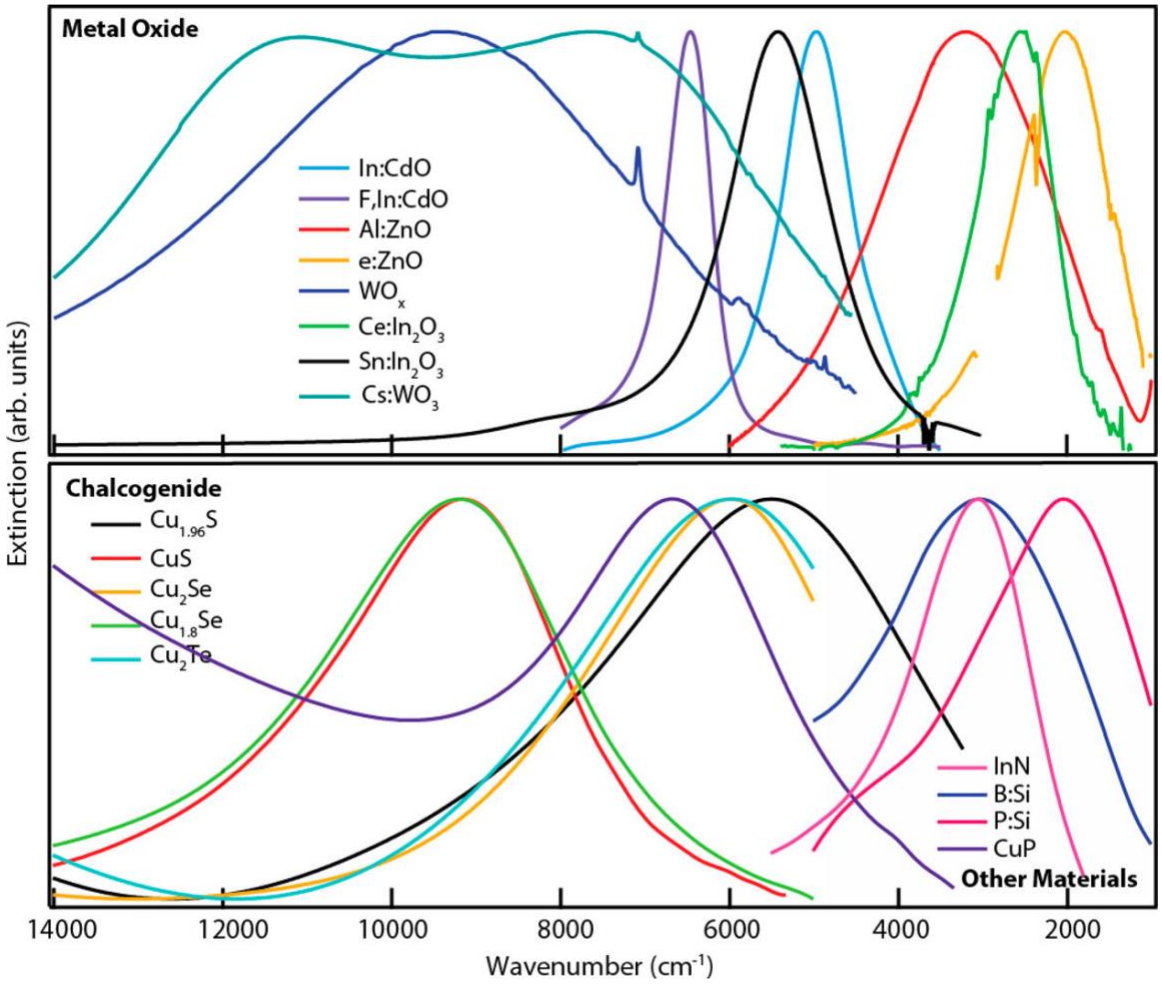

Figure 1.4 Compositionally tunable LSPR spectral response of copper chalcogenide, metal oxide, group IV and III-V nanocrystals synthesized with varying dopant contents, sizes and dielectric environments. Adapted from 29 and reprinted with permission

1.2.2 Copper-based chalcogenides

Copper-based chalcogenide nanocrystals, most notably $Cu_{2-x}S$, $Cu_{2-x}Se$, $Cu_{2-x}Te$, Cu_xIn_yS and their various metal derivatives, exhibit tunable physical, electric, and plasmonic properties by adjusting the material composition stoichiometry.[38] The crystal morphology and the electronic properties of chalcogenide nanocrystals strongly depends on the metal (copper) stoichiometric factor (2-x). $Cu_{2-x}S$, for example, can vary from x =

0 to 1 in with several stable intermediate phases including $Cu_{1.97}S$ (djurleite), $Cu_{1.8}S$ (digenite), $Cu_{1.4}S$ (anilite),[43] and others. Non-stoichiometric Cu^{2+} and Cu^{+} ions are thermodynamically favored in the crystalline structure and the vacant metal oxidation states yield free hole carriers. The process of bottom-up engineering material composition, free carrier density, and optical response applied of copper chalcogenide nanocrystals represents a paradigm shift in the field of plasmonics towards designed (or user defined) and tunable plasmonic materials.

Copper chalcogenide nanocrystals, fabricated using colloidal synthesis methods, have received much attention as a versatile and low-cost alternative plasmonic semiconductor materials.[38] Near-infrared absorption of colloidal chalcogenide nanocrystals has been known and attributed to inter-band transitions, until Zhao et al. proposed a plasmonic absorption mechanism due to free carrier densities in the $Cu_{2-x}S$ valence band.[44] Soon after in 2011, Luther et al. substantiated the LSPR driven absorption mechanism of $Cu_{2-x}S$ nanocrystals by surveying their near-infrared spectral response as a function of particle size, dielectric environment, and composition.[45] Since the free charge carriers in these nanocrystals are electron vacancies arising from elemental defects in the crystal, their effective masses are generally larger than those in substitutionally doped metal-oxides, group IV and III-V semiconductor materials. [29] Nonetheless, the vacancy doping mechanism has been shown to produce very large "hole" free carrier densities, typically on the order of 10^{21} cm^{-3}, and enable LSPRs across visible to infrared spectral range.[46-52]

The carrier density and the corresponding LSPR spectral response of copper chalcogenides according to equation 2, is typically tuned as a function the copper-

deficient stoichiometry. Exposure of $Cu_{2-x}S$ to oxygen, for example, leads to formation of oxidation of copper (Cu_2O), a reduction in free carrier density due to a decrease in the overall copper stoichiometric deficiency, and lastly a red-shifting of the NC LSPR in accordance with equation 2. For example, thermodynamically stable $Cu_{2-x}S$ and $Cu_{2-x}Se$ nanocrystals exhibit copper stoichiometric ratios approximately equal to 1.97 and 1.8, respectively. These correspond to free carrier densities of 1.4×10^{21} and 3×10^{21} cm^{-3}. Lastly, these hole densities yield LSPRs at wavelengths of 1700 nm and 1300 nm, respectively.[43] Notably, $Cu_{2-x}Te$ nanocrystals exhibit the lowest nonstoichiometric coppers of 1.6, which yield carrier densities of 5.0×10^{21} cm^{-3} and LSPRs peaks at 900 nm.[51] Lastly, the oxidation selectivity of chopper chalcogenide nanocrystal LSPR has been demonstrated as route to dynamically control of LSPR absorption energy and peak width via reversible redox chemical reactions post synthesis. [53]

The main concerns which limit the utility of copper chalcogenide nanocrystals based LSPR applications stem from their poor stability in ambient and poor crystal quality. The large LSPR surface damping rates and large effective hole carrier masses combine to yield losses which typically surpass those of noble metal nanoparticles. Organic ligands are necessary to control size, crystals facets, and direction of growth in colloidal synthesis and stabilize the nanocrystals surface post synthesis.[54] However, the nanocrystal LSPR energies approach surface molecule vibration excitation energies in the infrared. The overlap permits synergistic coupling and energy transfer between the LSPR modes and surface ligand exciton states.[55] At near infrared region, oleic acid stabilized $Cu_{2-x}S$, $Cu_{2-x}Se$ and $Cu_{2-x}Te$ nanocrystal ensemble measurements yield FWHM ranging

from 0.21 to 0.6 eV.[43] These values are approximately twice as large as those for spherical Au nanoparticles in the near infrared region.[24]

1.2.3 Transparent conducting oxides

Plasmonic transparent conducting oxide (TCO) semiconductor nanocrystals are emerging as a versatile platform for exploiting plasmonic phenomenon for infrared optoelectronics due to simplicity of synthesis and LSPR tunability across the near-to-mid infrared.[56] TCOs were first introduced as an alternative low loss plasmonic material, due to their smaller magnitude of real permittivity relative to that of noble metals, particularly in the near-infrared spectral regime.[34, 57-60] TCO nanocrystals synthesized from the relevant metal-containing precursors in the colloidal and vapor phases, prominently include materials such as tin-doped indium oxide (ITO), fluorine-doped tin oxide (FTO), aluminum-doped zinc oxide (AZO), gallium-doped zinc oxide (GZO), antimony-doped tin oxide (ATO), and indium-doped cadmium oxide (ICO).[32, 61-63] TCO are substitutionally doped with alliovalnet elements to enable LSPRs in the near-infrared spectral region. Unlike the vacancy-doped copper-chalcogenide materials, substitutionally doped TCO nanocrystals exhibit electron (n-type) rather hole (p-type) free carrier densities. Electron charge carriers exhibit an intrinsic advantage of lower effective masses over holes or electron vacancies. TCO nanocrystals LSPRs, therefore, typically effective carrier masses of less than 0.4,[34] approximately half the value of their copper chalcogenide counterparts. Smaller effective free carrier masses in TCOs reduce the minimal free carrier concentration required to sustain plasmon resonance as well as lowers the LSPR damping rates.

ITO nanomaterials present a model system for understanding the interplay of doping and LSPR effects in the TCO nanomaterials. Electron free carrier densities are introduced in ITO nanocrystals primarily through aliovalent substitution of In^{3+} by Sn^{4+} which contribute a single donor electron to lattice. Free carrier concentrations on the order of 10^{20} cm^{-3} are typically observed for colloidally synthesized ITO nanocrystals.[64, 65] Oxygen vacancies in the In_2O_3 crystal also effect carrier density, as oxygen interstitial defects readily accommodated in the In_2O_3 crystal, can compensate the electron density donated by aliovalent dopants.[66] The Sn dopant concentration is adjusted by changing Sn and In precursor ratios during synthesis. For example, using a 12 nm diameter spherical nanoparticle, Kanehara et al have demonstrated that increasing Sn/In ratios from 3% to 10% shifts the LSPR wavelength shifts from the mid-infrared to near-infrared regions. Interestingly, this study has also shown that increasing Sn concentration further up to 30% results in LSPR red-shift due to formation of Sn-O complexes which act as an electron sinks. [63] Carrier densities of approximately 5×10^{20} cm^{-3} have been estimated for similar near-infrared plasmonic ITO nanocrystals by the Milliron group. [32]

Al and Ga doped ZnO, also referred to as AZO and GZO nanocrystals, respectively, have also been investigated for their LSPRs in the 3 – 5 μm spectral range, sustained by corresponding carrier densities on the order of 10^{20} cm^{-3}. As observed for colloidal synthesis of ITO nanocrystals, the upper limit on carrier densities and thereby LSPR energies of both AZO and GZO nanocrystals, is set by a percent content of dopant precursor in synthesis which can contribute to free carrier concertation prior to interstitial rather substitutional dopant incorporation or formation of defects and charge trap complexes. [61, 67] The high energy LSPRs within the class of doped TCO nanocrystals,

were observed at approximately 1.6 μm for GZO (6 wt% Ga)[50] and ITO (10 wt% Sn)[63], at 2 μm for ICO (16.2 wt% In),[68] and at 3 μm AZO (7.3 wt% Al).[61] Plasmonic ITO nanowires have also been synthesized using a bottom-up growth process with vaporized powders of Sn and InO as the ITO precursors. Vertical arrays of ITO nanowires produced LSPR spectral response in the mid-infared range tunable as a function of nanowire aspect ratio.[62, 69] Interestingly, the free carrier densities of ITO nanowires were estimated in the range of 2 - 8 × 10^{20} cm^{-3}, comparable their colloidal synthesized nanocrystal counterparts, which suggests ITO nanowires are subject to similar substitutional Sn incorporation constraints.[63]

1.2.4 Group IV semiconductors

Group IV semiconductors, such as Si and Ge, principally underpin the intergraded circuit industry and UV-visible range optoelectronics. Due to its ubiquitous presence in electronic devices, Si plasmonic materials are a uniquely important platform for widespread integration of plasmonic functionality. Si materials offer the advantages of material abundance and relatively low cost, as well as extensively developed fabrication capabilities. Surface plasmon phenomenon in the form of far-IR propagating surface plasmon polaritons (SPPs) were first noted in Si inversion layer 40 years ago.[70] Heavily doped Si (>10^{20} cm^{-3}) thin-films[71, 72] fabricated using ion implantation methods, are known to exhibit a mid-infrared spectral response due to surface plasmon polaritons (SPPs), defined as propagating plasmon oscillations at the (semi-infinite) material interface. Many current studies have focused on mid-IR SPPs in lithographically degenerately doped Si films.[73, 74] Recently, infrared LSPRs have been demonstrated in phosphorus doped Si nanowires and nanocrystals [39, 75]

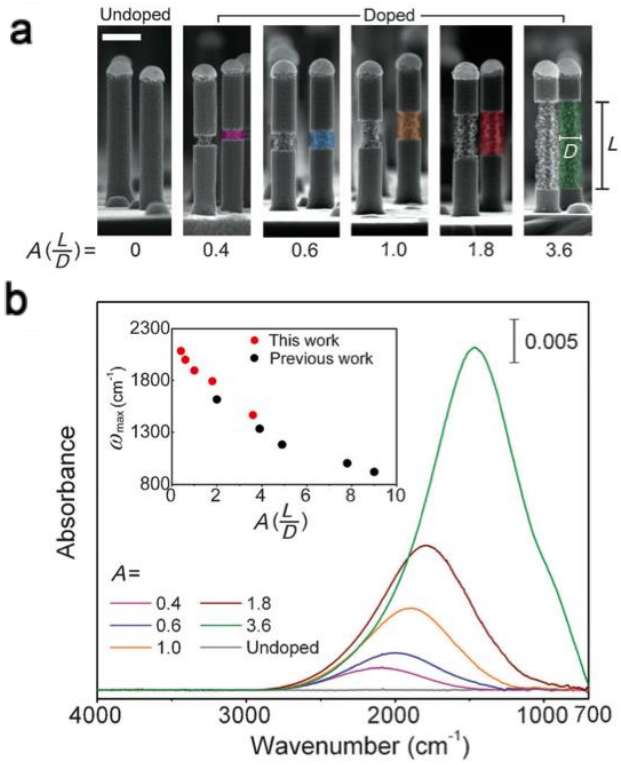

Figure 1.5 Phosphorus doped Si nanowire LSPR dependence on embedded resonator aspect ratio. (a) SEM images of silicon nanowires etched in buffered oxide etch (BOE) solution to expose the doped segment morphology. (b) The *in-situ* measured spectral response of nanowire samples shown in (a). Adapted from 38 and reprinted with permission.

In 2012, the Filler group first reported electron carrier densities on the order of 10^{20} cm^{-3} in Si nanowires doped with phosphorus during the vapor-liquid-solid (VLS) nanowire growth process.[39] The VLS nanowire growth technique, first outlined by Wagner and Ellis in 1964,[76] yields uniform arrays of single crystalline and epitaxial aligned Si nanowires with user programmable axial dopant profiles. The technique designation, vapor-liquid-solid, specifies the physical pathway of precursor atoms in this system. A gaseous chemical precursor, such as silane or disilane for silicon, reacts at the

liquid catalyst surface delivering silicon atoms from the vapor phase to the eutectic metal (Au) droplet. [77] The bottom-up VLS fabrication process offers the advantages of precise control over the nanowire geometry, surface facets, and distribution within a vertically aligned array.[78] Additionally, the dynamic control of dopant precursor flow during synthesis offer opportunity to engineering 1 dimensional arrays of doped plasmonic segments embedded along the length of a nanowire.[79] In 2013, Chou *et al* applied this approach to engineer a multi-modal LSPR spectral response in phosphorous doped Si nanowires.[80] The dielectric anisotropy inherent to the nanowire geometry was shown to yield a dominant longitudinal plasmon oscillation along the nanowire axis. Subsequent investigation have further demonstrated the deterministic role of the host semiconducting nanowire material on the LSPR properties of an embedded doped resonator.[81]

In 2013, the Kortshagen group had first demonstrated LSPRs sustained in phosphorus doped Si nanocrystals. [75] A chemical dopant concentration on the order of 10^{21} cm^{-3} was achieved in sub 10 nm Si nanocrystals using the non-thermal plasma synthesis technique with SiH_4 and PH_3, as precursors. The active dopant concertation was estimated to be on the order 10^{20} cm^{-3}, resulting LSPR in the mid-infrared region. However, unlike the VLS synthesized Si nanowire based LSPRs, these Si nanocrystals were shown loose the LSPR spectral response upon oxidation, likely due to a non-uniform dopant distribution within the nanocrystals and formation electron traps at the surface in air. Boron doped Si nanocrystals with a mid-infrared spectral response were synthesized soon after by the same group.[82] In contrast, boron doped Si nanocrystals did not exhibit an LSPR spectral response immediately upon synthesis but rather gain and retain plasmonic absorption peaks following oxidation and post synthesis heat treatment.

The LSPR behavior of these nanocrystals was likewise shown to be consistent with large surface doping contribution. Additionally, these small particles are synthesized with diameters < 10 nm and exhibit non-uniform shapes and surface facets, which results in significant broadening of the aggregate nanocrystal solution and film spectral response measurements.[40]

Doped Ge materials are also attractive group IV plasmonic materials due to their low permittivity magnitude in the infrared, low effective free carrier masses and high quality materials fabrication capabilities via single crystalline epitaxial growth processes. Phosphorus and boron dopant elemental content on the order of 10^{19} cm^{-3} has been shown for VLS doped Ge nanowires.[83] Mid-infrared surface plasmons in Ge were first demonstrated using micron scale phosphorus doped Ge antenna pairs, which were lithographically etched from a Ge films grown on Si via a low energy plasma-enhanced CVD process. [84] The coupled Ge particle pairs were also used to demonstrate spectral sensitivity to adsorbent molecular vibrations around 10 μm. Furthermore, heavily doped Ge particle pairs were later shown to exhibit nonlinear optical properties and yield subwavelength optical emission via third-harmonic generation.[85] The plasmonic properties of doped Ge nanomaterials remain largely unexplored despite the advantages due to fabrication challenges and limited doping capabilities for bottom-growth Ge nanowires and nanocrystals.[86]

1.2.5 Group III-V semiconductors

Direct band-gap III-V compound semiconductors are prominent materials in the field of optoelectronics due to their direct band-gap, small electron effective mass, and

small permittivity magnitude.[7] Studies of III-V nanocrystals have largely focused on quantum confinement effects, size-dependent photoluminescence, and optical band-gap absorption effects. [87, 88] Nonetheless, III-V semiconductors, such as InP, InAs, and InSb, are promising low-loss plasmonic materials in the infrared.[89, 90, 91] In general, these nanomaterials are beset by poor dopant solubility and substitution efficiency, which limit the carrier density to the range of $10^{18} - 10^{19}$ cm^{-3}. [92] Near-infrared LSPRs have been demonstrated for heavily Si-doped InAs and S-doped InP nanocrystals.[87, 93] However, the LSPR properties of colloidal synthesized group III-V semiconductors remain relatively unexplored in part due to strong covalent bonds in the crystal that obstruct substitutional dopant incorporation to minimize strain and lead to self-purification.[64]

1.3 Summary and Outlook

The utility of semiconductor plasmonic materials is ultimately determined and limited by the material doping capabilities and methods used in engineering the plasmonic spectral response. The upper limit on the free carrier density that can be engineered in a semiconducting nanomaterial is generally determined by the solubility and incorporation efficiency of impurity atoms in the crystal structure. For example, despite tremendous research effort, phosphorus doped Si nanowires synthesized using the VLS technique, and Si nanocrystals synthesized using a nonthermal plasma process, have produced estimated maximum carrier densities of 0.7 and 3.0×10^{20} cm^{-3}, respectively. [3994] Likewise, colloidally synthesized ITO nanocrystals and CVD fabricated pillars have produced carrier densities of similar magnitude suggesting a fundamental limit in

activation and incorporation of impurities. [40, 69] Hence, most semiconductors exhibit a narrow spectral range over which their LSPR spectral response can be chemically tuned via vacancy or aliovalent substitution doping methods.

1.3.1 Limits of doping

Beyond the introduction of free carrier density, the incorporation of impurity atoms into a semiconductor or dielectric material host lattice can substantially modify the physical properties of a material. For example, Sn content in Sn dopant in ITO nanocrystals impacts the concentration of activated Sn substitutional defects and oxygen vacancies which can act as deep traps for electrons.[95] The concentrations of the activated dopant sites and oxygen vacancies together determine the free carrier concentration. Furthermore, in heavily (degeneratively) doped semiconductor nanocrystals the crystal defects, inactive dopant clusters, as well as the ionized dopant impurities density determine the nanoparticle plasmonic properties (LSPR energy, intensity and damping rate). [96-98]

Maximizing the LSPR near field intensity is a major focus in the current development of plasmonic technologies. This optimization is typically managed via synthetic shape control[99] and engineering inter-particle interactions.[36] Additionally, the near-field magnitude is dependent on the free carrier scattering rate within a material. At the plasmon resonance condition the maximum kinetic energy stored in the oscillation and thereby the maximum near near-field intensity at the surface of a nanoparticle is limited by the free carrier damping rate. For heavily doped nanoparticles, the LSPR near-field intensity can become inversely dependent on doping magnitude as impurity

scattering can significantly dampen the surface plasmon resonance.[7]

1.3.2 Optical multi-functionality via co-doping

Doping of semiconductor nanoparticles additionally allows for engineering of multifunctional properties. Si and Ge nanowires heterostructures, that contain separate an atomically precise p-n junction – separate electron (n) and hole (p) carrier functional domains have been engineered by switching corresponding dopant precursors during the VLS nanowire growth process using a solid catalyst.[79, 100] p-n plasmonic interfaces and their electric bias dependence remain unexplored and may lead to novel emergent plasmonic phenomena. Additionally, multi-functionality such as magnetism and plasmonic free carrier density oscillations are of interest for novel optical switch device applications.[101, 102] Fe and Sn doped In_2O_3 nanoparticles, for example, have been shown to exhibit both magnetic spin and surface plasmon properties arising from each of the respective dopant element properties.[103, 104] Engineering unique combinations of electrical, magnetic and optical functionalities within semiconductor nanomaterials via co-doping is a new avenue of plasmonics research that promises emergent phenomena and technology applications.

1.3.3 Dynamic post-synthesis LSPR tuning

Dynamic control of LSPR properties post synthesis is a unique advantage of doped semiconductor materials over metals.[30] Dynamic LSPR tuning via modulation of carrier density has been widely investigated primarily using (i) electrochemical charging, (i) redox reactions and (iii) photo-activated charging methods. An electrochemical potential modulates the Fermi level position and thereby, the free charge carrier type

(electron or hole) and density within a semiconducting material.[105-107] Reversible electrochemical modulation of the LSPR spectral response has been widely studied for nanocrystal films in solution. In redox reactions, the nanoparticle gains or losses electron density upon being exposed to a reducing or an oxidizing chemical agent, respectively.[42, 105, 108, 109] Lastly, LSPR tuning via photochemical charging requires high intensity optical excitation of the electronic transition across the semiconductor band-gap and in the presence of a reducing agent to stabilize the excited electron in the conduction band.[101, 110, 111] The research of dynamically controlled LSPRs promises new LSPR utility, particularly in the infrared with application such as smart absorbing windows,[32] plasmonic optical interconnects,[112] and chemical sensors. [113]

In summary, doped semiconductors materials have emerged as the preeminent materials platform for development of optoelectronic technologies harnessing the LSPR phenomena in the infrared spectral regime. Doped semiconductors exhibit low permittivity magnitude values across the infrared, and are thereby uniquely capable of subwavelength LSPR optical confinement and electric field concentration in the infrared. The experimental studies and theoretical analysis which are outlined in this dissertation Chapters 2-4, demonstrate and substantiate the advantages of doped semiconductor nanomaterials harnessing infrared LSPRs for next-generation optoelectronic technologies.

1.4 References

1. Torchilin, V.P., *Engineered gold nanoparticles as contrast agents for biological medical imaging*, in *Handbook of nanobiomedical research : Fundamentals, applications, and recent developments*. 2014, World Scientific: Hackensack, New Jersey. p. 4 volumes.
2. Le Ru, E.C. and P.G. Etchegoin, *Principles of surface-enhanced raman spectroscopy : And related plasmonic effects*. 1st ed. 2009, Amsterdam ; Boston: Elsevier. xxiii, 663 p.
3. Brongersma, M.L. and P.G. Kik, *Surface plasmon nanophotonics*. Springer series in optical sciences. 2007, Dordrecht: Springer. vii, 268 p.
4. Naik, G.V., V.M. Shalaev, and A. Boltasseva, *Alternative plasmonic materials: Beyond gold and silver.* Adv Mater, 2013. **25**(24): p. 3264-94.
5. Willets, K.A. and R.P. Van Duyne, *Localized surface plasmon resonance spectroscopy and sensing.* Annu Rev Phys Chem, 2007. **58**: p. 267-97.
6. Ashcroft, N.W. and N.D. Mermin, *Solid state physics*. 1976, New York,: Holt. xxi, 826 p.
7. Zhong, Y.J., et al., *Review of mid-infrared plasmonic materials.* Journal of Nanophotonics, 2015. **9**.
8. Boriskina, S.V., et al., *Losses in plasmonics: From mitigating energy dissipation to embracing loss-enabled functionalities.* Advances in Optics and Photonics, 2017. **9**(4): p. 775-827.
9. Khurgin, J.B. and A. Boltasseva, *Reflecting upon the losses in plasmonics and metamaterials.* Mrs Bulletin, 2012. **37**(8): p. 768-779.

10. Brongersma, M.L., N.J. Halas, and P. Nordlander, *Plasmon-induced hot carrier science and technology.* Nature Nanotechnology, 2015. **10**(1): p. 25-34.

11. Khurgin, J.B. and A. Boltasseva, *Reflecting upon the losses in plasmonics and metamaterials.* MRS Bulletin, 2012. **37**(08): p. 768-779.

12. Bozhevolnyi, S.I. and T. Sondergaard, *General properties of slow-plasmon resonant nanostructures: Nano-antennas and resonators.* Optics Express, 2007. **15**(17): p. 10869-10877.

13. Boltasseva, A. and H.A. Atwater, *Low-loss plasmonic metamaterials.* Science, 2011. **331**(6015): p. 290-291.

14. Schuller, J.A., et al., *Plasmonics for extreme light concentration and manipulation (vol 9, pg 193, 2010).* Nature Materials, 2010. **9**(4).

15. Mayer, K.M. and J.H. Hafner, *Localized surface plasmon resonance sensors.* Chemical Reviews, 2011. **111**(6): p. 3828-57.

16. Clavero, C., *Plasmon-induced hot-electron generation at nanoparticle/metal-oxide interfaces for photovoltaic and photocatalytic devices.* Nature Photonics, 2014. **8**(2): p. 95-103.

17. Hirakawa, T. and P.V. Kamat, *Charge separation and catalytic activity of ag@tio2 core−shell composite clusters under uv−irradiation.* Journal of the American Chemical Society, 2005. **127**(11): p. 3928-3934.

18. Guo, L.H., et al., *Strategies for enhancing the sensitivity of plasmonic nanosensors.* Nano Today, 2015. **10**(2): p. 213-239.

19. Biswas, S., et al., *Plasmonic resonances in self-assembled reduced symmetry gold nanorod structures.* Nano Letters, 2013. **13**(5): p. 2220-2225.

20. Mcdonald, R.S., *Infrared spectrometry - review.* Analytical Chemistry, 1986. **58**(9): p. 1906-1925.

21. Turker-Kaya, S. and C.W. Huck, *A review of mid-infrared and near-infrared imaging: Principles, concepts and applications in plant tissue analysis.* Molecules, 2017. **22**(1).

22. Razeghi, M. and B.M. Nguyen, *Advances in mid-infrared detection and imaging: A key issues review.* Reports on Progress in Physics, 2014. **77**(8).

23. Byrnes, S.J., R. Blanchard, and F. Capasso, *Harvesting renewable energy from earth's mid-infrared emissions.* Proceedings of the National Academy of Sciences of the United States of America, 2014. **111**(11): p. 3927-3932.

24. Lee, K.S. and M.A. El-Sayed, *Gold and silver nanoparticles in sensing and imaging: Sensitivity of plasmon response to size, shape, and metal composition.* Journal of Physical Chemistry B, 2006. **110**(39): p. 19220-19225.

25. Agrawal, A., et al., *Resonant coupling between molecular vibrations and localized surface plasmon resonance of faceted metal oxide nanocrystals.* Nano Letters, 2017. **17**(4): p. 2611-2620.

26. Brown, L.V., et al., *Surface-enhanced infrared absorption using individual cross antennas tailored to chemical moieties.* Journal of the American Chemical Society, 2013. **135**(9): p. 3688-3695.

27. Stanley, R., *Plasmonics in the mid-infrared.* Nature Photonics, 2012. **6**(7): p. 409-411.

28. Novotny, L., *Effective wavelength scaling for optical antennas.* Physical Review Letters, 2007. **98**(26).

29. Law, S., V. Podolskiy, and D. Wasserman, *Towards nano-scale photonics with micro-scale photons: The opportunities and challenges of mid-infrared plasmonics.* Nanophotonics, 2013. **2**(2): p. 103-130.

30. Agrawal, A., et al., *Localized surface plasmon resonance in semiconductor nanocrystals.* Chemical Reviews, 2018. **118**(6): p. 3121-3207.

31. Comin, A. and L. Manna, *New materials for tunable plasmonic colloidal nanocrystals.* Chemical Society Reviews, 2014. **43**(11): p. 3957-3975.

32. Garcia, G., et al., *Dynamically modulating the surface plasmon resonance of doped semiconductor nanocrystals.* Nano Letters, 2011. **11**(10): p. 4415-4420.

33. Comin, A. and L. Manna, *New materials for tunable plasmonic colloidal nanocrystals.* Chemical Society Reviews, 2014.

34. Naik, G.V., V.M. Shalaev, and A. Boltasseva, *Alternative plasmonic materials: Beyond gold and silver.* Advanced Materials, 2013. **25**(24): p. 3264-3294.

35. Priolo, F., et al., *Silicon nanostructures for photonics and photovoltaics.* Nature Nanotechnology, 2014. **9**(1): p. 19-32.

36. Schuller, J.A., et al., *Plasmonics for extreme light concentration and manipulation.* Nature Materials, 2010. **9**(3): p. 193-204.

37. Luther, J.M., et al., *Localized surface plasmon resonances arising from free carriers in doped quantum dots.* Nature Materials, 2011. **10**(5): p. 361-366.

38. Coughlan, C., et al., *Compound copper chalcogenide nanocrystals.* Chemical Reviews, 2017. **117**(9): p. 5865-6109.

39. Chou, L.-W., et al., *Tunable mid-infrared localized surface plasmon resonances in silicon nanowires.* Journal of the American Chemical Society, 2012. **134**(39): p. 16155-16158.

40. Zhang, H., et al., *Doped silicon nanocrystal plasmonics.* Acs Photonics, 2017. **4**(4): p. 963-970.

41. Faucheaux, J.A. and K. Jain, *Plasmons in photocharged zno nanocrystals revealing the nature of charge dynamics.* Journal of Physical Chemistry Letters, 2013. **4**(18): p. 3024-3030.

42. Jain, P.K., et al., *Doped nanocrystals as plasmonic probes of redox chemistry.* Angewandte Chemie-International Edition, 2013. **52**(51): p. 13671-13675.

43. Kriegel, I., et al., *Tuning the excitonic and plasmonic properties of copper chalcogenide nanocrystals.* Journal of the American Chemical Society, 2011. **134**(3): p. 1583-1590.

44. Zhao, Y., et al., *Plasmonic cu2−xs nanocrystals: Optical and structural properties of copper-deficient copper(i) sulfides.* Journal of the American Chemical Society, 2009. **131**(12): p. 4253-4261.

45. Luther, J.M., et al., *Localized surface plasmon resonances arising from free carriers in doped quantum dots.* Nature Materials, 2011. **10**(5): p. 361-366.

46. Niezgoda, J.S., et al., *Novel synthesis of chalcopyrite cuxinys2 quantum dots with tunable localized surface plasmon resonances.* Chemistry of Materials, 2012. **24**(16): p. 3294-3297.

47. Li, W.H., et al., *Metal ions to control the morphology of semiconductor nanoparticles: Copper selenide nanocubes.* Journal of the American Chemical Society, 2013. **135**(12): p. 4664-4667.

48. Manthiram, K. and A.P. Alivisatos, *Tunable localized surface plasmon resonances in tungsten oxide nanocrystals.* Journal of the American Chemical Society, 2012. **134**(9): p. 3995-3998.

49. Li, W., et al., *Metal ions to control the morphology of semiconductor nanoparticles: Copper selenide nanocubes.* Journal of the American Chemical Society, 2013. **135**(12): p. 4664-4667.

50. Hessel, C.M., et al., *Copper selenide nanocrystals for photothermal therapy.* Nano Letters, 2011. **11**(6): p. 2560-2566.

51. Kriegel, I., et al., *Shedding light on vacancy-doped copper chalcogenides: Shape-controlled synthesis, optical properties, and modeling of copper telluride nanocrystals with near-infrared plasmon resonances.* Acs Nano, 2013. **7**(5): p. 4367-4377.

52. Niezgoda, J.S., et al., *Novel synthesis of chalcopyrite cuxinys2 quantum dots with tunable localized surface plasmon resonances.* Chemistry of Materials, 2012. **24**(16): p. 3294-3298.

53. Dorfs, D., et al., *Reversible tunability of the near-infrared valence band plasmon resonance in cu2-xse nanocrystals.* Journal of the American Chemical Society, 2011. **133**(29): p. 11175-11180.

54. Hsu, S.-W., W. Bryks, and A.R. Tao, *Effects of carrier density and shape on the localized surface plasmon resonances of cu2–xs nanodisks.* Chemistry of Materials, 2012. **24**(19): p. 3765-3771.

55. Liu, H. and P. Guyot-Sionnest, *Photoluminescence lifetime of lead selenide colloidal quantum dots.* Journal of Physical Chemistry C, 2010. **114**(35): p. 14860-14863.

56. Diroll, B.T., et al., *Synthesis of n-type plasmonic oxide nanocrystals and the optical and electrical characterization of their transparent conducting films.* Chemistry of Materials, 2014. **26**(15): p. 4579-4588.

57. Naik, G.V., J. Kim, and A. Boltasseva, *Oxides and nitrides as alternative plasmonic materials in the optical range [invited].* Optical Materials Express, 2011. **1**(6): p. 1090-1099.

58. Kim, J., et al., *Plasmonic resonances in nanostructured transparent conducting oxide films.* Selected Topics in Quantum Electronics, IEEE Journal of, 2013. **19**(3): p. 4601907-4601907.

59. Luque, A. and S. Hegedus, *Handbook of photovoltaic science and engineering*. 2nd ed. 2011, Chichester, West Sussex, U.K.: Wiley. xxxii, 1132 p.

60. Kim, J., et al., *Plasmonic resonances in nanostructured transparent conducting oxide films.* Ieee Journal of Selected Topics in Quantum Electronics, 2013. **19**(3).

61. Buonsanti, R., et al., *Tunable infrared absorption and visible transparency of colloidal aluminum-doped zinc oxide nanocrystals.* Nano Letters, 2011. **11**(11): p. 4706-4710.

62. Li, S.Q., et al., *Infrared plasmonics with indium–tin-oxide nanorod arrays.* Acs Nano, 2011. **5**(11): p. 9161-9170.

63. Kanehara, M., et al., *Indium tin oxide nanoparticles with compositionally tunable surface plasmon resonance frequencies in the near-ir region.* Journal of the American Chemical Society, 2009. **131**(49): p. 17736-17737.

64. Buonsanti, R. and D.J. Milliron, *Chemistry of doped colloidal nanocrystals.* Chemistry of Materials, 2013. **25**(8): p. 1305-1317.

65. Agrawal, A., R.W. Johns, and D.J. Milliron, *Control of localized surface plasmon resonances in metal oxide nanocrystals.* Annual Review of Materials Research, Vol 47, 2017. **47**: p. 1-31.

66. Gonzalez, G.B., et al., *Defect structure studies of bulk and nano-indium-tin oxide.* Journal of Applied Physics, 2004. **96**(7): p. 3912-3920.

67. Della Gaspera, E., et al., *Low-temperature processed ga-doped zno coatings from colloidal inks.* Journal of the American Chemical Society, 2013. **135**(9): p. 3439-3448.

68. Gordon, T.R., et al., *Shape-dependent plasmonic response and directed self-assembly in a new semiconductor building block, indium-doped cadmium oxide (ico).* Nano Letters, 2013. **13**(6): p. 2857-2863.

69. Li, S.Q., et al., *Plasmonic-photonic mode coupling in indium-tin-oxide nanorod arrays.* Acs Photonics, 2014. **1**(3): p. 163-172.

70. Allen, S.J., D.C. Tsui, and R.A. Logan, *Observation of 2-dimensional plasmon in silicon inversion layers.* Physical Review Letters, 1977. **38**(17): p. 980-983.

71. Streyer, W., et al., *Strong absorption and selective emission from engineered metals with dielectric coatings.* Optics Express, 2013. **21**(7): p. 9113-9122.

72. Chen, Y.B. and Z.M. Zhang, *Heavily doped silicon complex gratings as wavelength-selective absorbing surfaces.* Journal of Physics D: Applied Physics, 2008. **41**(9): p. 095406.

73. Ginn, J.C., et al., *Infrared plasmons on heavily-doped silicon.* Journal of Applied Physics, 2011. **110**(4).

74. Shahzad, M., et al., *Infrared surface plasmons on heavily doped silicon.* Journal of Applied Physics, 2011. **110**(12).

75. Rowe, D.J., et al., *Phosphorus-doped silicon nanocrystals exhibiting mid-infrared localized surface plasmon resonance.* Nano Letters, 2013. **13**(3): p. 1317-1322.

76. Wagner, R.S. and W.C. Ellis, *Vapor-liquid-solid mechanism of single crystal growth.* Applied Physics Letters, 1964. **4**(5): p. 89.

77. Schmidt, V., J.V. Wittemann, and U. Gosele, *Growth, thermodynamics, and electrical properties of silicon nanowires.* Chemical Reviews, 2010. **110**(1): p. 361-388.

78. Schmidt, V., et al., *Silicon nanowires: A review on aspects of their growth and their electrical properties.* Adv Mater, 2009. **21**(25-26): p. 2681-2702.

79. Dayeh, S.A., et al., *Progress in doping semiconductor nanowires during growth.* Materials Science in Semiconductor Processing, 2017. **62**: p. 135-155.

80. Chou, L.-W. and M.A. Filler, *Engineering multimodal localized surface plasmon resonances in silicon nanowires.* Angewandte Chemie, 2013. **125**(31): p. 8237-8241.

81. Chou, L.-W., et al., *Influence of dielectric anisotropy on the absorption properties of localized surface plasmon resonances embedded in si nanowires.* The Journal of Physical Chemistry C, 2014. **118**(10): p. 5494-5500.

82. Kramer, N.J., K.S. Schramke, and U.R. Kortshagen, *Plasmonic properties of silicon nanocrystals doped with boron and phosphorus.* Nano Letters, 2015. **15**(8): p. 5597-5603.

83. Perea, D.E., et al., *Direct measurement of dopant distribution in an individual vapour-liquid-solid nanowire.* Nat. Nano., 2009. **4**(5).

84. Baldassarre, L., et al., *Midinfrared plasmon-enhanced spectroscopy with germanium antennas on silicon substrates.* Nano Letters, 2015. **15**(11): p. 7225-7231.

85. Fischer, M.P., et al., *Mid-infrared third-harmonic emission from heavily-doped germanium plasmonic nanoantennas.* 2017 Conference on Lasers and Electro-Optics (Cleo), 2017.

86. Frigerio, J., et al., *Tunability of the dielectric function of heavily doped germanium thin films for mid-infrared plasmonics.* Physical Review B, 2016. **94**(8).

87. Felts, J.R., et al., *Near-field infrared absorption of plasmonic semiconductor microparticles studied using atomic force microscope infrared spectroscopy.* Applied Physics Letters, 2013. **102**(15): p. -.

88. Stiegler, J.M., et al., *Nanoscale free-carrier profiling of individual semiconductor nanowires by infrared near-field nanoscopy.* Nano Letters, 2010. **10**(4): p. 1387-1392.

89. Guilengui, V.N., et al., *Localized surface plasmon resonances in highly doped semiconductors nanostructures.* Applied Physics Letters, 2012. **101**(16).

90. Felts, J.R., et al., *Near-field infrared absorption of plasmonic semiconductor microparticles studied using atomic force microscope infrared spectroscopy.* Applied Physics Letters, 2013. **102**(15).

91. Law, S., et al., *Making the mid-infrared nano with designer plasmonic materials.* Optoelectronic Devices and Integration Iv, 2012. **8555**.

92. Tsame Guilengui, V., et al., *Localized surface plasmon resonances in highly doped semiconductors nanostructures.* Applied Physics Letters, 2012. **101**(16): p. -.

93. Stiegler, J.M., et al., *Nanoscale free-carrier profiling of individual semiconductor nanowires by infrared near-field nanoscopy.* Nano Letters, 2010. **10**(4): p. 1387-1392.

94. Boyuk, D.S., L.W. Chou, and M.A. Filler, *Strong near-field coupling of plasmonic resonators embedded in si nanowires.* Acs Photonics, 2016. **3**(2): p. 184-189.

95. Hwang, J.H., et al., *Point defects and electrical properties of sn-doped in-based transparent conducting oxides.* Solid State Ionics, 2000. **129**(1-4): p. 135-144.

96. Lounis, S.D., et al., *Defect chemistry and plasmon physics of colloidal metal oxide nanocrystals.* Journal of Physical Chemistry Letters, 2014. **5**(9): p. 1564-74.

97. Runnerstrom, E.L., et al., *Defect engineering in plasmonic metal oxide nanocrystals.* Nano Letters, 2016. **16**(5): p. 3390-3398.

98. Donovan, B.F., et al., *Interplay between mass-impurity and vacancy phonon scattering effects on the thermal conductivity of doped cadmium oxide.* Applied Physics Letters, 2016. **108**(2).

99. Agrawal, A., I. Kriegel, and D.J. Milliron, *Shape-dependent field enhancement and plasmon resonance of oxide nanocrystals.* Journal of Physical Chemistry C, 2015. **119**(11): p. 6227-6238.

100. Geaney, H., et al., *Atomically abrupt silicon-germanium axial heterostructure nanowires synthesized in a solvent vapor growth system.* Nano Letters, 2013. **13**(4): p. 1675-1680.

101. Kriegel, I., et al., *Ultrafast photodoping and plasmon dynamics in fluorine indium codoped cadmium oxide nanocrystals for all-optical signal manipulation at optical communication wavelengths.* Journal of Physical Chemistry Letters, 2016. **7**(19): p. 3873-3881.

102. Marinica, D.C., et al., *Active quantum plasmonics.* Science Advances, 2015. **1**(11).

103. Tandon, B., G.S. Shanker, and A. Nag, *Multifunctional sn- and fe-codoped in2o3 colloidal nanocrystals: Plasmonics and magnetism.* Journal of Physical Chemistry Letters, 2014. **5**(13): p. 2306-2311.

104. Tandon, B., A. Yadav, and A. Nag, *Delocalized electrons mediated magnetic coupling in mn-sn codoped in2o3 nanocrystals: Plasmonics shows the way.* Chemistry of Materials, 2016. **28**(11): p. 3620-3624.

105. Carroll, G.M., et al., *Redox potentials of colloidal n-type zno nanocrystals: Effects of confinement, electron density, and fermi-level pinning by aldehyde*

hydrogenation. Journal of the American Chemical Society, 2015. **137**(34): p. 11163-11169.

106. Dahlman, C.J., et al., *Spectroelectrochemical signatures of capacitive charging and ion insertion in doped anatase titania nanocrystals.* Journal of the American Chemical Society, 2015. **137**(28): p. 9160-9166.

107. Pradhan, N., et al., *Luminescence, plasmonic, and magnetic properties of doped semiconductor nanocrystals.* Angewandte Chemie-International Edition, 2017. **56**(25): p. 7038-7054.

108. Kriegel, I., et al., *Tuning the excitonic and plasmonic properties of copper chalcogenide nanocrystals.* Journal of the American Chemical Society, 2012. **134**(3): p. 1583-1590.

109. Schimpf, A.M., et al., *Electronic doping and redox-potential tuning in colloidal semiconductor nanocrystals.* Accounts of Chemical Research, 2015. **48**(7): p. 1929-1937.

110. Rinehart, J.D., et al., *Photochemical electronic doping of colloidal cdse nanocrystals.* Journal of the American Chemical Society, 2013. **135**(50): p. 18782-18785.

111. Cohn, A.W., et al., *Photocharging zno nanocrystals: Picosecond hole capture, electron accumulation, and auger recombination.* Journal of Physical Chemistry C, 2012. **116**(38): p. 20633-20642.

112. Kinsey, N., et al., *Examining nanophotonics for integrated hybrid systems: A review of plasmonic interconnects and modulators using traditional and*

alternative materials [invited]. Journal of the Optical Society of America B-Optical Physics, 2015. **32**(1): p. 121-142.

113. Strobbia, P., E. Languirand, and B.M. Cullum, *Recent advances in plasmonic nanostructures for sensing: A review.* Optical Engineering, 2015. **54**(10).

CHAPTER 2.

ENGINEERING SERIES OF ABRUPT LOCALIZED SURFACE PLASMON RESONANCES IN SI NANOWIRES

2.1 Introduction

2.1.1 Motivation

As described in detail in Chapter 1, LSPRs offers a route to confine electromagnetic waves into deep-sub-wavelength volumes. While conventional metals are traditionally leveraged for this purpose,[1-3] semiconductors are now receiving increased attention.[4-6] Semiconductors enable modulation of charge carrier density *via* chemical doping, electrostatic gating, and/or optical excitation and [7] this capability opens the door to new opportunities in applications such as photo-thermal therapy,[8] smart windows,[9] chemical sensing,[10] and information processing.[11, 12] Si-based materials offer the additional advantages of elemental abundance and extensive processing know-how.

Uniformly doped Si nanowires as well as nanowires with doped segments embedded along the length, can support localized surface plasmon resonances infrared similar to plasmonic effects observed for metal nanorods. [13]The capacity to design and fabricate complex axial carrier density profiles in a bottom-up user-defined manner makes the Si nanowire plasmonic system an uniquely important platform for studying and exploiting the interactions of mid-infrared LSPRs. Robust control of carrier density profile is critical for harnessing the near-field effects extensively studied for plasmonic nanoparticles,[14-17] and which serve as the basis of ultrasensitive spectroscopy,[18] compact

waveguides,[2] non-linear optical enhancements,[19] and even catalysis.[20] When two LSPR-supporting nanoparticles are brought into close proximity, tremendous local electric field enhancements are generated between them. The strength of such near-field interactions, and thus the magnitude of the local field enhancement, inversely depends on inter-particle separation (above the quantum regime).[21] Nanoparticle dimensions, and thus inter-particle spacing, are easily defined for metals since the carrier density profile is uniform throughout. However, the "dimensions" of a plasmonic semiconductor nanoparticle will also depend on its carrier density profile. Thus, to engineer near-field interactions in plasmonic semiconductor nanoparticles, it is imperative to understand and control the factors governing the placement and activation of dopant atoms.

2.1.2 Axial carrier density profile engineering in VLS grown Si nanowires

Vapor-liquid-solid synthesis – where a liquid catalyst droplet collects atoms from the vapor and directs crystallization of the solid[22-24] – permits the incorporation of multiple, axially-registered doped segments, and thus LSPRs, along the length of individual nanowires.[25] This method allows for reasonable control of dopant profile by temporally modulating dopant precursor (*e.g.*, PCl_3 for phosphorus doping of Si nanowires[25]) delivery, but axial gradients are common and limit the plasmonic design space for nanowires.[26] Such behavior is most often explained with the so-called "reservoir effect," where atoms in the finite volume growth catalyst continue to incorporate into the nanowire even after precursor flow ceases.[27-30]

In the present work, we show the impact of axially carrier density gradients on the spectral response of Si nanowires containing multiple resonators. *In situ* infrared spectral

response measurements and scattering simulations within the discrete dipole approximation (DDA) are a powerful method to study these effects.[31] A considerable residual carrier density remains in the spacer segment between intentionally encoded resonators that yields unexpected spectral features and modifies near-field interactions. A reduction of substrate temperature during spacer segment growth can mitigate these effects. We use this approach to fabricate Si nanowires with spectral responses indistinguishable from those of nanowires with ideal, atomically abrupt carrier density profiles. In addition to studying the optical properties of doped Si nanowires, our methodology is useful for probing complex carrier density profiles that can be challenging for transport measurements, electron holography, Kelvin force probe microscopy, and scanning photocurrent microscopy.[32-35]

2.2 Experimental Methods

2.2.1 Si nanowire growth using the vapor-liquid-solid technique

Experimental protocols are similar to previous work[36, 37] and briefly summarized here. A double-side polished Si (111) substrate (El-Cat, FZ, 15-30 Ω-cm, double side polished) is initially cleaned in HF (J.T. Baker, 10%) for 5 minutes and rinsed in deionized water prior to insertion into a custom-built ultrahigh vacuum (UHV) chamber. Pressures are not corrected for ion gauge sensitivity. The substrate is resistively annealed at 700 °C for 1 hour and then flashed to 1200 °C for 30 seconds in vacuum. A thin film of Au (ESPI Metals, 99.999%) is thermally evaporated at a rate of 1 nm/min after cooling to room temperature at a rate of approximately 2 °C/s.

Nanowire arrays are grown using the VLS technique in a two-step process in an ultra-high-vacuum chemical vapor deposition (CVD) system shown in Figure 2.1. During the "incubation step," which includes Au film break up, Ostwald ripening, and initial nanowire nucleation, the substrate temperature is ramped to and held at 620 °C while maintaining a 4×10^{-5} Torr Si_2H_6 (Voltaix, 99.998%) partial pressure for 5 minutes. Nanowire array areal densities near 1 nanowire/μm^2 are obtained with this procedure. To initiate the "elongation step," where nanowires are grown and encoded with one or more phosphorus-doped segments, the substrate temperature is lowered to 540 °C at a rate of 3 °C/s at constant Si_2H_6 partial pressure. Phosphorous-doped segments are generated by introducing PCl_3 (Strem Chemicals, 99.999%) at a partial pressure of 3×10^{-6} Torr. Between each doped segment, as described in the main text, the substrate temperature is either maintained at 540 °C or reduced to 465 °C. Nanowire growth rates are approximately 9 and 5 nm/min at 4×10^{-5} Torr Si_2H_6 and substrate temperatures of 540 °C and 465 °C, respectively. PCl_3 partial pressures as high as 3.0×10^{-6} Torr do not strongly impact nanowire growth rate.[36]

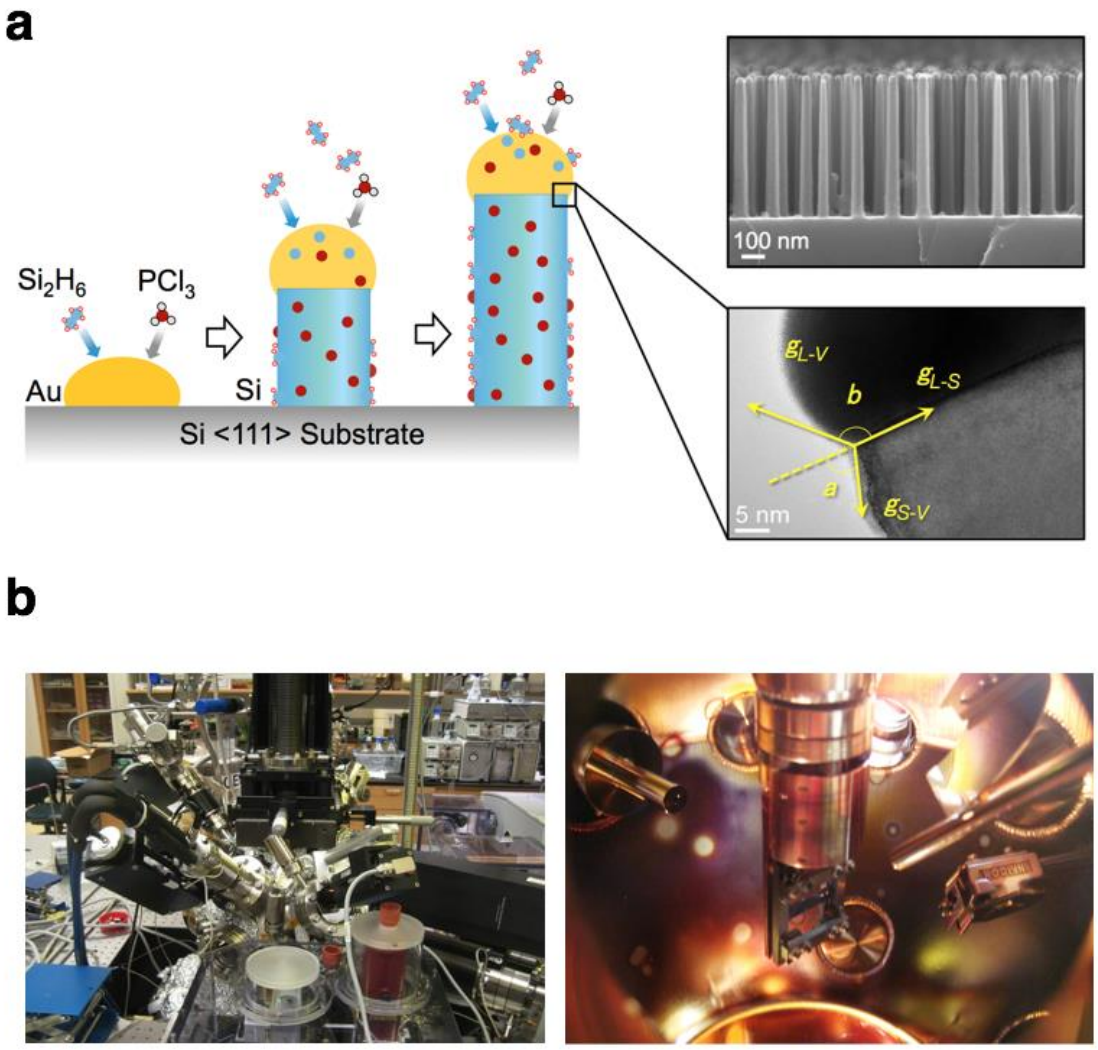

Figure 2.1 (a) The vapor-liquid-solid nanowire growth process illustrated for an Au-catalyzed phosphorous-doped Si nanowire grown using disilane (Si_2H_6) and phosphorus-trichloride (PCl_3) as precursors. (b) An ultra-high-vacuum chemical vapor deposition chamber used to fabricate the doped-Si nanowires and characterize their in-situ infrared spectral response.

2.2.2 Characterization of Si nanowire plasmonic spectral response

The extinction spectra of as-grown nanowire arrays are measured *in situ* at room temperature using infrared spectroscopy (Bruker, Vertex 70) with a transmission geometry. Unpolarized light from a SiC light source is used in combination with a liquid

nitrogen-cooled HgCdTe detector and a KBr beam-splitter to collect data between 700 and 3400 cm^{-1} with a resolution of 4 cm^{-1}. All spectra are recorded at an angle of incidence of 58° to probe the longitudinal LSPR absorption mode. The absorption strength of the transverse LSPR is more than an order of magnitude weaker than the longitudinal LSPR, as shown for single and multiple doped segments in Figure 2.2 and Figure 2.3, the measured spectral response is almost entirely due to the longitudinal LSPR. They are subsequently processed by subtracting the spectra recorded at 0° and baselined with a concave rubberband method. To reveal doped segment geometry, nanowire arrays are etched in buffered HF (J.T. Baker, 5:1) solution for up to 3 minutes after spectral response measurement and removal from the vacuum system. Nanowire morphology is examined using a Zeiss Ultra-60 field-emission scanning electron microscope (SEM).

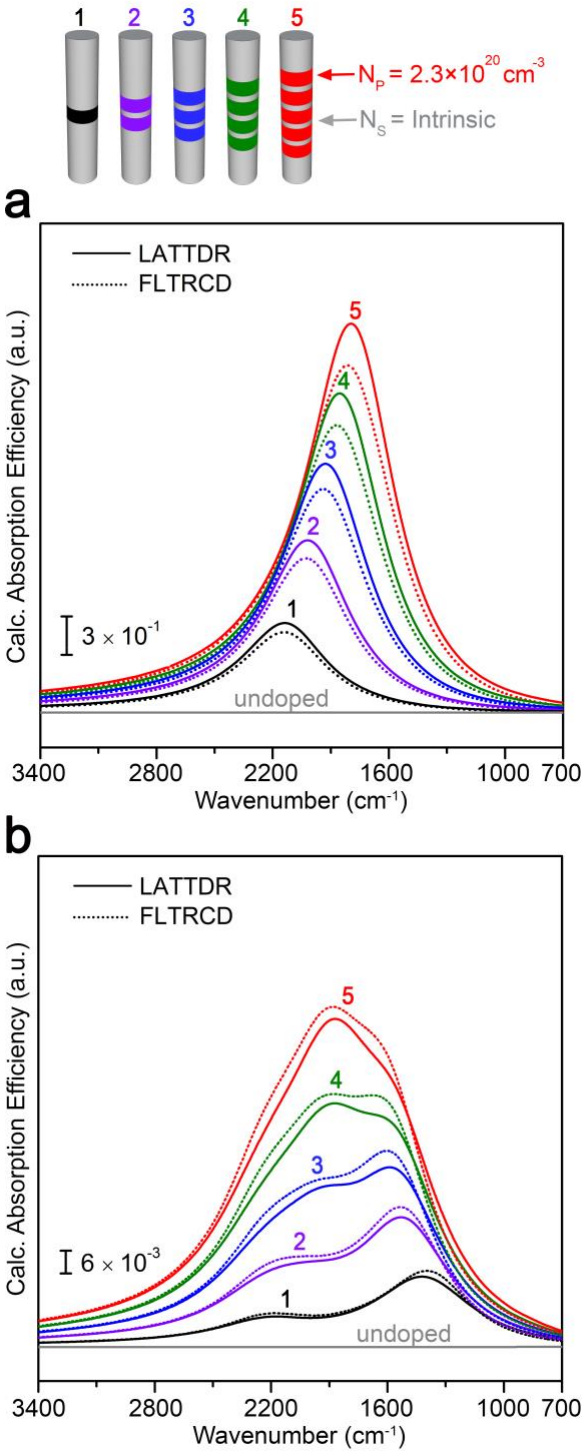

Figure 2.2. Comparison of DDA method and longitudinal vs. transverse LSPRs. Calculated absorption efficiency of the (a) longitudinal and (b) transverse LSPR mode using the LATTDR and FLTRCD methods in DDSCAT 7.3. The GKDLDR method yields spectra (not shown) identical to those from LATTDR. The longitudinal mode is orders of magnitude stronger than the transverse mode.

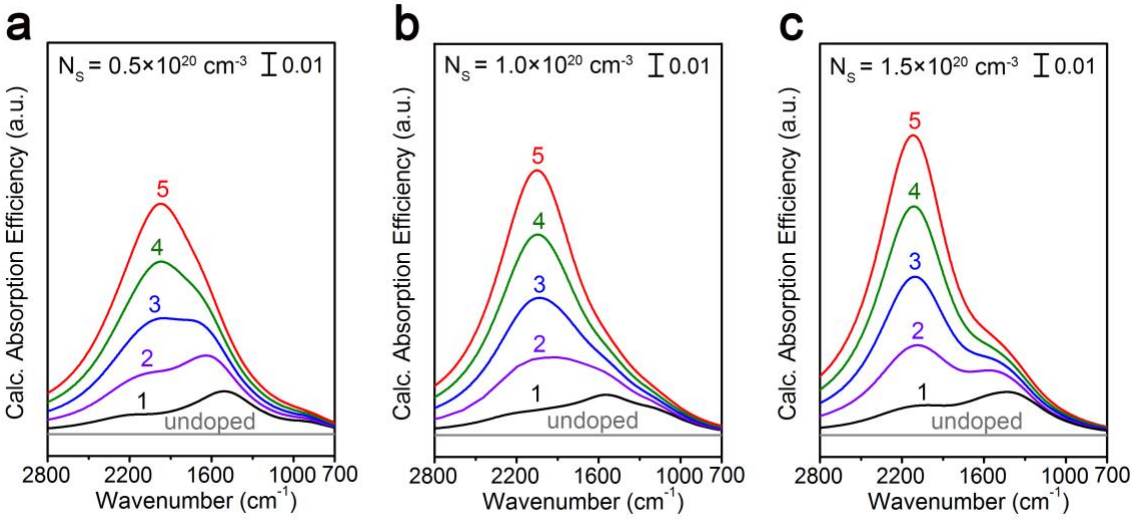

Figure 2.3. Effect of spacer segment carrier density on transverse LSPR. Calculated transverse mode absorption efficiencies for individual Si nanowires containing 0 - 5 primary resonators (N_P = 2.3 × 10^{20} cm^{-3}) with spacer segments exhibiting carrier densities (N_S) of (a) 0.5, (b) 1.0, and (c) 1.5 × 10^{20} cm^{-3}.

2.2.3 Discrete Dipole Approximation simulation methods

Doped Si nanowire spectral response is simulated within the discrete dipole approximation (DDA) using the DDSCAT 7.3 code, analogous to that described previously.[31] The LATTDR method utilized here yields results effectively equivalent to those from GKDLTR and FLTRCD as shown in Figure 2.2. The spectral response, local field enhancement, and polarization vector map for a longitudinally applied electric field are calculated for individual, cylindrical nanowires with overall dimensions matching those of as-synthesized nanowires, specifically a length of 650 nm and diameter of 130 nm. Simulations of individual nanowires are appropriate for the present work since inter-nanowire coupling is negligible for arrays with low areal densities (~1 nanowire/μm^2). All "primary" (*i.e.*, intentionally encoded) resonators are modeled with carrier densities,

N_P, of 2.3×10^{20} cm^{-3} and lengths of 50 nm. Each primary resonator is each separated by a 20 nm spacer region. The carrier density of the "spacer" region, N_S, is varied as described in the main text. Each nanowire is simulated using a total of 8905 dipoles with a periodic grid spacing of 10 nm as illustrated in Figure 2.4. The refractive indices (n) and extinction coefficients (k) of bulk Si as a function of carrier density are obtained from Palik and an extended Drude model.[38] A conjugate gradient iteration is applied until the error tolerance is below 10^{-5}.

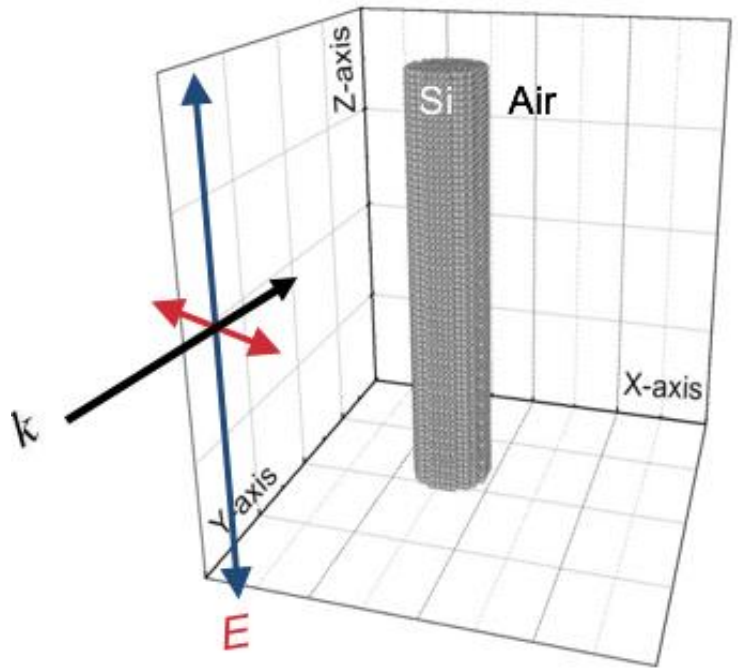

Figure 2.4 A dipole array used to represent a nanowire in a DDA simulation using a total of 8905 dipoles with a periodic grid spacing of 10 nm.

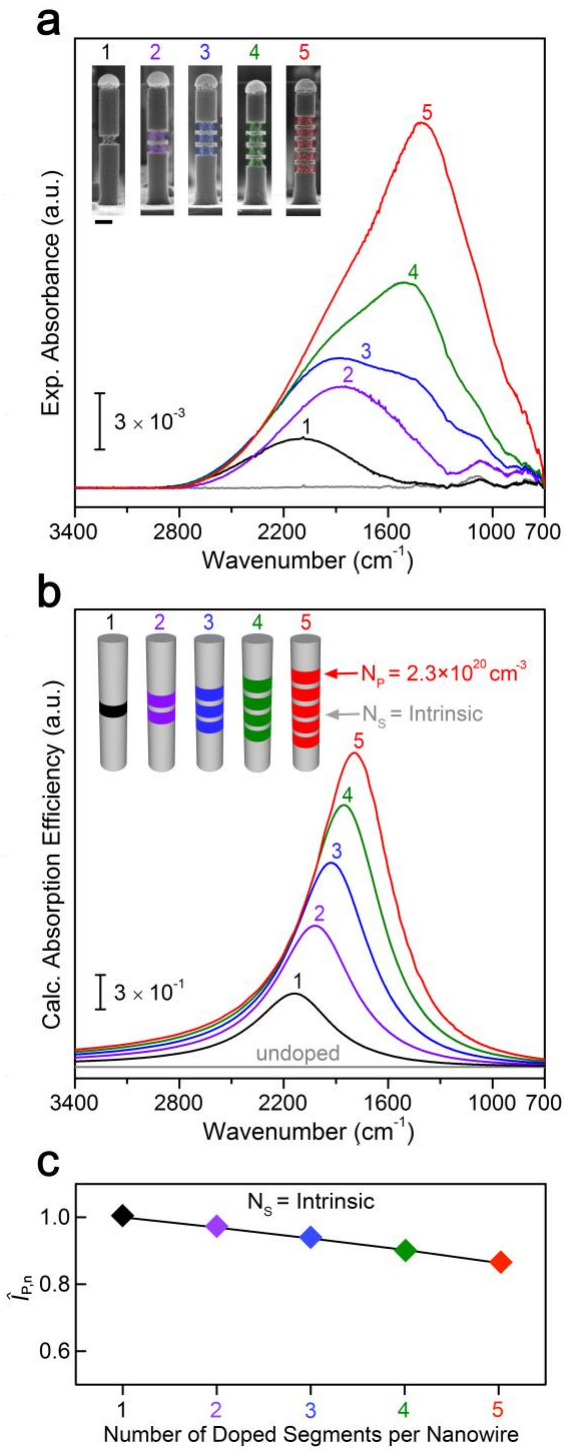

Figure 2.5. Comparison of experimental and expected Si nanowire spectral responses for the longitudinal LSPR. (a) Experimental spectral response for an array of Si nanowires each containing 0 - 5 primary resonators. Primary resonators and spacer segments are grown at a substrate temperature of 540 °C. Inset: Side view SEM images of representative nanowires following a buffered oxide etch treatment to determine doped segment geometry. (b) Calculated absorption efficiency for individual Si nanowires

containing 0 - 5 primary resonators (N_P = 2.3 × 10^{20} cm^{-3}) and intrinsic spacer segments (N_S = intrinsic Si). (c) Integrated absorption efficiencies from the spectra in (b) normalized according to Eq. 1.

2.3 Results and Discussion

2.3.1 Spectral response of a series of doped resonators in a Si nanowire

Figure 2.5a shows a series of experimental spectral response measurements for arrays of Si nanowires containing 0 to 5 "primary" (*i.e.*, intentionally encoded) resonators. Our prior work shows that the carrier density of resonators fabricated in this manner is near 2.3 × 10^{20} cm^{-3} and that the observed spectral features result from resonant absorption, rather than scattering.[31] Representative SEM images of Si nanowires after buffered HF etching are displayed in the Figure 2.6a inset and reveal the geometry of each resonator. All aspect ratios appear the same within the limits of this etching technique. As expected, a single absorption band is observed for Si nanowires containing one primary resonator. However, the absorption features for Si nanowires containing 2 to 5 resonators exhibit a pronounced asymmetry consistent with multiple, convoluted peaks.

We simulate the spectral response of the longitudinal LSPR to further understand this behavior. Figure 2.5b shows calculated absorption efficiencies for Si nanowires with 0 to 5 primary resonators (N_P = 2.3 × 10^{20} cm^{-3}) with intrinsic "spacer" segments (N_S = intrinsic). Our simulations predict, consistent with the scattering of metal particles arranged in 1-D chains,[39] a monotonically increasing absorption intensity and redshift of the absorption maximum as the number of primary resonators increases. The substantial redshift observed in Figure 2.5b ($\Delta\nu_{1\text{-}5}$ = 347 cm^{-1}) suggests strong near-field coupling for this system, as expected due to the large dielectric constant of intrinsic Si and

anisotropic dielectric environment of the nanowire geometry.[31] The effect of adding an additional resonator can be quantified, as shown in Figure 2.5c, by normalizing the integrated absorption efficiency according to Eq. 1:

$$\hat{I} = \frac{I_{j,n}}{I_{j,1} n} \tag{1}$$

where $I_{j,n}$ and $\hat{I}_{j,n}$ are the measured and normalized integrated intensity of the j^{th} mode for nanowires with n primary resonators, respectively. While there is only one mode in Figure 2.5b, and thus no need to distinguish between multiple modes, this definition is useful for the subsequent discussion. Notably, Figure 2.5c shows that each additional resonator (1-5) provides an increasingly smaller absorption enhancement, despite adding the same number of additional charge carriers. We attribute this behavior to the proximity of the doped segments, where a neighboring segment acts to lower the overall dielectric function of the surroundings. A constant increase in absorption enhancement would be expected for doped segments with larger spacing. The simulated spectral response for the transverse LSPR, shown in Figure 2.2, exhibits additional complexity. However, its contribution to the experimental spectra is negligible, as its absorption efficiency is an order of magnitude lower than that for the longitudinal LSPR. As shown in our previous work, the optical properties of undoped Si and the nanowire's anisotropic dielectric structure produce an image dipole that strongly damps the transverse LSPR.[31] We include these data for the transverse LSPR here and below for completeness.

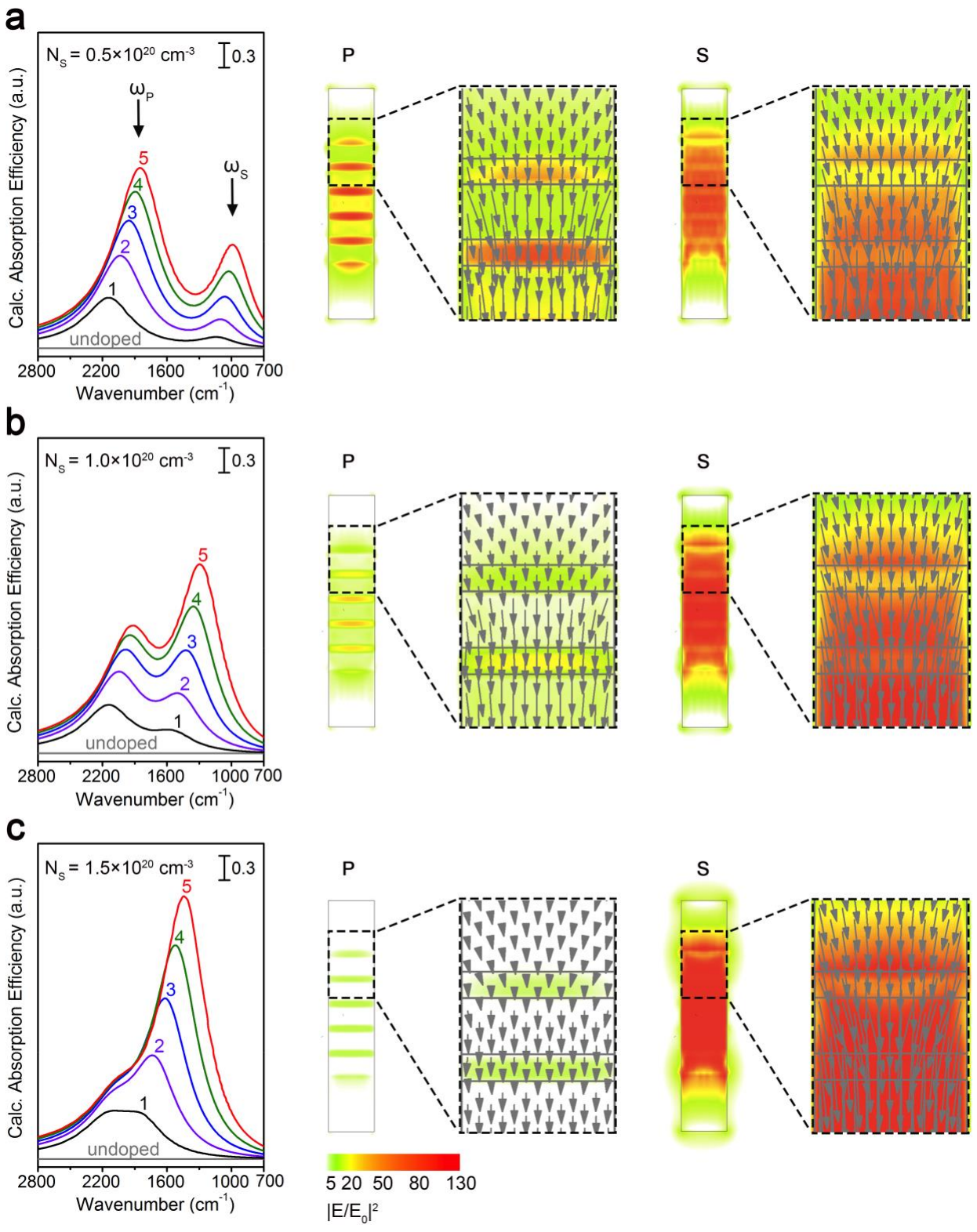

Figure 2.6 Effect of spacer segment carrier density on longitudinal LSPR. Calculated longitudinal mode absorption efficiencies for individual Si nanowires containing 0 - 5 primary resonators (N_P = 2.3 × 10^{20} cm^{-3}) with spacer segments exhibiting carrier

densities (N_S) of (a) 0.5, (b) 1.0, and (c) 1.5×10^{20} cm^{-3}. The high (labeled 'ω_P') and low (labeled 'ω_S') frequency absorption modes are attributed to the "primary" and "spacer" segments, respectively. E-field enhancement maps and polarization vector plots of the P and S mode at each value of N_S are shown for the case of 5 primary resonators, and determined at the absorption efficiency maximum of the longitudinal LSPR. The magnitude of the E-field enhancement is indicated by a red-to-green gradient.

2.3.2 Carrier density profile effects on LSPR spectral response

We hypothesize that the differences observed between Figure 2.5a and 2.5b result from dopant profiles in our fabricated Si nanowires that are less abrupt than the ideal profiles used in the simulation. To explore this possibility, we numerically investigate nanowires with primary resonators separated by spacer segments with non-zero carrier densities. Figure 2.6 displays calculated absorption efficiencies and electric-field enhancement maps for the longitudinal LSPR with 0 - 5 primary resonators ($N_P = 2.3 \times 10^{20}$ cm^{-3}) and N_S values of 0.5, 1.0, and 1.5×10^{20} cm^{-3}. Two distinct absorption features are present in all cases. The high (labeled 'ω_P') and low (labeled 'ω_S') energy modes result from absorption predominantly arising from the primary resonators and spacer segments, respectively. Both modes redshift and increase in intensity as the number of resonators increases. The frequency and absorption strength of the S mode also increases concomitantly with spacer segment carrier density. The transverse LSPR remains weak for any number of primary resonators as shown in Figure 2.2.

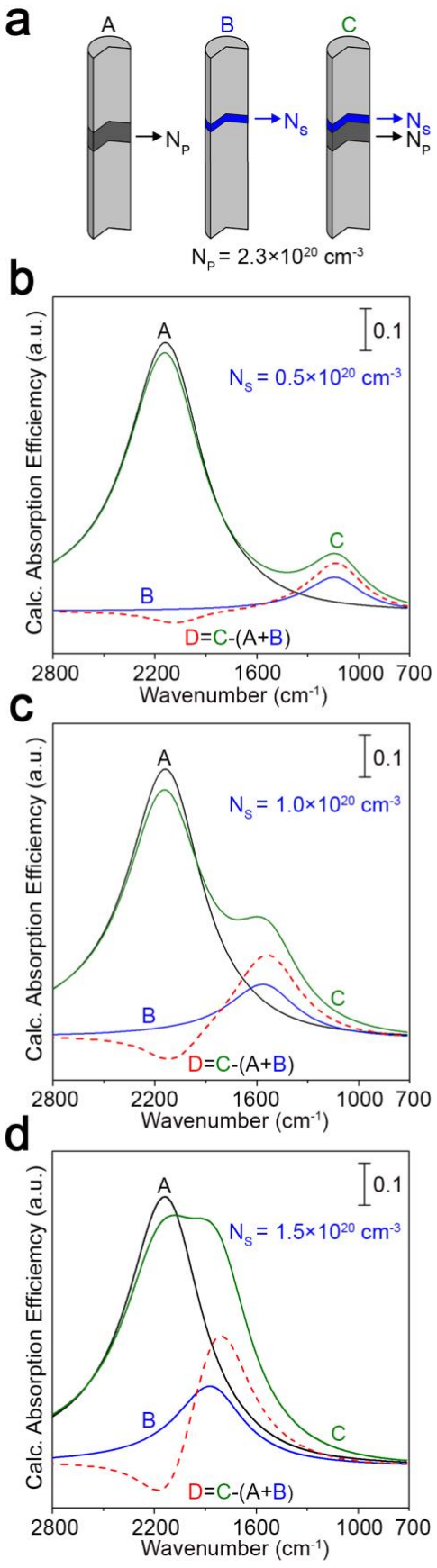
a
A
B
C
N_P
N_S
N_S
N_P
$N_P = 2.3\times10^{20}$ cm^{-3}
b
A
0.1
$N_S = 0.5\times10^{20}$ cm^{-3}
C
B
D=C-(A+B)
Calc. Absorption Efficiemcy (a.u.)
2800
2200
1600
1000
700
Wavenumber (cm^{-1})
c
A
0.1
$N_S = 1.0\times10^{20}$ cm^{-3}
B
C
D=C-(A+B)
Calc. Absorption Efficiemcy (a.u.)
2800
2200
1600
1000
700
Wavenumber (cm^{-1})
d
A
0.1
$N_S = 1.5\times10^{20}$ cm^{-3}
B
C
D=C-(A+B)
Calc. Absorption Efficiemcy (a.u.)
2800
2200
1600
1000
700
Wavenumber (cm^{-1})

Figure 2.7 Inter-segment LSPR effects. The absorption efficiency spectra of silicon nanowires containing a single N_P, a single N_S as well adjacent N_P and N_S phosphorus-doped segments were calculated using the DDA method and labeled A, B, and C in the figure accordingly. Spectrum labeled D was obtained by subtracting the calculated spectra A and B from C. Hence, spectrum D represents the inter-segment LSPR effects which occur when the two doped segments are located adjacent within a single nanowire. The calculation results are displayed in the order of increasing N_S segment phosphorous dopant concentration: 0.5×10^{20} cm^{-3}, 1.0×10^{20} cm^{-3}, and 1.5×10^{20} cm^{-3}, corresponding to figure parts (b), (c), and (d) accordingly.

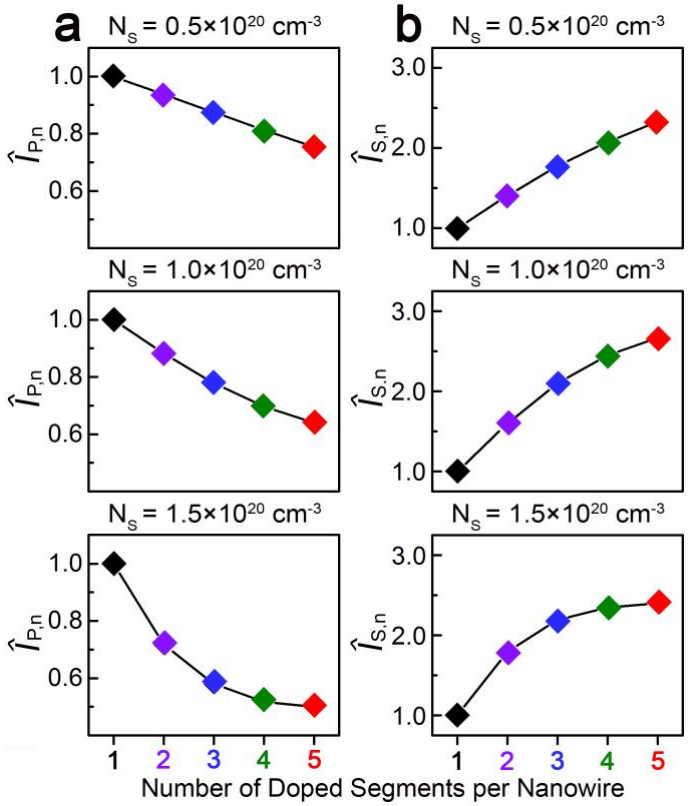

Figure 2.8 Normalized absorption strength. Integrated absorption efficiencies of the (a) P and (b) S modes from the spectra in Figure 2.2 normalized according to Eq. 1 for individual Si nanowires containing 1 - 5 primary resonators ($N_P = 2.3 \times 10^{20}$ cm^{-3}) with spacer segments exhibiting carrier densities (N_S) of 0.5, 1.0, and 1.5×10^{20} cm^{-3}.

The complex dielectric structure of the doping superlattices contained in these nanowires also leads to other, less obvious behavior. Figure 2.7 shows the diminishing absorption due to inter-segment LSPR interactions between a single heavily doped (N_P) and a lightly doped spacer segment (N_S) as a function of spacer segment carrier density. Figure 2.8 displays the normalized integrated intensity of each mode (*i.e.,* P and S) as per Eq. 1. Analogous to that observed for nanowires with intrinsic spacer segments (Figure 2.2c), Figure 2.8a indicates that the values of $\hat{I}_{P,n}$ are incrementally smaller with each additional resonator. More importantly, the extent of this effect increases as a function of spacer segment carrier density (N_S) and the number of coupled resonators in series. We attribute this behavior to changes in the dielectric function of the spacer segments *at the frequency of the P mode*.[38] For intrinsic spacer segments, the real part of Si's dielectric function, ε_S (where the subscript 'S' denotes the spacer segment), is 11.6 and independent of frequency in the infrared. In this situation, the intrinsic Si strongly polarizes and enhances primary resonator coupling. However, ε_S decreases as N_s increases *at the frequency of the P mode*. For example, $\varepsilon_S = 5.2$ for a spacer segment with a carrier density of 1.0×10^{20} cm^{-3} at $\omega_P = 2139$ cm^{-1}. The reduced polarizability of the spacer segment hinders coupling, as seen in the electric-field enhancement maps of Figure 2.6, and reduces P mode absorption strength. $\hat{I}_{P,n}$ drops most quickly upon adding the first few resonators (*e.g.*, from n = 1 to 2), as most easily seen for $N_S = 1.5 \times 10^{20}$ cm^{-3}. This effect stems from the substantial changes in dielectric environment upon transitioning from that of purely intrinsic Si to one that is partially doped. Figure 2.8b shows that $\hat{I}_{S,n}$ increases as a function of resonator number, indicating enhanced coupling of the spacer

segments. This effect is the inverse of that discussed above for the P mode. In other words, ε_P increases as N_s increases *at the frequency of the S mode*.

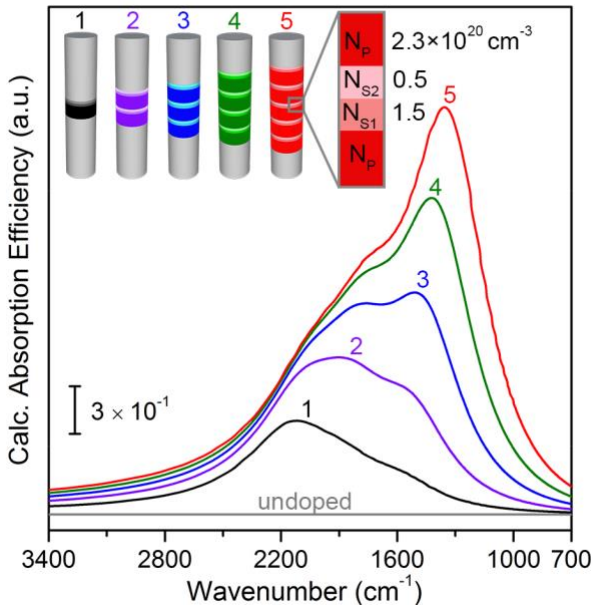

Figure 2.9 Effect of stepped carrier density profile. Calculated absorption efficiencies for individual Si nanowires containing 0 - 5 primary resonators (N_P = 2.3 × 10^{20} cm^{-3}) and spacer segments with a two-step carrier density gradient (N_{S1} = 1.5 × 10^{20} cm^{-3}, N_{S2} = 0.5 × 10^{20} cm^{-3}).

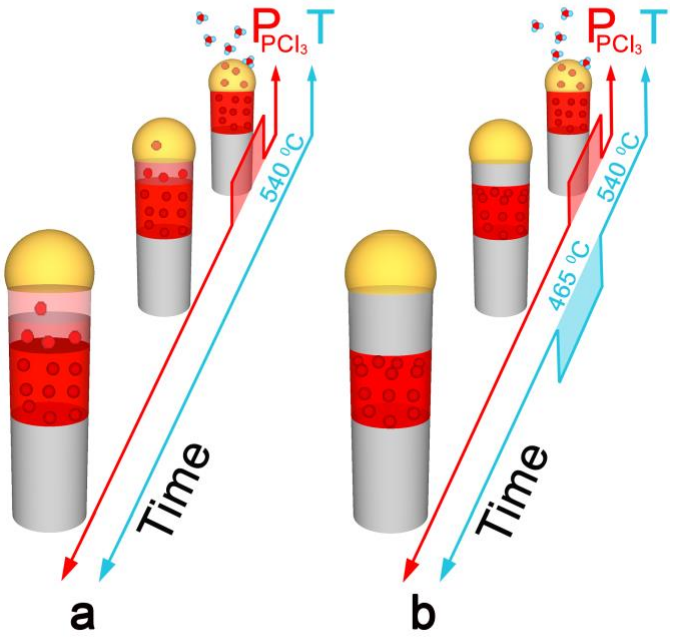

Figure 2.10 Schematic of single- and two-temperature nanowire growth protocols. (a) At high substrate temperature, phosphorus atoms remaining in the catalyst after termination of PCl_3 flow continue to incorporate into the nanowire. (b) A reduction of substrate temperature during spacer segment growth improves carrier density profile abruptness.

2.3.3 Mitigation of diffuse carrier gradients via two-temperature growth protocol

We next model the spacer segment as two domains with stepped carrier densities to more accurately capture the behavior seen in our experiments. Figure 2.9 displays simulations of absorption efficiency for Si nanowires with 0 - 5 primary resonators (N_P = 2.3×10^{20} cm^{-3}) separated by two 10 nm spacer segments (20 nm total) with carrier densities of $N_{S1} = 1.5 \times 10^{20}$ cm^{-3} and $N_{S2} = 0.5 \times 10^{20}$ cm^{-3}. The trends observed as a function of primary resonator number are consistent with the experimental data in Figure 2.5a and provide strong evidence that the interfaces between undoped and doped

segments exhibit graded carrier densities for our standard growth conditions. We attribute these axial carrier density gradients to the "reservoir effect." As illustrated in Figure 2.10a, upon terminating dopant precursor flow the concentration of dopant atoms inside the catalyst (*i.e.*, the reservoir) must be depleted. Recent studies indicate that these concentrations can be quite high (0.3 at. % P in an AuGe eutectic at 380 °C).[40] Residual atoms are incorporated into the nanowire as elongation continues, leading to an axial compositional gradient whose characteristic length is proportional to nanowire diameter and dopant atom concentration in the growth catalyst.[26, 27]

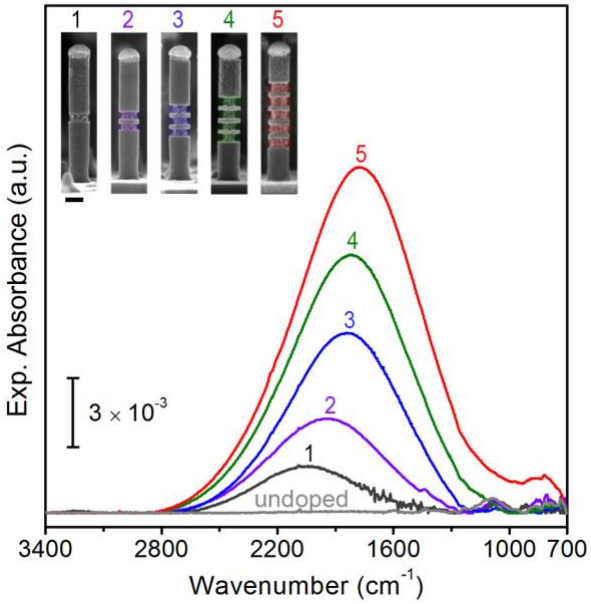

Figure 2.11 Demonstration of optically abrupt resonators. (a) Experimental spectral response for an array of Si nanowires each containing 0 - 5 primary resonators. Primary resonators and spacer segments are grown at a substrate temperature of 540 and 465°C, respectively. Inset: Side view SEM images of representative nanowires following a buffered oxide etch treatment to determine doped segment geometry.

A modified growth protocol, where the spacer segment is grown at a lower substrate temperature, minimizes the observed carrier density gradients. As displayed in

Figure 2.10b, we use substrate temperatures of 540 and 465 °C for segment growth with and without PCl_3 flow, respectively. Figure 2.11 shows that the experimental spectral responses for Si nanowires synthesized in this manner exhibit single peaks that redshift as the number of primary resonators increases. The agreement between these data and our simulations of nanowires with ideal dopant profiles (Figure 2.5b) indicates a substantial reduction of residual phosphorus in the spacer segment and improvement in profile abruptness. The mechanism by which dopant atoms inside the catalyst (*i.e.*, the reservoir) are depleted is beyond the scope of this work, but may occur *via* accelerated injection into the solid nanowire, ejection onto the nanowire sidewalls,[41] or evaporation to the gas phase.[42] While a residual phosphorus concentration in the spacer segment may still be on the order of 10^{18} cm^{-3}, and undetectable with the current approach, carrier densities below 1×10^{19} cm^{-3} do not significantly impact Si's dielectric function in the infrared.[38] Hence, we refer to resonators fabricated using the modulated temperature growth process as "optically abrupt" since the spectral response of these nanowires is indistinguishable from nanowires with ideal carrier density profiles.

2.4 Summary and Outlook

In this chapter, we characterized the effect of graded carrier densities on the LSPRs of phosphorus-doped Si nanowires with a combination of experimental spectral response measurements and DDA simulations. We showed the presence and impact of axially graded carrier density profiles on mid-infrared localized surface plasmon resonances in Si nanowires via coupled in situ spectral response measurements and

discrete dipole approximation calculations. A substantial concentration of dopant atoms is injected into the nanowire even after terminating dopant precursor delivery and results in absorption spectra with multiple, convoluted modes. A new fabrication protocol, which utilizes distinct temperatures for undoped and doped segment growth, overcomes this challenge and results in single absorption features as expected from scattering theory. These spectral responses can be considered "optically abrupt" since they are indistinguishable from those for nanowires with ideal, atomically abrupt carrier density profiles. Our findings pave the way for exploiting near-field interactions in Si-based plasmonic materials.

Our findings show that the spacer segment carrier density plays a critical role in determining LSPR properties of a Si nanowire, particularly in for series of resonators. This behavior is unique to the high aspect ratio doped Si nanowire plasmonic system, as the material symmetry of common plasmonic metal nanoparticles minimalizes the impact of their dielectric environment. The DDA calculations outlined here, indicate that the carrier density profile of a doped semiconductor system can be an effective route to dynamically modulate individual LSPR spectral response as well inter-LSPR interaction in system of coupled plasmonic resonators. The understanding and control of nanowire doping demonstrated here is particularly important for future applications leveraging near-field interactions, such as optical interconnects and molecular detection. [3, 43]

2.5 References

1. Link, S. and M.A. El-Sayed, *Shape and size dependence of radiative, non-radiative and photothermal properties of gold nanocrystals.* Int. Rev. Phys. Chem., 2000. **19**: p. 409-453.
2. Maier, S.A. and H.A. Atwater, *Plasmonics: Localization and guiding of electromagnetic energy in metal/dielectric structures.* J. Appl. Phys., 2005. **98**: p. 011101.
3. Schuller, J.A., et al., *Plasmonics for extreme light concentration and manipulation.* Nat. Mater., 2010. **9**: p. 193-204.
4. Naik, G.V., V.M. Shalaev, and A. Boltasseva, *Alternative plasmonic materials: Beyond gold and silver.* Adv. Mater., 2013. **25**: p. 3264-3294.
5. Naik, G.V. and A. Boltasseva, *Semiconductors for plasmonics and metamaterials.* Phys. Status Solidi-R., 2010. **4**: p. 295-297.
6. Faucheaux, J.A., A.L.D. Stanton, and P.K. Jain, *Plasmon resonances of semiconductor nanocrystals: Physical principles and new opportunities.* J. Phys. Chem. Lett., 2014. **5**: p. 976-985.
7. Pierret, R.F., *Semiconductor device fundamentals*. 1996, Reading, Mass.: Addison-Wesley. 792.
8. Hessel, C.M., et al., *Copper selenide nanocrystals for photothermal therapy.* Nano Lett., 2011. **11**: p. 2560-2566.
9. Llordes, A., et al., *Tunable near-infrared and visible-light transmittance in nanocrystal-in-glass composites.* Nature, 2013. **500**: p. 323-327.
10. Jain, P.K., et al., *Doped nanocrystals as plasmonic probes of redox chemistry.* Angew. Chem. Int. Edit., 2013. **52**: p. 13671-13675.

11. Babicheva, V.E., et al., *Towards cmos-compatible nanophotonics: Ultra-compact modulators using alternative plasmonic materials.* Optics Express, 2013. **21**: p. 27326-27337.

12. Tice, D.B., et al., *Ultrafast modulation of the plasma frequency of vertically aligned indium tin oxide rods.* Nano Lett., 2014. **14**: p. 1120-1126.

13. Chou, L.-W., et al., *Tunable mid-infrared localized surface plasmon resonances in silicon nanowires.* Journal of the American Chemical Society, 2012. **134**(39): p. 16155-16158.

14. Maier, S.A., et al., *Observation of near-field coupling in metal nanoparticle chains using far-field polarization spectroscopy.* Phys. Rev. B, 2002. **65**: p. 193408.

15. Sonnichsen, C., et al., *A molecular ruler based on plasmon coupling of single gold and silver nanoparticles.* Nat. Biotechnol., 2005. **23**: p. 741-745.

16. Jain, P.K., S. Eustis, and M.A. El-Sayed, *Plasmon coupling in nanorod assemblies: Optical absorption, discrete dipole approximation simulation, and exciton-coupling model.* J. of Phys. Chem. B, 2006. **110**: p. 18243-18253.

17. Halas, N.J., et al., *Plasmons in strongly coupled metallic nanostructures.* Chem. Rev., 2011. **111**: p. 3913-3961.

18. Willets, K.A. and R.P. Van Duyne, *Localized surface plasmon resonance spectroscopy and sensing.* Annu. Rev. Phys. Chem., 2007. **58**: p. 267-297.

19. Kauranen, M. and A.V. Zayats, *Nonlinear plasmonics.* Nat. Photonics, 2012. **6**: p. 737-748.

20. Kale, M.J., T. Avanesian, and P. Christopher, *Direct photocatalysis by plasmonic nanostructures.* ACS Catal., 2014. **4**: p. 116-128.

21. Jain, P.K., W.Y. Huang, and M.A. El-Sayed, *On the universal scaling behavior of the distance decay of plasmon coupling in metal nanoparticle pairs: A plasmon ruler equation.* Nano Lett., 2007. **7**: p. 2080-2088.

22. Kodambaka, S., et al., *Diameter-independent kinetics in the vapor-liquid-solid growth of si nanowires.* Phys. Rev. Lett., 2006. **96**: p. 096105.

23. Schmidt, V., J.V. Wittemann, and U. Gosele, *Growth, thermodynamics, and electrical properties of silicon nanowires.* Chem. Rev., 2010. **110**: p. 361-388.

24. Shi, J. and X.D. Wang, *Functional semiconductor nanowires via vapor deposition.* J. Vac. Sci. Technol. B, 2011. **29**: p. 060801.

25. Chou, L.W. and M.A. Filler, *Engineering multimodal localized surface plasmon resonances in silicon nanowires.* Angew. Chem. Int. Edit., 2013. **52**: p. 8079-8083.

26. Li, N., T.Y. Tan, and U. Gosele, *Transition region width of nanowire hetero- and pn-junctions grown using vapor-liquid-solid processes.* Appl. Phys. a-Mater., 2008. **90**: p. 591-596.

27. Clark, T.E., et al., *Diameter dependent growth rate and interfacial abruptness in vapor-liquid-solid si/si(1-x)ge(x) heterostructure nanowires.* Nano Lett., 2008. **8**: p. 1246-1252.

28. Wen, C.Y., et al., *Formation of compositionally abrupt axial heterojunctions in silicon-germanium nanowires.* Science, 2009. **326**: p. 1247-1250.

29. Perea, D.E., et al., *Controlling heterojunction abruptness in vls-grown semiconductor nanowires via in-situ catalyst alloying.* Nano Lett., 2011. **11**: p. 3117-3122.

30. Dick, K.A., et al., *Controlling the abruptness of axial heterojunctions in iii-v nanowires: Beyond the reservoir effect.* Nano Lett., 2012. **12**: p. 3200-3206.

31. Chou, L.W., et al., *Influence of dielectric anisotropy on the absorption properties of localized surface plasmon resonances embedded in si nanowires.* J. Phys. Chem. C, 2014. **118**: p. 5494-5500.

32. Xie, P., et al., *Diameter-dependent dopant location in silicon and germanium nanowires.* P. Natl. Acad. Sci. USA, 2009. **106**: p. 15254-15258.

33. Gan, Z.F., et al., *Mapping electrostatic profiles across axial p-n junctions in si nanowires using off-axis electron holography.* Appl. Phys. Lett., 2013. **103**: p. 153108.

34. Amit, I., et al., *Spatially resolved correlation of active and total doping concentrations in vls grown nanowires.* Nano Lett., 2013. **13**: p. 2598-2604.

35. Koren, E., et al., *Obtaining uniform dopant distributions in vls-grown si nanowires.* Nano Lett., 2011. **11**: p. 183-187.

36. Chou, L.W., et al., *Tunable mid-infrared localized surface plasmon resonances in silicon nanowires.* J. Am. Chem. Soc., 2012. **134**: p. 16155-16158.

37. Shin, N. and M.A. Filler, *Controlling silicon nanowire growth direction via surface chemistry.* Nano Lett., 2012. **12**: p. 2865-2870.

38. Palik, E.D. and G. Ghosh, *Handbook of optical constants of solids*. 1998, San Diego: Academic Press. 999.

39. Wei, Q.H., et al., *Plasmon resonance of finite one-dimensional au nanoparticle chains.* Nano Lett., 2004. **4**: p. 1067-1071.

40. Connell, J.G., et al., *Identification of an intrinsic source of doping inhomogeneity in vapor-liquid-solid-grown nanowires.* Nano Lett., 2013. **13**: p. 199-206.

41. Kodambaka, S., et al., *Germanium nanowire growth below the eutectic temperature.* Science, 2007. **316**: p. 729-732.

42. Christesen, J.D., et al., *Encoding abrupt and uniform dopant profiles in vapor-liquid-solid nanowires by suppressing the reservoir effect of the liquid catalyst.* Acs Nano, 2014. **8**: p. 11790-8.

43. Mayer, K.M. and J.H. Hafner, *Localized surface plasmon resonance sensors.* Chem. Rev., 2011. **111**: p. 3828-3857.

CHAPTER 3.

EXTREME LOCALIZED SURFACE PLASMON COUPLING IN DOPED SI NANOWIRES

3.1 Introduction

3.1.1 Motivation

LSPRs supported by small metallic particles provide a route to enhance the sensitivity of chemical detectors,[1, 2] activity of heterogeneous catalysts,[3, 4] and compactness of waveguides[5, 6]. These opportunities emerge from two key properties of the LSPR: (i) deep sub-wavelength photon confinement and (ii) enhanced local electric fields.[7] The near-field coupling between closely spaced resonators enables further light focusing, stronger local electric fields, and energy transport via dipolar coupling.[8-10] The term 'near-field coupling' is used to designate a Coulombic coupling mechanism between electric fields at the surfaces of adjacent LSPRs. These interactions are a strong function of resonator size and separation,[11-13] with larger resonators and/or shorter inter-resonator distances resulting in stronger coupling. However, these are conflicting requirements for many applications – large electric fields are often desired in the smallest possible footprint. Obtaining the largest local electric fields also necessitates that neighboring resonators be separated by nanometer, or even sub-nanometer, gaps, and this degree of precision continues to be challenging in high-volume manufacturing environments.

3.1.2 Plasmon ruler equation analysis of LSPR interaction

The near-field coupling strength of dipolar LSPRs can be determined (in the quasi-static limit) by analyzing far-field spectral response measurements with the so-called "plasmon ruler" equation,[12-14] which describes the relationship between absorption peak position and resonator spacing:

$$\frac{w - w_0}{w_0} = A \cdot \exp\left[\frac{-S/L}{t}\right] \quad (1)$$

where ω_0 is the peak absorption frequency for an isolated resonator of length L and ω is the peak absorption frequency for two resonators of length L, separated by a distance S. A is a dimensionless constant of proportionality. τ is known as the decay length scaling factor, a dimensionless parameter that describes the rate at which the electric field decays away from the surface of each resonator. Larger values of τ indicate longer electric field decay lengths and stronger near-field coupling interactions. Previous work supports the validity of Equation 1 for coupled *dipolar* LSPRs in purely isotropic (e.g., nanoparticles dispersed in solution)[15-19] as well as anisotropic (e.g., patterned metal particles on a substrate) dielectric environments[20-23]. Most importantly, τ is found to be nearly independent of nanoparticle size, shape, metal, and surrounding dielectric.[14, 23-27] Closely spaced sphere, disk, and pyramid dimers comprised of either Au or Ag all exhibit τ values in the 0.2 - 0.3 range. Hence, the LSPR near-field decays over a distance about 1/5 to 1/3 of the resonator size.[23, 27]

Doped semiconductors are promising plasmonic materials for applications in the mid- to near-infrared spectral regime.[28-30] We previously demonstrated mid-infrared LSPRs supported by fully and partially doped Si nanowires synthesized by the bottom-up

vapor-liquid-solid (VLS) technique.[31-33] The programmability of axial dopant profile presents unique opportunities to both manipulate and understand near-field coupling interactions in doped-semiconductor nanostructures. Here, we combine *in situ* infrared spectroscopy and discrete dipole approximation (DDA) calculations to characterize the coupling of doped Si resonators embedded along the length of Si nanowires.

3.2 Experimental methods

3.2.1 Doped Si nanowire preparation

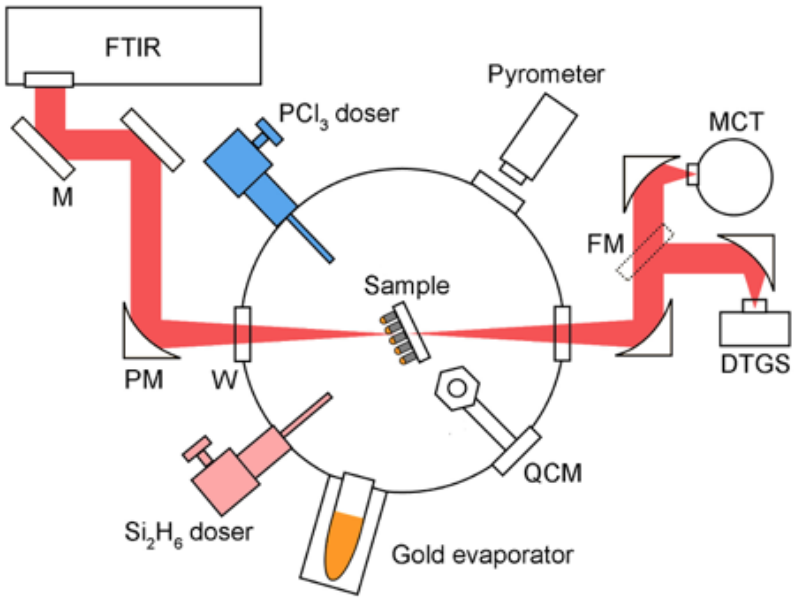

Figure 3.1 Chemical-vapour-deposition chamber *in situ* infrared spectroscopy system schematic.

A Si (111) substrate (El-Cat, FZ, 15-30 Ω-cm, double side polished) is cleaned by a 5 minute immersion in 10% HF (J.T. Baker) and subsequently rinsed in deionized water prior to insertion into a ultrahigh vacuum (UHV) chamber.[34] The substrate is degassed at

700 °C for 1 hour and then flash-annealed at 1200 °C for 30 seconds in vacuum. After cooling the substrate at a rate of less than 2 °C/s, a thin film of Au (ESPI Metals, 99.999%) is deposited at a rate of ~1 Å/min using a high temperature effusion cell (SVT Associates). Si nanowires containing one or two doped segments, each 100 nm in length, are then fabricated using the vapor-liquid-solid technique in a two-step process. In the first step, Au film break up and nanowire nucleation is accomplished by ramping to, and holding the substrate temperature at 620 °C while maintaining Si_2H_6 (Voltaix, 99.998%) at a pressure of 4×10^{-5} Torr for 2 min. Nanowire areal densities and mean diameters of ~1 nanowire/μm^2 and 130 nm are obtained using this procedure. In the second step, the substrate temperature is lowered to 470 °C with the Si_2H_6 partial pressure fixed at 4×10^{-5} Torr. These conditions result in a nanowire growth rate of ~4 nm/min. Each phosphorus-doped segment is encoded by introducing PCl_3 (Strem Chemicals, 99.999%) at a partial pressure of 3×10^{-6} Torr for 25 min. PCl_3 does not strongly impact nanowire growth rate.[35] Precursor partial pressures are not corrected for ion gauge sensitivity.

3.2.2 LSPR spectral response characterization

We measure the far-field absorption spectra of as-grown nanowire arrays at room temperature immediately following growth in vacuum using *in situ* infrared spectroscopy (Bruker, Vertex 70).[32, 33, 36] Unpolarized light from a standard SiC globar source is combined with a KBr beam-splitter and a liquid nitrogen-cooled HgCdTe detector to collect spectra between 700 and 3600 cm^{-1}. All spectra are recorded with a resolution of 4 cm^{-1}, at an incidence angle of 58° to access the longitudinal localized surface plasmon resonance (LSPR) mode, and are baseline corrected using a concave rubberband method. After synthesis and spectral response measurement, nanowire arrays are removed from

the UHV system and treated with buffered oxide etch (BOE, J.T. Baker 7:1) solution to reveal doped segment geometry. Nanowire morphology before and after BOE treatment is examined using a Zeiss Ultra 60 field-emission scanning electron microscope (SEM).

The spectral responses of the doped Si nanowires are simulated within the discrete dipole approximation using the FLTRCD method available in the DDSCAT 7.3 code.[36] Nanowires are modeled as ideal cylinders with overall and doped segment dimensions matching experiment and the incident electric field is polarized along the nanowire axis (i.e., longitudinally). Single nanowire calculations are appropriate for this investigation since array areal densities are sufficiently low (~ 1 nanowire/μm^2) such that inter-nanowire LSPR interactions can be neglected.[31] The refractive indices (n) and extinction coefficients (k) of undoped and doped Si segments are obtained from Palik[37] and an extended Drude model,[33] respectively. Unless otherwise noted, a grid spacing of 10 nm is used in all calculations and a conjugate gradient iteration is completed until achieving an error tolerance below 10^{-5}.

3.3 Results and Discussion

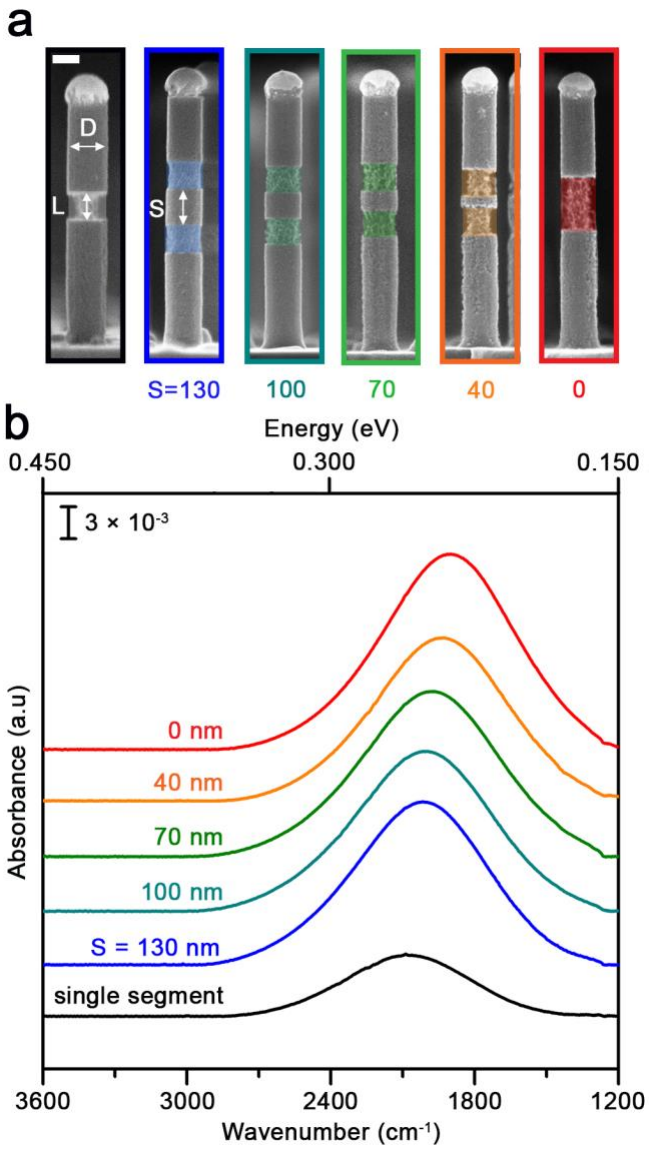

Figure 3.2 Redshift of absorption frequency for coupled LSPRs in Si nanowires. (a) Side view SEM images of representative Si nanowires following a buffered oxide etch treatment to determine doped segment geometry (AR = 0.8) and separation distance (130, 100, 70, 40, and 0 nm). Scale bar, 100 nm. (b) Spectral response measurements of the longitudinal LSPR mode for arrays of the Si nanowires shown in (a).

3.3.1 LSPR coupling of resonators embedded in a Si nanowire

Figure 3.2a displays representative scanning electron microscope (SEM) images of epitaxial Si nanowires containing one or two phosphorus-doped segments. These images are taken *following* a buffered oxide etch (BOE) treatment that reveals resonator placement and dimensions. All resonators exhibit a length of 100 nm, which corresponds to an aspect ratio (AR) of 0.8. Figure 3.2b displays *in situ* spectral response measurements, acquired immediately after growth and *before* BOE treatment, for the nanowire arrays in Figure 3.2a. As described in the Methods, these measurements are sensitive to LSPRs with dipoles oriented along the nanowire length (i.e., longitudinally). Si nanowires containing a single doped segment exhibit a single LSPR absorption feature centered at 2088 cm^{-1} (ω_0), consistent with a carrier density of 2.7×10^{20} cm^{-3}. Similar to previous reports[12-14] and as expected from dipole-dipole coupling theory,[11, 24] the absorption peak position for neighboring resonators (ω) redshifts with decreasing resonator separation distance (S).

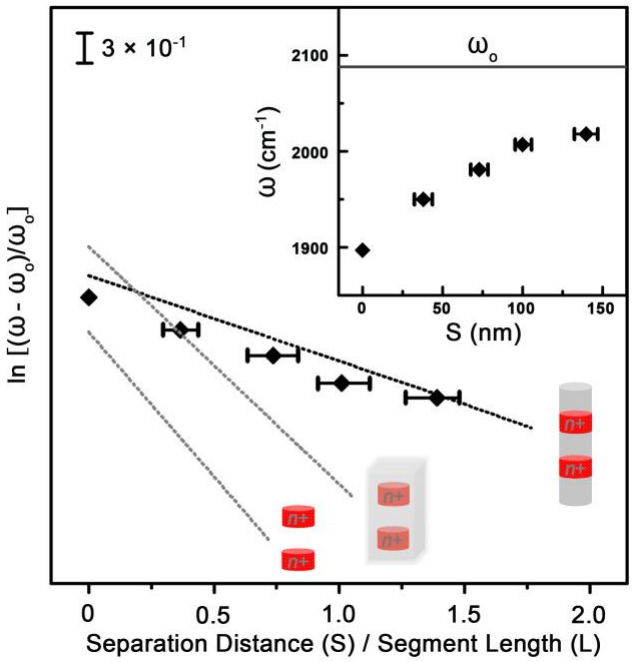

Figure 3.3 Determination of decay length scaling factor. Experimental absorption peak frequencies and doped Si resonator separation distances are extracted from Figure 3.2, as shown in the inset, and plotted according to a linearized form of Eq. 1. τ can be extracted from the slope of these points. Error bars are for one standard deviation. A linear fit to calculated absorption peak frequencies for doped Si segments embedded in a nanowire, isotropic vacuum, and isotropic Si are shown as dotted lines.

We use the plasmon ruler equation, as shown in Figure 3.3, to determine the decay length scaling factor (τ) for our embedded resonators. Eq. 1 is linearized and the ω values from Figure 1 are plotted accordingly. We find that the value of τ, which can be extracted from the slope, is 1.4 for this resonator geometry and carrier density. Consistent with these data, calculations yield an absorption peak redshift as resonator spacing decreases as shown in Figure 3.4 and a τ value of 1.7. However, as seen in Figure 3.3, LSPRs supported by doped Si resonators placed in an isotropic dielectric that is either vacuum or intrinsic Si exhibit τ values of ~0.4. These values are in line with published results for noble metals[14, 27] and $Cu_{2-x}S$ nanodisks.[38] The τ value for coupled resonators

embedded in isotropic Si is determined from one of two dipolar resonances as shown in Figure 3.5. The motivation for, and validity of, this approach is outlined in detail next.

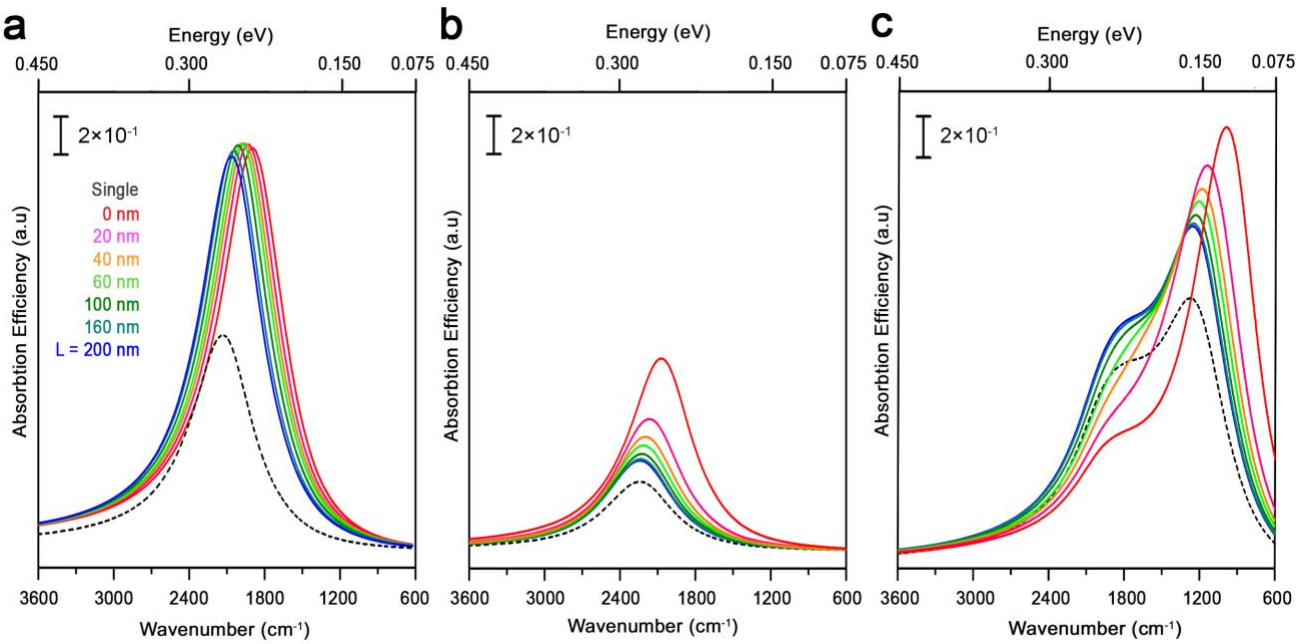

Figure 3.4. Calculated absorption efficiency spectra for coupled Si resonators as a function of resonator separation in (a) Si nanowire, (b) isotropic vacuum, and (c) isotropic Si dielectric environments. Resonator aspect ratios and carrier densities are all 0.8 and 2.7 × 10^{20} cm^{-3}, respectively. Calculated absorption efficiencies for isolated resonators with the same geometry and carrier density are included in each plot for comparison (black dotted curves). To match the dimensions of nanowires obtained experimentally, calculations are performed for cylindrical nanowires with a diameter and length of 130 and 950 nm, respectively.

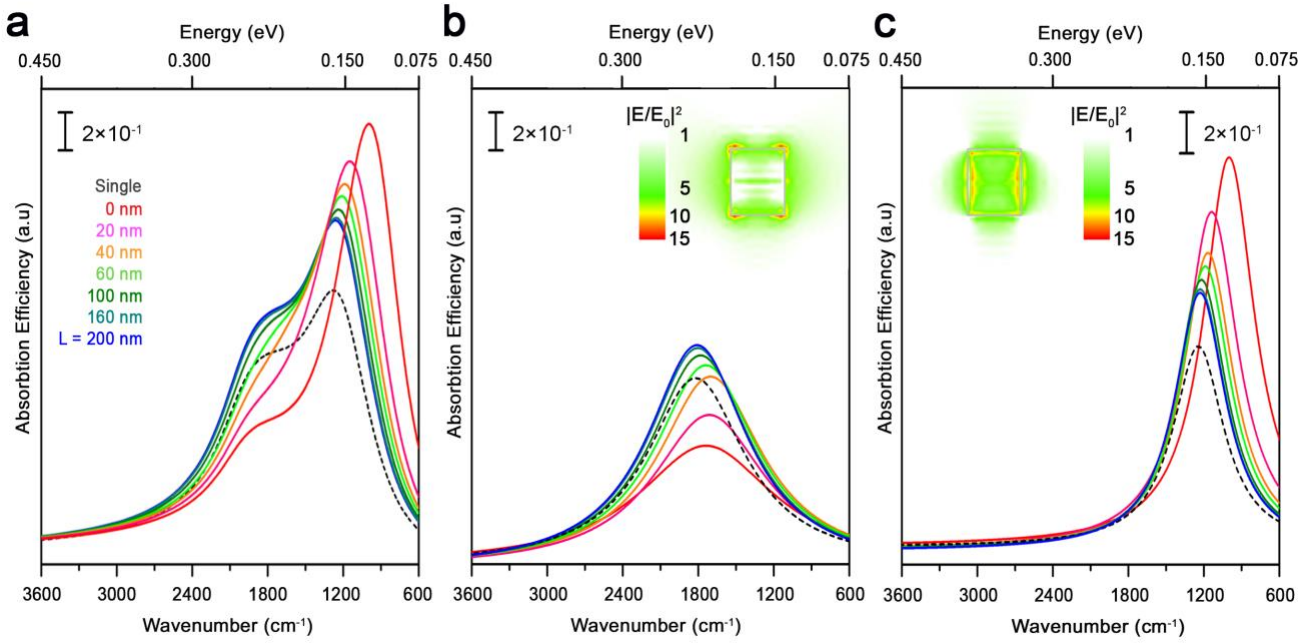

Figure 3.5 (a) Calculated absorption efficiency spectra for coupled Si resonators as a function of resonator separation in isotropic Si. Resonator aspect ratio and carrier density are 0.8 and 2.7 × 10^{20} cm^{-3}, respectively. The (b) higher and (c) lower energy absorption modes extracted by peak fitting the data in (a) with two Lorentzian functions. The spectra in (c) are the basis of the plasmon ruler curve for coupled resonators embedded in isotropic Si shown in Figure 3.3. The insets in (b) and (c) show the calculated field enhancement maps for isolated resonators.

3.3.2 Dielectric anisotropy effects

Figure 3.5a reveals that two LSPRs exist for coupled Si resonators embedded in isotropic Si. The field enhancement maps shown in the insets to Figures 3.5b and 3.5c confirms that both modes are dipolar. To determine a τ value for each mode, the frequency of each mode can be extracted via standard fitting procedures as a function of resonator spacing. As seen in Figure 3.5c and expected for coupled dipolar resonators, the stronger, low energy dipolar mode undergoes a monotonic redshift as resonator spacing is reduced. The τ value extracted for this mode is 0.4, as shown in Figure 3.3, and is

consistent with prior studies of isotropic dielectric environments. However, Figure 3.5b shows that the weaker, high energy dipolar mode first redshifts and then blue-shifts as resonator spacing decreases. We attribute this complex behavior to a convolution of near-field coupling and energy sharing with the low energy mode, which is energetically similar. Unfortunately, this behavior precludes a straightforward determination of τ for this mode.

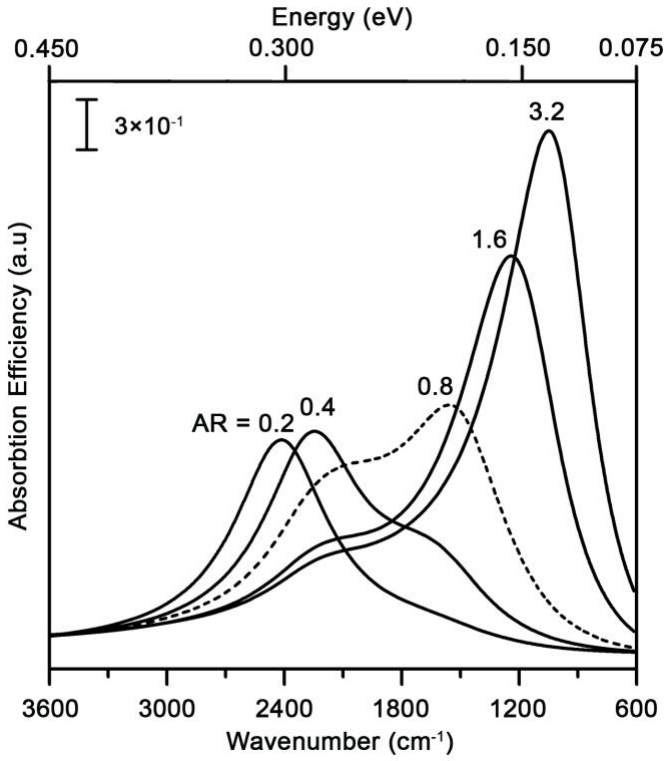

Figure 3.6. Absorption efficiency spectra calculated for single Si resonators embedded in isotropic Si. Each resonator has a carrier density of 2.7×10^{20} cm^{-3} and aspect ratios between 0.2 and 3.2.

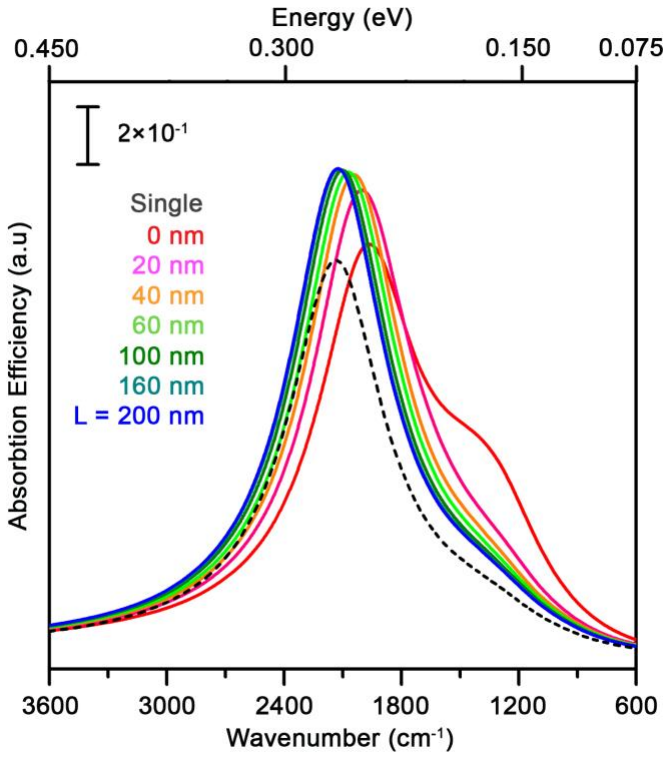

Figure 3.7 Absorption efficiency spectra calculated for coupled Si resonators embedded in isotropic Si as a function of separation distance. Resonator aspect ratio and carrier density are 0.2 and 2.7 × 10^{20} cm^{-3}, respectively. Calculated absorption efficiencies for isolated resonators with the same geometry and carrier density are included in each plot for comparison (black dotted curves).

To better understand the coupling of resonators in isotropic Si environments, Figure 5 shows the calculated spectral responses of isolated resonators for several aspect ratios. An aspect ratio of 0.8, which was used in experiment, yields modes of similar absorption efficiency. For this situation, one would expect the largest amount of energy sharing, which likely prevents a monotonic redshift as resonator spacing is reduced (*vide supra*). However, mode absorption efficiencies become increasingly distinct as aspect ratio is either increased or decreased from 0.8. As an example, shown in Figure 3.6, we calculated the spectral response for coupled resonators with an aspect ratio of 0.2 as a

function of resonator spacing. Figure 3.7 shows the spectral response for each mode, as extracted via peak fitting. Here, as expected for simple dipolar coupling, both modes monotonically redshift as resonator spacing decreases.

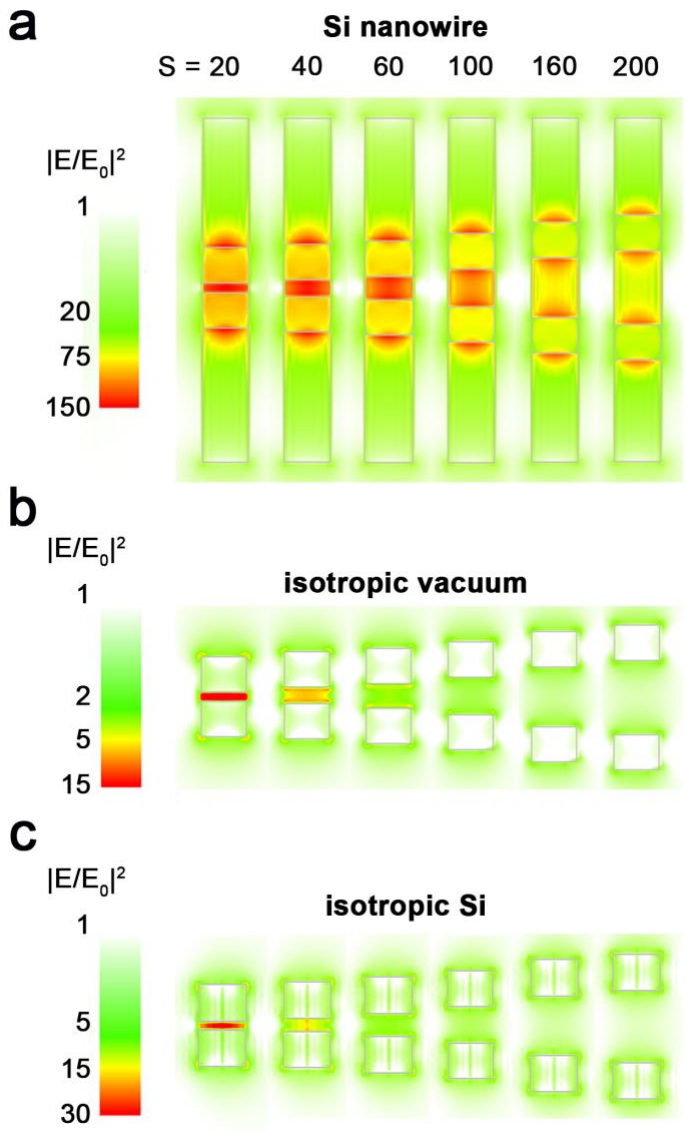

Figure 3.8 Calculated electric field enhancement maps for coupled Si resonators as a function of resonator separation in (a) Si nanowire, (b) isotropic vacuum, and (c) isotropic Si dielectric environments. Resonator aspect ratios and carrier densities are 0.8 and 2.7 × 10^{20} cm^{-3}, respectively. Each map is calculated at the frequency where

absorption efficiency is at a maximum. Field enhancement magnitude is indicated by a red-to-green gradient.

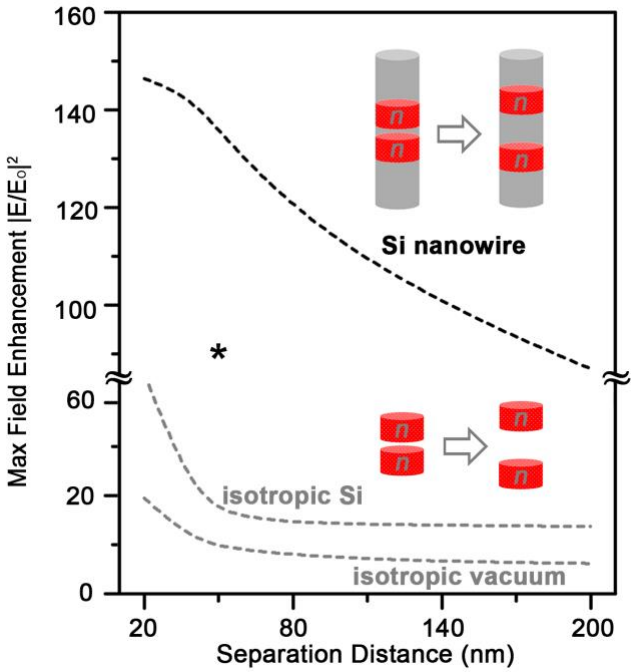

Figure 3.9 Comparison of LSPR coupling in Si nanowires, isotropic vacuum, and isotropic Si. Maximum field enhancement for coupled Si resonators as a function of resonator separation in a Si nanowire, isotropic vacuum, and isotropic Si. The corresponding electric field enhancement maps are shown in Figure 3.8. The star at a separation distance of 60 nm indicates the approximate field enhancement obtained in the vacuum cut-out of the nanowire shown in Figure 3.11. To match the dimensions of nanowires obtained experimentally, calculations are performed for cylindrical nanowires with a diameter and length of 130 and 950 nm, respectively.

The nanowire structure enables an approximately 4-5-fold increase in near-field decay length. For nanowires, the structural anisotropy and large permittivity of intrinsic Si (n = 3.4) leads to a strong concentration of the electric field in the volume between adjacent resonators as shown in Figure 3.8a. This behavior greatly enhances the near-

field coupling strength. For equivalent resonators placed in an isotropic vacuum as shown in Figure 3.8b or isotropic Si shown in Figure 3.8c, the largest field enhancements occur near the resonator corners, which prevents the same degree of coupling. In both the nanowire and isotropic Si cases, the resonators are axially separated by a high permittivity medium (i.e., Si). However, in the later case, the presence of intrinsic Si in the radial direction results in an image dipole that counteracts and defocuses the field.[31,39] As shown in Figure 8, and expected from the preceding discussion, resonators embedded in nanowires yield local fields stronger than resonators in an isotropic vacuum *for the same spacing*. While the maximum enhancement for isotropic vacuum asymptotes at a value of ~10 at resonator separations above 50 nm, resonators embedded in a Si nanowire separated by a distance of 200 nm still support field enhancements of approximately 90.

3.3.3 Coupled LSPR near-field enhancement

DDA allows us to explore the role of nanowire structure on near-field interactions. We determine τ values for doped Si resonators embedded in GaAs (n = 3.2), Si (3.4), and Ge (4.1) nanowires, or an isotropic vacuum, as a function of the resonator aspect ratio and carrier density. We choose these materials since the VLS growth of nanowires is possible for each.[40, 41] Figure 3.5a shows that small AR resonators yield the largest decay length scaling factors. This behavior is expected from the plasmon ruler equation (i.e., as L decreases at constant S, τ must increase) and has been observed for Au nanorods.[26] Resonators embedded in nanowires amplify this effect due to their anisotropic structure. Figure 3.5b shows that increasing carrier density yields larger τ values. Coupling increases because the plasma frequency (ω_p), and therefore the

polarizability, of each resonator increases with carrier density.[42] Figures 3.10a and 3.10b also show that τ increases with the permittivity of the embedding nanowire material.[8,25]

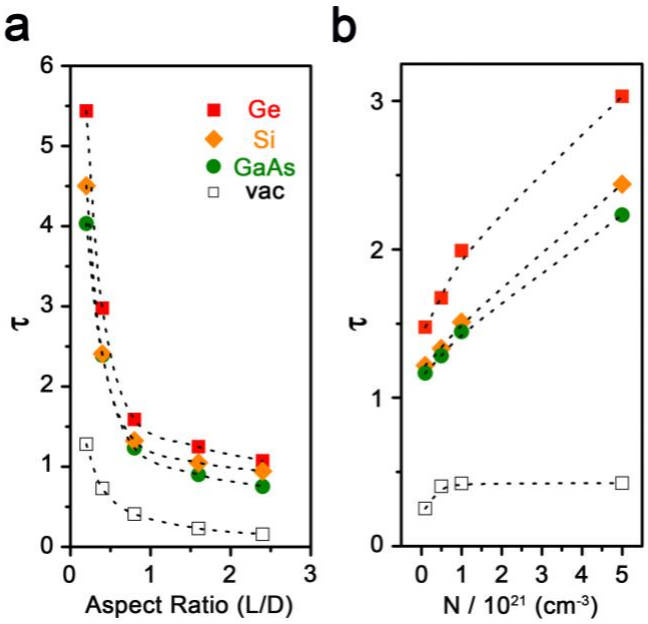

Figure 3.10 Near-field decay length scaling factor (τ). Calculation results plotted as a function of doped Si resonator (a) aspect ratio (for $n = 3 \times 10^{20}$ cm^{-3}) and (b) carrier concentration (for AR = 0.8). Red squares, orange diamonds, and green circles represent doped Si resonators embedded in Ge, Si, and GaAs nanowires, respectively. Open black squares represent equivalent doped Si resonators in an isotropic vacuum. Calculations are performed for cylindrical nanowires with a diameter and length of 150 and 1500 nm, respectively.

3.3.4 Anisotropic dielectric engineering advantages

The benefits of enhanced decay length scaling factors become clear when considering the needs of devices that leverage near-field plasmon interactions such as waveguides, chemical sensors, and photodetectors. Maximizing the interaction strength, and thereby the distance over which energy can be transported, is critical for sub-wavelength waveguides.[43, 44] More specifically, Ohmic losses demand as few plasmonic

resonators as possible per unit waveguide length. A 4-5x larger near-field decay length, as observed here, allows a 4-5x increase in inter-nanoparticle distance and, therefore, a concomitant increase in energy transport distance. Calculations are currently underway in our laboratory to quantitatively understand and predict the performance (e.g., propagation length) of sub-wavelength doped nanowire waveguides.

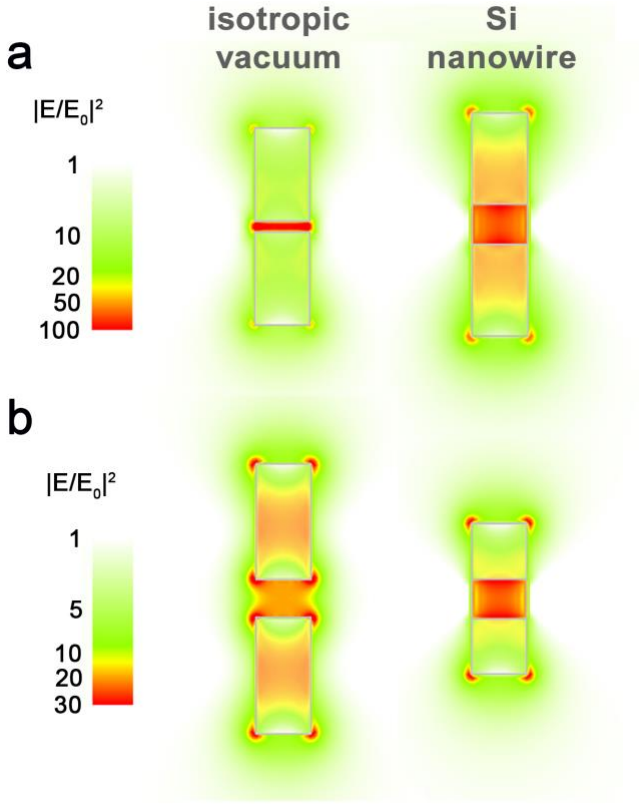

Figure 3.11 Advantages of structural anisotropy. Calculated electric field enhancement maps for the longitudinal mode of cylindrical doped Si resonators each with a carrier concentration of 2.7×10^{20} cm^{-3}. (a) Equivalent field enhancement magnitudes (~ 100) are calculated between two resonators with AR = 1.6 separated by 20 nm of vacuum and 100 nm of Si. (b) Equivalent field enhancement magnitudes (~ 30) are achieved between two resonators of AR = 1.6 (length = 240 nm) separated by vacuum and AR = 1.0 (length = 150 nm) separated by Si.

Our results also show how anisotropic structures, such as nanowires, can improve the sensitivity and reduce the physical size of plasmon-based chemical sensors and

photodetectors. As discussed above (Figure 3.9), nanowires offer higher local electric fields, and therefore sensitivities, for the same resonator spacing. Alternatively, anisotropy can relax the precision required of the fabrication process (e.g., lithography and etching),[10, 18] since it provides the same local electric field at larger resonator spacing. For example, as shown in Figure 3.11a, resonators of the same geometry (AR = 1.6) separated by 100 nm in a Si nanowire and 20 nm in an isotropic vacuum yield the same maximum local field enhancement. Increasing resonator length can also strengthen local electric fields, but this increases overall device size. Figure 3.11b shows that doped Si resonators separated by a segment of intrinsic Si achieve field enhancements equivalent to that of 60% larger resonators in an isotropic vacuum.

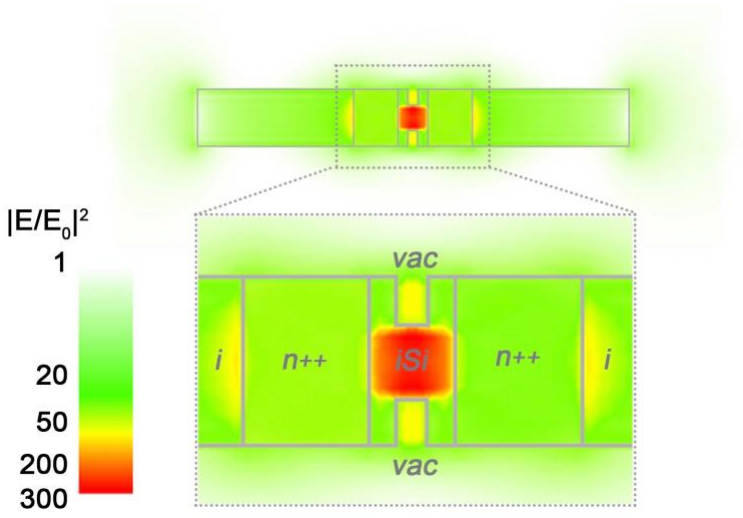

Figure 3.12 Calculated electric field enhancement map for coupled Si resonators separated by 60 nm with a 40 nm deep radial cut-out comprised of vacuum. Resonator aspect ratio and carrier density are 0.8 and 2.7 × 10^{20} cm^{-3}, respectively. Field enhancement magnitude is indicated by a red-to-green gradient.

It must be noted that optically active materials must be placed in, or molecules must access, the region of highest electric field (i.e., inside the intrinsic Si separating the doped segments) for photon and chemical detectors, respectively. VLS is well equipped to insert thin layers of other photo-active semiconductors[45-47] and recent work shows a new route to embed silicides.[48] Selective etching can enable the small radial cut-outs necessary for mass transport into and out of the high field region.[49] The introduction of a cut-out consisting of a low permittivity medium (e.g., gas) will reduce the extent of light focusing and field enhancement, as seen in Figure 3.12. However, for this structure, as indicated by the star in Figure 3.4, the maximum electric fields located in the cut-outs exceed those for the same resonators embedded in an isotropic medium by ~8 times.

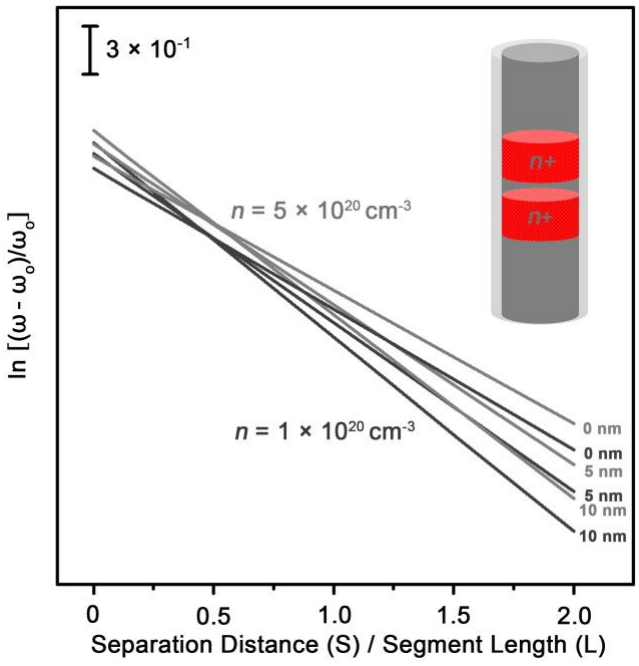

Figure 3.13 Effect of a uniform intrinsic Si shell on the decay length scaling factor. Calculated LSPR peak positions for nanowires containing coupled doped-Si segments fitted to a linearized form of equation 1. Resonator carrier densities of 1×10^{20} cm^{-3} (black) or 5×10^{20} cm^{-3} (gray) and nanowire shell thicknesses of 0, 5, and 10 nm are shown. Calculations are performed for cylindrical nanowires with a diameter and length

of 130 and 950 nm, respectively. A periodic grid spacing of 5 nm was used for these calculations.

3.3.5 Conformal Si deposition effects

The small differences in the decay length scaling factors determined from experiment and simulation (Figure 3.3) are also worthy of discussion. We attribute this behavior to the non-idealities of semiconductor nanowire growth via the vapor-liquid-solid technique. A small amount of sidewall deposition (< 10 nm) cannot be ruled out, and will produce an image dipole that damps the LSPR.[31,39] This behavior reduces near-field coupling strength, as seen for coupled resonators embedded in Si nanowires with 5 and 10 nm intrinsic Si shells as shown in Figure 3.13. Notably, VLS growth likely yields a shell whose thickness depends on axial position (due to the concurrent elongation of the nanowire) and/or contains additional carriers (due to PCl_3 decomposition on the sidewall). Nonetheless, careful control of nanowire structure will be crucial to obtain the highest near-field coupling strengths.

3.4 Summary and Outlook

The so-called "plasmon ruler" is widely used to measure nanoscale distances in the chemical and biological sciences. This measurement relies on the near-field coupling of neighboring plasmonic resonators and, as shown in many previous reports, that the scaling behavior of these interactions is nearly universal (i.e., independent of material, dielectric environment, etc.). We have experimentally shown that the near-field decay length scaling factor determined using the plasmon ruler equation for doped Si resonators

embedded in Si nanowires exceeds the well known "universal" value for noble metals in the UV/visible by 4-5 times. The anisotropic structure of semiconductor nanowires and large permittivity of intrinsic Si in the infrared underlies this behavior.

Foremost, our experiments demonstrate that the plasmon coupling scaling applys only to isotropic dielectric environments. Complex structures, including Si nanowires, require a more thorough exploration of their near-field coupling behavior. Our results indicate that use of the plasmon ruler to measure nanoscale distance, without ensuring that the dielectric environment is truly isotropic, may lead to experimental errors. The enhanced LSPR near-field interactions demonstrated here in Si nanowires enable deep sub-wavelength confinement of light using a system of resonators with a smaller total volume and/or increased spacing, in comparison to equivalent resonators in an isotropic medium. The dielectric anisotropy effects offer improved device compactness and less stringent lithographic precision benchmarks, which are often on the single nanometer scale for extreme focusing. Our findings offer several new design options for plasmon-based detectors, catalysts, and waveguides.

3.5 References

1. Mayer, K.M. and J.H. Hafner, *Localized surface plasmon resonance sensors.* Chemical Reviews, 2011. **111**(6): p. 3828-3857.
2. Baldassarre, L., et al., *Midinfrared plasmon-enhanced spectroscopy with germanium antennas on silicon substrates.* Nano Letters, 2015. **15**(11): p. 7225-7231.

3. Linic, S., et al., *Photochemical transformations on plasmonic metal nanoparticles.* Nature Mat., 2015. **14**(7): p. 744-744.

4. Mukherjee, S., et al., *Hot-electron-induced dissociation of h-2 on gold nanoparticles supported on sio2.* Journal of the American Chemical Society, 2014. **136**(1): p. 64-67.

5. Maier, S.A. and H.A. Atwater, *Plasmonics: Localization and guiding of electromagnetic energy in metal/dielectric structures.* Journal of Applied Physics, 2005. **98**(1): p. 011101.

6. Apuzzo, A., et al., *Observation of near-field dipolar interactions involved in a metal nanoparticle chain waveguide.* Nano Letters, 2013. **13**(3): p. 1000-1006.

7. Gramotnev, D.K. and S.I. Bozhevolnyi, *Plasmonics beyond the diffraction limit.* Nat. Photon., 2010. **4**(2): p. 83-91.

8. Schuller, J.A., et al., *Plasmonics for extreme light concentration and manipulation.* Nat. Mater., 2010. **9**(3): p. 193-204.

9. Alu, A., P.A. Belov, and N. Engheta, *Coupling and guided propagation along parallel chains of plasmonic nanoparticles.* New J. of Phys., 2011. **13**: p. 033026.

10. Mayer, K.M. and J.H. Hafner, *Localized surface plasmon resonance sensors.* Chem. Rev., 2011. **111**(6): p. 3828-3857.

11. Nordlander, P., et al., *Plasmon hybridizaton in nanoparticle dimers.* Nano Lett., 2004. **4**(5): p. 899-903.

12. Rechberger, W., et al., *Optical properties of two interacting gold nanoparticles.* Opt. Commun., 2003. **220**(1-3): p. 137-141.

13. Su, K.H., et al., *Interparticle coupling effects on plasmon resonances of nanogold particles.* Nano Lett., 2003. **3**(8): p. 1087-1090.

14. Gunnarsson, L., et al., *Confined plasmons in nanofabricated single silver particle pairs: Experimental observations of strong interparticle interactions.* J. Phys. Chem. B, 2005. **109**(3): p. 1079-1087.

15. Underwood, S. and P. Mulvaney, *Effect of the solution refractive-index on the color of gold colloids.* Langmuir, 1994. **10**(10): p. 3427-3430.

16. Jensen, T.R., et al., *Nanosphere lithography: Effect of the external dielectric medium on the surface plasmon resonance spectrum of a periodic array of sliver nanoparticles.* Journal of Physical Chemistry B, 1999. **103**(45): p. 9846-9853.

17. Prodan, E., A. Lee, and P. Nordlander, *The effect of a dielectric core and embedding medium on the polarizability of metallic nanoshells.* Chemical Physics Letters, 2002. **360**(3-4): p. 325-332.

18. Lee, K.S. and M.A. El-Sayed, *Gold and silver nanoparticles in sensing and imaging: Sensitivity of plasmon response to size, shape, and metal composition.* Journal of Physical Chemistry B, 2006. **110**(39): p. 19220-19225.

19. Jain, P.K. and M.A. El-Sayed, *Noble metal nanoparticle pairs: Effect of medium for enhanced nanosensing.* Nano Letters, 2008. **8**(12): p. 4347-4352.

20. Sonnichsen, C., et al., *A molecular ruler based on plasmon coupling of single gold and silver nanoparticles.* Nature Biotechnology, 2005. **23**(6): p. 741-745.

21. Funston, A.M., et al., *Plasmon coupling of gold nanorods at short distances and in different geometries.* Nano Letters, 2009. **9**(4): p. 1651-1658.

22. Liu, N., et al., *Three-dimensional plasmon rulers.* Science, 2011. **332**(6036): p. 1407-1410.

23. Jain, P.K., W.Y. Huang, and M.A. El-Sayed, *On the universal scaling behavior of the distance decay of plasmon coupling in metal nanoparticle pairs: A plasmon ruler equation.* Nano Lett., 2007. **7**(7): p. 2080-2088.

24. Willingham, B., D.W. Brandl, and P. Nordlander, *Plasmon hybridization in nanorod dimers.* Appl. Phys. B-Lasers O, 2008. **93**(1): p. 209-216.

25. Prodan, E., et al., *A hybridization model for the plasmon response of complex nanostructures.* Science, 2003. **302**(5644): p. 419-422.

26. Jain, P.K., S. Eustis, and M.A. El-Sayed, *Plasmon coupling in nanorod assemblies: Optical absorption, discrete dipole approximation simulation, and exciton-coupling model.* J. Phys. Chem. B, 2006. **110**(37): p. 18243-18253.

27. Tabor, C., et al., *On the use of plasmonic nanoparticle pairs as a plasmon ruler: The dependence of the near-field dipole plasmon coupling on nanoparticle size and shape.* J. Phys. Chem. A, 2009. **113**(10): p. 1946-1953.

28. Naik, G.V., V.M. Shalaev, and A. Boltasseva, *Alternative plasmonic materials: Beyond gold and silver.* Adv. Mater., 2013. **25**(24): p. 3264-3294.

29. Liu, X. and M.T. Swihart, *Heavily-doped colloidal semiconductor and metal oxide nanocrystals: An emerging new class of plasmonic nanomaterials.* Chem. Soc. Rev., 2014. **43**(11): p. 3908-3920.

30. Zhong, Y.J., et al., *Review of mid-infrared plasmonic materials.* J. Nanophotonics, 2015. **9**(1): p. 093791.

31. Chou, L.W., et al., *Influence of dielectric anisotropy on the absorption properties of localized surface plasmon resonances embedded in si nanowires.* J. Phys. Chem. C, 2014. **118**(10): p. 5494-5500.

32. Chou, L.W., et al., *Tunable mid-infrared localized surface plasmon resonances in silicon nanowires.* J. Am. Chem. Soc. , 2012. **134**(39): p. 16155-16158.

33. Chou, L.W. and M.A. Filler, *Engineering multimodal localized surface plasmon resonances in silicon nanowires.* Angew. Chem. Int. Edit., 2013. **52**(31): p. 8079-8083.

34. Shin, N. and M.A. Filler, *Controlling silicon nanowire growth direction via surface chemistry.* Nano Lett., 2012. **12**(6): p. 2865-2870.

35. Chou, L.W., et al., *Tunable mid-infrared localized surface plasmon resonances in silicon nanowires.* J. Am. Chem. Soc., 2012. **134**: p. 16155-16158.

36. Chou, L.W., D.S. Boyuk, and M.A. Filler, *Optically abrupt localized surface plasmon resonances in si nanowires by mitigation of carrier density gradients.* Acs Nano, 2015. **9**(2): p. 1250-1256.

37. Palik, E.D. and G. Ghosh, *Handbook of optical constants of solids*. 1998, San Diego: Academic Press.

38. Hsu, S.W., C. Ngo, and A.R. Tao, *Tunable and directional plasmonic coupling within semiconductor nanodisk assemblies.* Nano Lett., 2014. **14**(5): p. 2372-2380.

39. Knight, M.W., et al., *Substrates matter: Influence of an adjacent dielectric on an individual plasmonic nanoparticle.* Nano Lett., 2009. **9**(5): p. 2188-2192.

40. Wu, Y.Y. and P.D. Yang, *Direct observation of vapor-liquid-solid nanowire growth.* J. Am. Chem. Soc., 2001. **123**(13): p. 3165-3166.

41. Harmand, J.C., et al., *Analysis of vapor-liquid-solid mechanism in au-assisted gaas nanowire growth.* Appl. Phys. Lett., 2005. **87**(20).

42. Jain, P.K. and M.A. El-Sayed, *Noble metal nanoparticle pairs: Effect of medium for enhanced nanosensing.* Nano Lett., 2008. **8**(12): p. 4347-4352.

43. Maier, S.A., et al., *Observation of near-field coupling in metal nanoparticle chains using far-field polarization spectroscopy.* Phys. Rev. B, 2002. **65**(19).

44. Maier, S.A., et al., *Local detection of electromagnetic energy transport below the diffraction limit in metal nanoparticle plasmon waveguides.* Nat. Mater., 2003. **2**: p. 229-232.

45. Bjork, M.T., et al., *One-dimensional heterostructures in semiconductor nanowhiskers.* Appl. Phys. Lett., 2002. **80**(6): p. 1058-1060.

46. Verheijen, M.A., et al., *Growth kinetics of heterostructured gap-gaas nanowires.* J. Am. Chem. Soc., 2006. **128**(4): p. 1353-1359.

47. Wen, C.Y., et al., *Formation of compositionally abrupt axial heterojunctions in silicon-germanium nanowires.* Science, 2009. **326**(5957): p. 1247-1250.

48. Panciera, F., et al., *Synthesis of nanostructures in nanowires using sequential catalyst reactions.* Nat. Mater., 2015. **14**: p. 820-825.

49. Christesen, J.D., et al., *Encoding abrupt and uniform dopant profiles in vapor-liquid-solid nanowires by suppressing the reservoir effect of the liquid catalyst.* Acs Nano, 2014. **8**(11): p. 11790-11798.

CHAPTER 4.

SURFACE PLASMON DRIVEN MID-INFRARED PHOTOCONDUCTIVITY IN ITO NANOCRYSTAL FILMS

4.1 Introduction

4.1.1 Mid-infrared optoelectronics overview and motivation

The infrared spectral region (2 μm > λ > 20 μm) is home to a range of optoelectronic technologies, including molecular spectroscopy,[1] imaging,[2, 3] and energy harvesting.[4] Narrow band-gap crystalline semiconductor materials, such as HgCdTe and InSb, currently underpin the field of infrared optoelectronics.[5] Devices based on these materials detect infrared photons via an inter-band quantum transition that is adjustable by alloy composition.[6] The key drawback of this approach is that a bulk single crystals with low defect densities is required for high performance devices. These criteria lead to high manufacturing costs as well as a form factor and fragility that limit their application space.[5] There remains a need for materials and manufacturing strategies that can enable cost-effective absorption and detection of infrared light.[7, 8] Self-assembled colloidal quantum dots in the mid-infrared

The infrared spectral region (2 μm > λ > 20 μm) is home to a range of optoelectronic technologies, including molecular spectroscopy,[1] imaging,[2, 3] and energy harvesting.[4] Narrow band-gap crystalline semiconductor materials, such as HgCdTe and InSb, currently underpin the field of infrared optoelectronics.[5] Devices based on these materials detect infrared photons via an inter-band quantum transition that is adjustable

by alloy composition.[6] The key drawback of this approach is that a bulk single crystals with low defect densities is required for high performance devices. These criteria lead to high manufacturing costs as well as a form factor and fragility that limit their application space.[5] There remains a need for materials and manufacturing strategies that can enable cost-effective absorption and detection of infrared light.[7, 8]

Thin films of semiconductor nanocrystals (NCs), also referred to as colloidal quantum dots (CQDs), have been widely investigated for their optical properties and applications in the infrared.[8] Research has been driven by the prospect of low-cost manufacturing of photoactive materials. NC films can be deposited from solution over large areas using spin-coating, spray-coating, and roll-to-roll techniques. Additionally, the optical properties of NCs are tailorable across the infrared by exploiting the size and surface dependence of their quantum inter- and intra-band transitions.[8-10] Infrared photodetection by NC thin films of PbS – a wide band-gap semiconductor – was first reported in 2005; however, the spectral range of these materials remains limited to < 2 μm.[11] HgTe – a zero band-gap semiconductor – is a leading NC material for mid-infrared optoelectronic applications with absorption tunable to 10 μm.[7, 12]

The surface physicochemistry of NCs strongly impacts their inter- and intra-band transitions. This connection, in principle, offers an opportunity for property engineering; however, it more often results in unwanted instabilities and reliability concerns. Foremost, surface changes over time, due to oxidation and/or electric current stress, degrade optoelectronic performance.[10] Second, the surface ligands can themselves absorb mid-infrared light, thus reducing the flux of photons to the active material. The coupling

of NC excited states with the ligand shell vibrations represent another loss pathway,[13] which stable inorganic matrices are needed to mitigate.[14] Finally, the organic ligands terminating a NC produce a dipole layer, small changes to which, particularly for small band-gap semiconductor materials, can cause large changes in the local electrostatic potential and thereby, the NC carrier density.[15-17]

4.1.2 Localized surface plasmons in the mid-infrared

As the free carrier density of CQDs is increased via doping, the intra-band resonances of the free electron density begin to behave as collective carrier density oscillations, physically and mathematically analogous to collective localized surface plasmon resonances (LSPR).[18, 19] The mid-infrared localized surface plasmon optical properties of doped semiconductor nanoparticles have been previously reported for a wide range of materials including group IV,[20] III-V,[21] transition metal oxides,[22] and copper chalcogenides.[23, 24] LSPR absorption has been widely touted as an alternative route for developing next generation low-cost mid-infrared optoelectronics.[7, 25]

4.1.3 Sn-doped indium oxide nanocrystals

Plasmonic NCs are emerging as a versatile platform for infrared optoelectronics due to their (i) straightforward synthesis, (ii) strong, stable, and tunable infrared absorption, and (iii) low toxicity and large earth-abundance relative to conventional materials.[7, 25, 26] As NC free carrier density increases via impurity doping, the intra-band resonances of the free electron density begin to behave as collective carrier density oscillations, physically and mathematically analogous to collective localized surface plasmon resonances (LSPR).[18, 19] The infrared optical properties of doped semiconductor

NC have been reported for a wide range of materials, including group IV,[20] III-V,[21] transition metal oxides,[22] and copper chalcogenides.[23, 24] NCs of Sn-doped In_2O_3, also known as indium tin oxide (ITO), are particularly promising due to their broadly adjustable LSPR via Sn doping as well as post-synthetic treatments and chemical stability under ambient conditions.[27, 28] Here, we demonstrate and characterize a mid-infrared LSPR driven photoconductive response in ITO NC films for the first time.

4.2 Experimental Methods

4.2.1 ITO nanocrystal colloidal synthesis

Plasmonic ITO nanocrystals are synthesized using a protocol well-studied in the literature. [27] 0.5 mmol In(acac)3 (Sigma-Aldrich, 99.99%), 0.043 mmol Sn(acac)2Cl2 (Sigma-Aldrich, 98%) were mixed with 7 g of oleylamine (Sigma-Aldrich, 70%) in a 50 mL two-necked flash then connected to a Schlenk-line. The reaction was carried out under nitrogen at 250 oC for 5 hours. The final dispersion of ITO nanocrystals was collected after 3 repeated cycles of precipitaion with ehanol centrifugation, and redisperisoin in hexane (BDH, ACS Grade). During redispersion, 20 μL oleylamine and 40 μL oleic acid (Sigma-Aldrich, 90%) are added for stabilization. As-synthesized ITO nanocrystals exhibit an average diameter of 9.4 ± 1.7 nm and a morphology consistent with the literature for this synthesis technique.[29] Detailed analysis of the NC physical properties as reported in a previous publication by our group.[30]

4.2.2 Electrical probe platform preparation via UV lithography

The Au probes are prepared using a standard UV lithography process[31] and a SEM image of the resulting sample measurement platform is shown in Figure 4.1. Intrinsic Si [111] 500μm thick FZ wafers obtained from University Wafer are selected as the substrates. Approximately 50 nm of SiO_2 is then deposited via Unaxis PECVD at 300°C. A MicroChem HDMS primer and 1813 Resist is spin coated onto the wafer via SCS G3P8 Spinner. A Karl Suss TSA MA6 Aligner is subsequently used to align the mask and expose the wafer with a 405 nm light source. Immediately following UV exposure, the wafer samples are soaked in a MicroChem MF-319 developer solution for 1 minute. A 2 nm Ti adhesion layer followed by a 50 nm Au layer is then deposited onto the patterned wafer using the Denton Explorer E-Beam Evaporation at a rate of 2 Å/s and chamber pressure of $< 1.0 \times 10^{-6}$ Torr. Following photoresist lift-off by soaking the wafer in ethanol, individual Au probe measurement platforms are obtained by dicing the wafer, rinsing the pieces in dimethylformamide, and finally, exposing them to UV-ozone in vacuum for 30 minutes to remove residual organics.

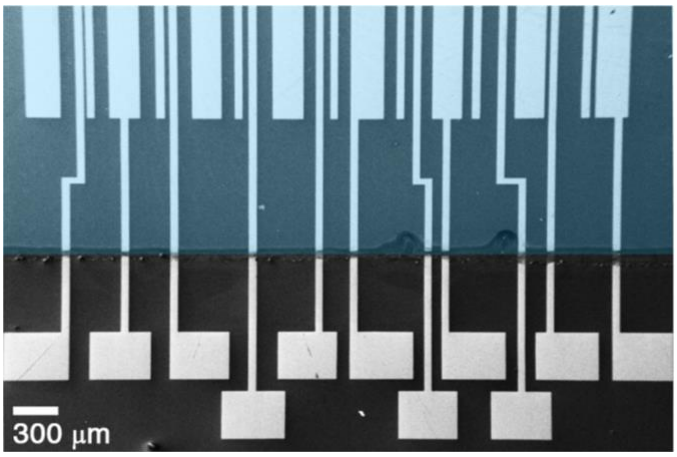

Figure 4.1 Scanning-electron-microscope image of ITO nanocrystal film electrical probe characterization platform. The area covered by the nanocrystal film is highlighted in blue.

4.2.3 Characterization of ITO nanocrystal film spectral response

We measure the far-field extinction spectra of as deposited NC film samples at room temperature immediately following the UV-ozone cleaning process using infrared spectroscopy (Bruker, Vertex 70).[20, 32, 33] Unpolarized light from a mid-infrared SiC globular source is combined with a KBr beam-splitter and a liquid nitrogen-cooled HgCdTe detector to collect transmission spectra between 700 and 3600 cm^{-1} for measurement of nanocrystals on SiO_2 substrates. In measurements of nanocrystals on Au substrate, unpolarized light from near-infrared SiC globar source is combined with a CaF_2 beam-splitter and a liquid nitrogen-cooled InSb detector to collect reflection spectra between 2000 and 8000 cm^{-1} in a diffuse reflectance accessory (Harrick Scientific Products, Praying Mantis). A transmission geometry cannot be conducted due to near-perfect reflectance of Au in the infrared. Also, since the ITO nanocrystals on Au exhibit a near-infrared All spectra are recorded using 48 scans and a resolution of 4 cm^{-1} and are baseline corrected using a standard concave rubberband method.

4.2.4 Nanocrystal film preparation

An approximately 20 nm thick ITO nanocrystal film is deposited onto the Au patterned substrate using a two-step spin coat recipe for NCs dispersed in hexane: (i) 30sec 1000 rotations per minute (RPM) and (ii) 20 sec at 4000 RPM. Masking tape was used to partially block the Au electrode contact pads when depositing the nanocrystals. Immediately afterwards, the masking tape is removed and the nanocrystal film sample is subjected to UV-ozone cleaning for 30 minutes. The morphology of the nanocrystal film

on the Au probe platform is then examined using a Zeiss Ultra 60 field-emission scanning electron microscope (SEM) and a sample image is shown in Figure 4.3.

4.2.5 Atomic layer deposition of Al_2O_3 and electrical characterization

Atomic layer deposition of Al_2O_3 is performed using a Cambridge NanoTech ALD tool. A thermal deposition process is performed at 200 °C utilizing water and trimethylaluminum (TMA) as the oxygen and aluminum precursors, respectively. A single ALD cycle consists of the following steps: (i) 1 s water pulse – (ii) 60 s purge – (iii) 1 s TMA pulse – (iv) 60 s purge. Electrical characterization is then performed using a Cascade Summit 9000 electrical probe station together with a Thor Labs SLS203L mounted stabilized globar infrared and ACE A20500 halogen visible light sources. Photocurrent density is calculated by dividing photocurrent measured by the nanocrystal film cross section = 6.6×10^{-7} cm^2. A Spectrogon LP-2000 long-pass filter is used in line with the infrared source to eliminate photons with wavelength < 2 μm from the broadband source output. IR source emission spectrum, with and without a long wave pass filter, is characterized using a Bruker Vertex 80v spectrometer with an MgCdTe detector. The illumination power is measured for both the infrared and visible sources in the experimental set up using Molectron MAX 5200 power meter per detector area of 11.5 cm^2. The light source manufacturer specified emission spectra are shown in Figure 4.2.

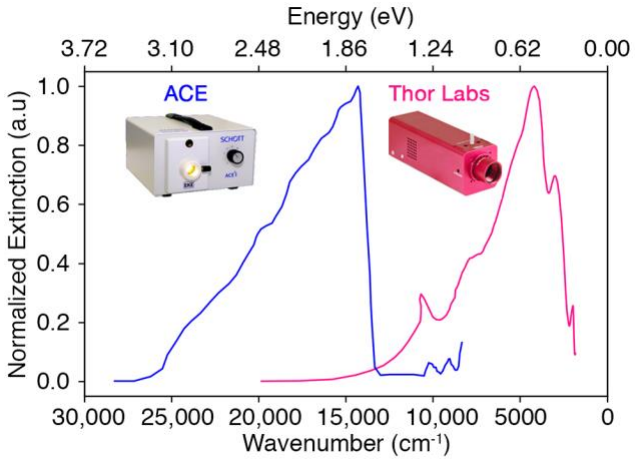

Figure 4.2. Normalized emission spectra for IR light source – Thor Labs (SLS203L) and visible light source – ACE (A20500).

4.3 Results and Discussion

4.3.1 Plasmonic ITO nanocrystal film infrared photoconductivity

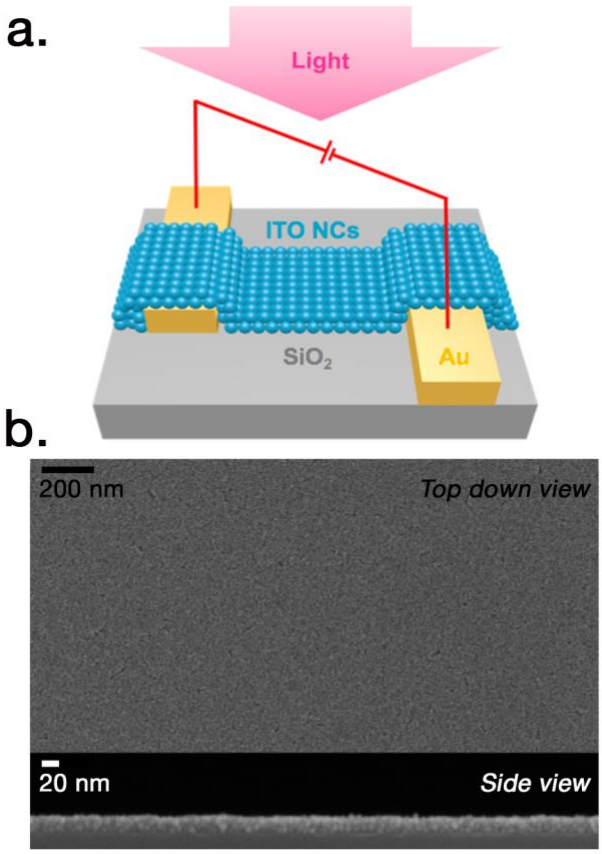

Figure 4.3 (a) ITO nanocrystal film photoconductor measurement schematic. (b) Top and side view SEM images of ITO nanocrystal film.

Al_2O_3 ALD coated ITO nanocrystal films produce photocurrent in response to a broadband infrared illumination (< 35 mW/cm^2) under electrical bias > |0.01| V. The measurement layout is shown in a schematic in Figure 4.3a. ITO nanocrystal films exhibit resistivities around 3.3 Ωcm. Visible light illumination showed no measurable photoresponse under analogous applied bias and illumination conditions. Figure 4.4a shows photocurrent density measured as a function of time at an applied bias of 10V. Infrared illumination at an interval of 10 seconds yields a consistent photocurrent density of ~ 1.8 A/cm^2 with a rise time constant (τ) of 0.6 seconds. τ was extracted via a negative

exponential fit of photocurrent density as a function of time. Intrinsic In_2O_3 nanocrystal films, which exhibit corresponding morphology but do not support LSPRs in the near-to-mid infrared regime, showed no photoconductive response under identical measurement conditions for visible and infrared light illumination and |0.01-100| V range of voltages bias magnitudes applied. In contrast, ITO nanocrystal films consistently yield photocurrent density proportion to voltage bias magnitude across the same range of magnitudes. In_2O_3 nanocrystal films exhibit a 5 orders of magnitude higher resistivity their Sn doped counterparts; this difference in electron collection precludes a conclusive comparison. Nonetheless, the exclusive relationship between infrared LSPR-driven absorption in ITO nanocrystals and infrared photoconductivity of ITO nanocrystal films suggests an LSPR-driven infrared photoconduction mechanism.

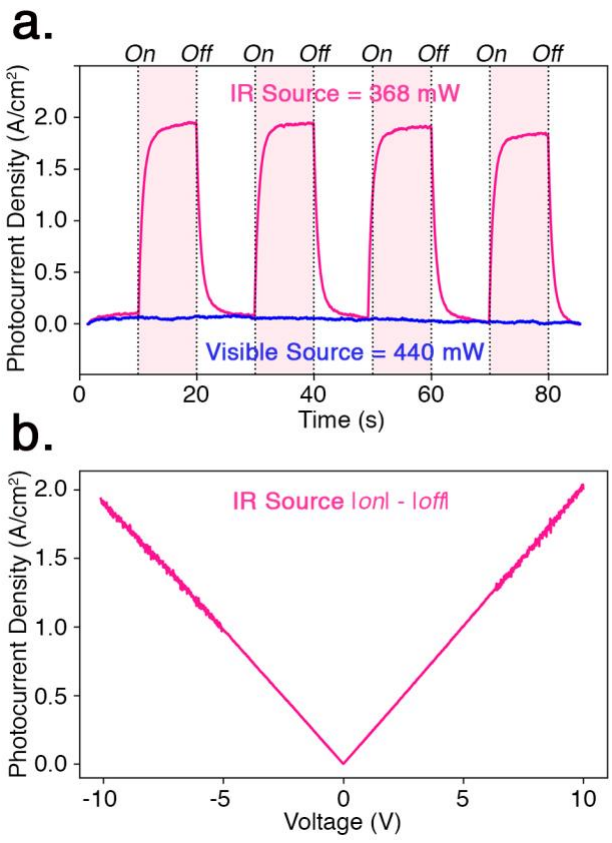

Figure 4.4. ITO nanocrystal film photoresponse (a) Photocurrent density measured as a function of time at a voltage bias of 10V for broadband infrared and visible light illumination. (b) Photocurrent density measured as a function of voltage bias between -10V and 10V for infrared illumination. The infrared (IR) and visible light sources emission spectra, as specified by the respective manufacturer, are shown in Figure 4.2.

4.3.2 Photoconduction based photodetector metrics

The ITO nanocrystal films exhibit a linear photocurrent voltage dependence, as shown in Figure 4.4b. This behavior is consistent with visible light photoconductor device performance.[34] Our data establish a connection between infrared light illumination and NC thin films supporting infrared LSPRs. We calculate a responsivity (R) of 12.3 A/W for broadband infrared light illumination using Equation (1), where $J_{electron}$ is the measured photocurrent density and J_{photon} is the broadband infrared illumination power supplied.

$$R(infrared) = \frac{J_{electron}}{J_{photon}(infrared)} \tag{1}$$

In this calculation, we assume the optically active nanocrystal device area to be the total surface area of the two Au electrodes and the SiO_2 substrate in-between (4.2×10^{-3} cm^2). Furthermore, we calculate a noise equivalent power (NEP) of 1.8×10^{-10} $WHz^{-1/2}$ and a detectivity (D^*) of 1.2×10^{8} $cmHz^{1/2}W^{-1}$ for a broadband 2000 – 10,000 cm^{-1} infrared

$$NEP(infrared) = \frac{\sqrt{\overline{I_n^2}}}{R(infrared)} \tag{2}$$

$$D^*(infrared) = \frac{\sqrt{Area}}{NEP(infrared)} \tag{3}$$

illumination using the equations (2) and (3) as follows. where Area is the optically active

NC film area and I_n is the noise current – defined as the root mean square of fluctuations in current over a bandwidth of 1 Hz.[9, 34]

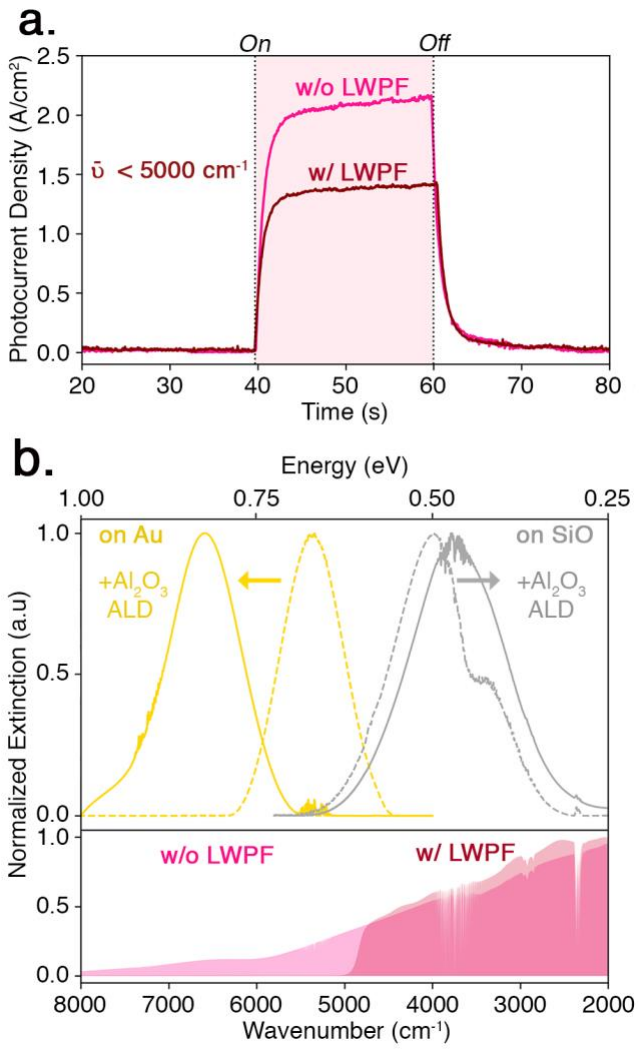

Figure 4.5. (a) Photocurrent density for broadband infrared source illumination with and without a LWPF is shown as a function of time. The "light on" period is highlighted in pink. (b) Normalized extinction of ITO nanocrystal films on SiO_2 and Au substrates is shown following UV-ozone treatment (solid curve) and 30 cycles of Atomic Layer Deposition (ALD) of Al_2O_3 at 200 °C (dash curve). The measured infrared source emission spectrum without a long wave pass filter (w/o LWPF) is indicated by pink infill, while the measured emission with a LWPF ($\upsilon_{cut\text{-}off}$ = 5000 cm^{-1}) is shown as red infill.

4.3.3 Photoconductivity stems from ITO nanocrystals on Au and SiO_2

Figure 4.5a shows that photocurrent density is reduced by 0.6 A/cm^2 or ~30 % when inserting a long wave pass filter (LWPF) which cuts off all light with energy > 5000 cm^{-1} in the illumination pathway while the illumination power flux is also reduced from 32.0 to 19.7 mW/cm^2. The corresponding infrared source emission spectra, with and without the LWPF, are shown by an infill plot in Figure 4.5b. Additionally, the ITO nanocrystal film absorbance spectra on Au and SiO_2 substrates before and after Al_2O_3 ALD are also shown on the same energy axis in Figure 4.3b. The ITO nanocrystal film exhibits a broad near-infrared (5322 cm^{-1}) and a mid-infrared (4052 cm^{-1}) LSPR absorption peaks on Au and SiO_2 substrates, accordingly. Interestingly, a 1095 cm^{-1} increase (blue-shift) in the LSPR peak energy is observed following ALD for nanocrystals on the Au substrate. However, a 259 cm^{-1} decrease (red-shift) is observed for NCs on SiO_2.

4.3.4 Al_2O_3 ALD and substrate effects on LSPR

The changes in the nanocrystal LSPR energy with v of Al_2O_3 are driven by a combination of effects simultaneously taking place during the conformal Al_2O_3 deposition. At the ALD temperature of 200 ^oC and a chamber pressure of ~ 1.0×10^{-2} Torr, the ITO nanocrystal surfaces are stripped of ambient adsorbents (i.e. water molecules) and are conformally passivated by Al_2O_3. Al_2O_3 infills the void between the closely packed nanocrystals with continued deposition[35] and changes in the NC dielectric environment across the LSPRs of the neighboring nanocrystals in the film interact.[36] On

an insulating SiO_2 substrate, the optical properties of the ITO nanocrystal film stem from the aggregate sum of inter-nanocrystal coupled optical response across the film. Here, increasing the dielectric environment with Al_2O_3 infill results in net constructive change in dipolar LSPR coupling, and thereby red-shifts the NC film LSPR energy.[36, 37]

A number of factors impact the optical response of the ITO NC thin films (Figure 1b), which are important for understanding our photoresponse measurements. Foremost, absorption depends on the identity to the underlying substrate. In the present case, the ITO NCs couple to the image dipole of the Au film[38], and therefore blue shifting their oscillation frequency relative to substrates without a large free carrier density (i.e., SiO_2). The spectral response for ITO NCs on Au is consistent with the literature. Al_2O_3 deposition via ALD leads to other effects. As is seen for ITO NCs on SiO_2 due to the reduction of the shoulder near 3400 cm^{-1}, ALD removes adsorbed water. The same feature is not observed for ITO NCs on Au as it is outside of the measurement range. Similar to recent work, we expect that Al_2O_3 infills the void between the closely packed NCs with continued deposition[35] and changes in the NC dielectric environment across the LSPRs of the neighboring NCs in the film interact.[36] On an insulating SiO_2 substrate, the optical properties of the ITO NC film stem from the aggregate sum of inter-NC coupled optical response across the film. Here, increasing the overall film dielectric environment with Al_2O_3 ALD infill results in net constructive change in dipolar LSPR coupling, and thereby red-shifts the NC film LSPR energy.[36, 37] Previous publications from our group discuss in detail the effects a dielectric environment exhibits on nanoparticle LSPR coupling interactions in the mid-infrared.[32, 37-42] In this study we focus on demonstrating

and characterizing the infrared photoconduction of ITO nanocrystal films following Al_2O_3 ALD.

The ~30% reduction in photocurrent density observed upon eliminating the photons with energy > 5000 cm^{-1} with a LWPF suggests that a corresponding amount of photocurrent density is derived from light with energies in that spectral region. The incident infrared source extinction, with and without a LWPF, is displayed in the lower half of Figure 5b. The ITO nanocrystal film spectral response also plotted in Figure 5b suggests that the infrared source emission eliminated by the LWPF corresponds to the LSPR spectral range of ITO nanocrystals on the Au substrate. Therefore, the photocurrent density measured with a LWPF is likely attributed to the photoconductive response of ITO nanocrystals on the SiO_2 substrate. In summary, the reduction in the photocurrent density due to a LWPF, as shown in Figure 4.5, suggests that ITO nanocrystals on both the Au and SiO_2 substrates contribute to photoconductivity measured.

4.3.5 Photoconductivity mechanism hypotheses

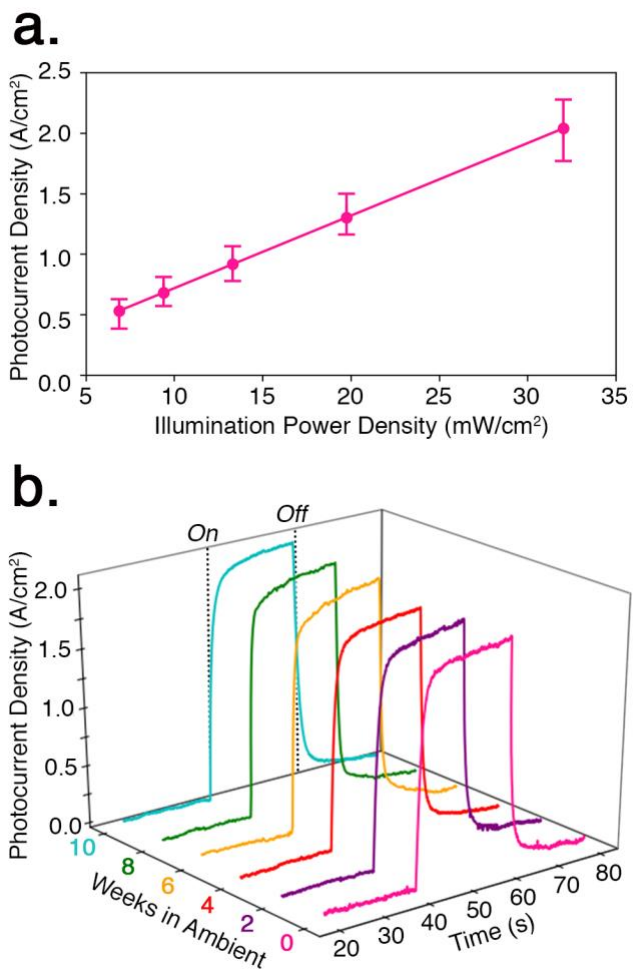

Figure 4.6. (a) Photocurrent density shown as a function of broadband infrared source illumination powers. A set of 6 sample measurements series was used to derive photocurrent confidence intervals. (b) ITO nanocrystals film broadband infrared (w/o LWPF, 32 mW/cm^2) photoresponse measured over 10 weeks in ambient conditions. A 20 second illumination period was used for measurement shown in Figure 4.3b.

We also probe the ITO nanocrystal film photoconductivity as a function of infrared source illumination power flux between 5 – 35 mW/cm^2 as shown Figure 4.5a. The observed voltage, illumination, and spectral dependences provide initial insight into the mechanism of photoconduction. The linear scaling of photocurrent density with illumination intensity (Figure 4a), especially if true for illumination intensities beyond 35

mW/cm^2, indicates that the underlying photoconductivity mechanism is athermal. Heat-driven carrier density or inter-NC contact effects would be expected to follow an Arrhenius (i.e., exponential) dependence.[43] Also, temperature driven carrier-density change are likely negligible in heavily-doped ITO.[44] LSPR driven NC surface heating effects on inter-NC contacts within the film cannot be ruled out in this work due to limited illumination power range. Photocurrent measurements with and without the LWPF show that ITO NCs on the Au and SiO_2 are both contributing to the photoresponse. Further studies of the photocurrent generation mechanism in the ITO NC films are underway in our laboratory.

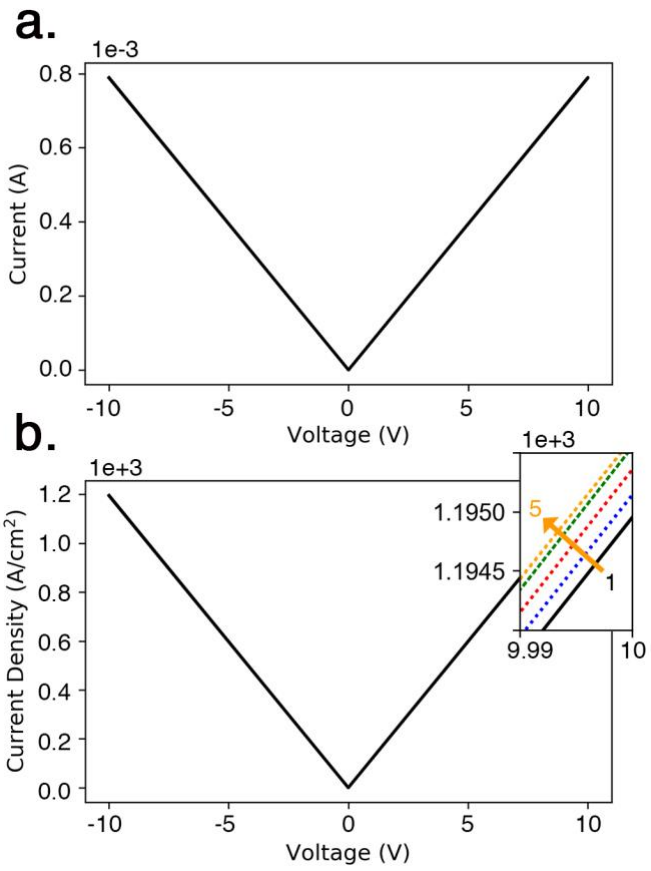

Figure 4.7. (a) 5 consecutive measurements of ITO nanocrystal film dark current and (b) current density as a function of voltage bias between -10V and 10V. Current density is obtained by dividing current by the ITO nanocrystal film cross-section. The inset shows an approximately 0.5 A/cm^2 change and saturation of current density magnitude within 5 consecutive voltage scans.

4.3.6 ITO nanocrystal film stability and electrical reliability

Lastly, we investigate ITO nanocrystal device stability over time and under electrical stress. Figure 4.4b shows photocurrent density measured for a single ITO nanocrystal film photoconductor device sample over the course of 10 weeks at a voltage bias of 10V. The ITO nanocrystal film exhibits excellent stability with a sample standard deviation of 0.09 A/cm^2 obtained for a set of 6 measurement with two week intervals. The stability of the ITO NCs in ambient conditions and the reproducibility of the

photoconductivity measurements under prolonged current stress at large voltage biases is a key advantage of our ITO NC thin film. In contrast to PbS and HgTe NCs,[29, 45] transition metal oxide NCs are not under threat of oxidation. Electrical stability is enabled by the complete removal of organic ligands via UV-ozone cleaning and then subsequent NC surface passivation via Al_2O_3. This process yields a closely packed NC thin film with metallic inter-NC contacts in 3 dimensions and electrically insulated NC surfaces. Furthermore, substitutional Sn^{4+} dopants in ITO NCs can produce degenerate carrier densities as large as 10^{21} cm^{-3} [46], resulting in low resistivity within a NC film and thereby enabling electrical reliability, as shown for 5 consecutive of voltage scans in Figure 4.7.

4.4 Summary and Outlook

Infrared photoconductive plasmonic ITO nanocrystal films are a promising materials platform for emerging infrared optoelectronic technologies. We demonstrate plasmonically-driven infrared photoconduction in ITO NC films coated with Al_2O_3. A responsivity of 15 A/W and a detectivity of 1.2×10^8 $cmHz^{1/2}W^{-1}$ is found using a broadband infrared lamp illumination. ITO NCs on both Au electrodes and the SiO_2 substrate contribute to the infrared photocurrent. Devices exhibit reliable photoconductive performance over multiple months of measurements in ambient at a voltage bias of 10 V. Our results indicate that infrared LSPR supported by ITO NC films are a viable materials platform for next-generation infrared optoelectronic technologies.

4.5 References

1. Mcdonald, R.S., *Infrared spectrometry - review.* Analytical Chemistry, 1986. **58**(9): p. 1906-1925.
2. Turker-Kaya, S. and C.W. Huck, *A review of mid-infrared and near-infrared imaging: Principles, concepts and applications in plant tissue analysis.* Molecules, 2017. **22**(1).
3. Razeghi, M. and B.M. Nguyen, *Advances in mid-infrared detection and imaging: A key issues review.* Reports on Progress in Physics, 2014. **77**(8).
4. Byrnes, S.J., R. Blanchard, and F. Capasso, *Harvesting renewable energy from earth's mid-infrared emissions.* Proceedings of the National Academy of Sciences of the United States of America, 2014. **111**(11): p. 3927-3932.
5. Henini, M. and M. Razeghi, *Handbook of infrared detection technologies*. 2002, New York: Elsevier Advanced Technology. xiv, 518 p.
6. Krier, A., *Mid-infrared semiconductor optoelectronics*. Springer series in optical sciences. 2006, London: Springer. xviii, 751 p.
7. Lhuillier, E. and P. Guyot-Sionnest, *Recent progresses in mid infared nanocrystal optoelectronics.* IEEE, 2017. **23**(5).
8. Konstantatos, G. and E.H. Sargent, *Nanostructured materials for photon detection.* Nature Nanotechnology, 2010. **5**(6): p. 391-400.
9. Saran, R. and R.J. Curry, *Lead sulphide nanocrystal photodetector technologies.* Nature Photonics, 2016. **10**(2): p. 81-92.
10. García de Arquer, F.P., et al., *Solution-processed semiconductors for next-generation photodetectors.* Nature Reviews Materials, 2017. **2**(3).

11. McDonald, S.A., et al., *Solution-processed pbs quantum dot infrared photodetectors and photovoltaics.* Nature Materials, 2005. **4**(2): p. 138-142.

12. Keuleyan, S., et al., *Mid-infrared hgte colloidal quantum dot photodetectors.* Nature Photonics, 2011. **5**(8): p. 489-493.

13. Liu, H. and P. Guyot-Sionnest, *Photoluminescence lifetime of lead selenide colloidal quantum dots.* Journal of Physical Chemistry C, 2010. **114**(35): p. 14860-14863.

14. Kovalenko, M.V., et al., *Inorganically functionalized pbs-cds colloidal nanocrystals: Integration into amorphous chalcogenide glass and luminescent properties.* J Am Chem Soc, 2012. **134**(5): p. 2457-60.

15. Chuang, C.H.M., et al., *Improved performance and stability in quantum dot solar cells through band alignment engineering.* Nature Materials, 2014. **13**(8): p. 796-801.

16. Jeong, K.S., et al., *Air-stable n-doped colloidal hgs quantum dots.* Journal of Physical Chemistry Letters, 2014. **5**(7): p. 1139-1143.

17. Carroll, G.M., et al., *Spectroelectrochemical measurement of surface electrostatic contributions to colloidal cdse nanocrystal redox potentials.* Chemistry of Materials, 2016. **28**(21): p. 7912-7918.

18. Schimpf, A.M., et al., *Charge-tunable quantum plasmons in colloidal semiconductor nanocrystals.* Acs Nano, 2014. **8**(1): p. 1065-1072.

19. Shen, G.H. and P. Guyot-Sionnest, *Hgs and hgs/cds colloidal quantum dots with infrared intraband transitions and emergence of a surface plasmon.* Journal of Physical Chemistry C, 2016. **120**(21): p. 11744-11753.

20. Chou, L.W., et al., *Tunable mid-infrared localized surface plasmon resonances in silicon nanowires.* J Am Chem Soc, 2012. **134**(39): p. 16155-8.

21. Zhong, Y.J., et al., *Review of mid-infrared plasmonic materials.* Journal of Nanophotonics, 2015. **9**.

22. Lounis, S.D., et al., *Defect chemistry and plasmon physics of colloidal metal oxide nanocrystals.* Journal of Physical Chemistry Letters, 2014. **5**(9): p. 1564-74.

23. Liu, X. and M.T. Swihart, *Heavily-doped colloidal semiconductor and metal oxide nanocrystals: An emerging new class of plasmonic nanomaterials.* Chemical Society Reviews, 2014. **43**(11): p. 3908-3920.

24. Wang, C.J., M. Shim, and P. Guyot-Sionnest, *Electrochromic nanocrystal quantum dots.* Science, 2001. **291**(5512): p. 2390-2392.

25. Tan, C.L. and H. Mohseni, *Emerging technologies for high performance infrared detectors.* Nanophotonics, 2018. **7**(1): p. 169-197.

26. Diroll, B.T., et al., *Synthesis of n-type plasmonic oxide nanocrystals and the optical and electrical characterization of their transparent conducting films.* Chemistry of Materials, 2014. **26**(15): p. 4579-4588.

27. Gilstrap, R.A., et al., *Synthesis of a nonagglomerated indium tin oxide nanoparticle dispersion.* Adv Mater, 2008. **20**(21): p. 4163-+.

28. Kanehara, M., et al., *Indium tin oxide nanoparticles with compositionally tunable surface plasmon resonance frequencies in the near-ir region.* Journal of the American Chemical Society, 2009. **131**(49): p. 17736-17737.

29. Garcia, G., et al., *Dynamically modulating the surface plasmon resonance of doped semiconductor nanocrystals.* Nano Letters, 2011. **11**(10): p. 4415-4420.

30. Hu, W., et al., *Reversible tuning of the surface plasmon resonance of indium tin oxide nanocrystals by gas-phase oxidation and reduction.* The Journal of Physical Chemistry C, 2017. **121**(29): p. 15970-15976.

31. Rabih Zaouk, B.Y.P., and Marc J. Madou, *Introduction to microfabrication techniques*, in *Microfluidic techniques reviews and protocols*, M. S.D., Editor. 2006, Humana Press. p. 248.

32. Boyuk, D.S., L.W. Chou, and M.A. Filler, *Strong near-field coupling of plasmonic resonators embedded in si nanowires.* Acs Photonics, 2016. **3**(2): p. 184-189.

33. Chou, L.W., D.S. Boyuk, and M.A. Filler, *Optically abrupt localized surface plasmon resonances in si nanowires by mitigation of carrier density gradients.* Acs Nano, 2015. **9**(2): p. 1250-1256.

34. Konstantatos, G. and E.H. Sargent, *Nanostructured materials for photon detection (vol 5, pg 391, 2010).* Nature Nanotechnology, 2010. **5**(12).

35. Ephraim, J., et al., *Transparent conductive oxide nanocrystals coated with insulators by atomic layer deposition.* Chemistry of Materials, 2016. **28**(15): p. 5549-5553.

36. Jain, P.K. and M.A. El-Sayed, *Noble metal nanoparticle pairs: Effect of medium for enhanced nanosensing.* Nano Letters, 2008. **8**(12): p. 4347-4352.

37. Chou, L.W., et al., *Influence of dielectric anisotropy on the absorption properties of localized surface plasmon resonances embedded in si nanowires.* J. Phys. Chem. C, 2014. **118**(10): p. 5494-5500.

38. Knight, M.W., et al., *Substrates matter: Influence of an adjacent dielectric on an individual plasmonic nanoparticle.* Nano Letters, 2009. **9**(5): p. 2188-2192.

39. Underwood, S. and P. Mulvaney, *Effect of the solution refractive-index on the color of gold colloids.* Langmuir, 1994. **10**(10): p. 3427-3430.

40. Jain, P.K., W.Y. Huang, and M.A. El-Sayed, *On the universal scaling behavior of the distance decay of plasmon coupling in metal nanoparticle pairs: A plasmon ruler equation.* Nano Lett., 2007. **7**(7): p. 2080-2088.

41. Tan, S.J., et al., *Plasmonic coupling at a metal/semiconductor interface.* Nature Photonics, 2017. **11**(12): p. 806-+.

42. Jain, P.K. and M.A. El-Sayed, *Noble metal nanoparticle pairs: Effect of medium for enhanced nanosensing.* Nano Lett., 2008. **8**(12): p. 4347-4352.

43. Gross, M., A. Winnacker, and P.J. Wellmann, *Electrical, optical and morphological properties of nanoparticle indium-tin-oxide layers.* Thin Solid Films, 2007. **515**(24): p. 8567-8572.

44. Ederth, J., et al., *Indium tin oxide films made from nanoparticles: Models for the optical and electrical properties.* Thin Solid Films, 2003. **445**(2): p. 199-206.

45. Silberman, J.A., et al., *Comparative-study of activated oxygen-uptake on hgte, hg0.69cd0.31te, and cdte.* Journal of Vacuum Science & Technology a-Vacuum Surfaces and Films, 1985. **3**(1): p. 222-225.

46. Lounis, S.D., et al., *Influence of dopant distribution on the plasmonic properties of indium tin oxide nanocrystals.* Journal of the American Chemical Society, 2014. **136**(19): p. 7110-7116.

CHAPTER 5.

CONCLUDING REMARKS

5.1 Conclusions

The capacity to chemically engineer a plasmonic response of a given material via a well-established toolbox of doping techniques is unique proposition of semiconductor nanomaterials. The active dopant incorporation capacity, there by carrier density, of a semiconductor crystal establishes the upper limit on LSPR spectral range in the near-infrared. However, due to the lower free carrier densities found in doped semiconductors, correspondingly reduced permittivity values in comparison to metals, and these materials are uniquely well-suited for subwavelength LSPR field confinement at the long infrared excitation wavelengths.

Doped semiconductors have emerged as an advantageous alternative plasmonic materials platform for harnessing LSPRs for optoelectronic technology applications, specifically in the infrared spectral region. A myriad of semiconductor nanomaterials with diverse physical properties have been shown to sustain LSPRs upon sufficient injection of carrier density via aliovalent and vacancy chemical doping methods, as well via electrochemical and photochemical charging in solution as discussed in Chapter 1. The experimental studies and theoretical analysis performed as part of this dissertation has contributed to establishing doped semiconductors as advantageous and viable alternative nanomaterials platform for next-generation LSPR based technologies.

Spatial control of dopant, and thereby carrier density, is critical for harnessing the LSPR coupling interactions in nanoscale semiconductors. In Chapter 2, we study Si nanowires containing multiple plasmonic resonators and demonstrate the impact of axial carrier density gradients on the interactions of resonators embedded in a Si nanowire. A modulated temperature nanowire growth process was then developed to mitigate the "residual doping" and resulting carrier density gradients during the VLS growth process. Series of doped segments fabricated along the length of a nanowire via the modulated temperature growth process, exhibited a coupled LSPR spectral response indistinguishable from that of nanowires with ideal, atomically abrupt carrier density profiles. These experiments have important implications for the control of near-field plasmonic phenomena and plasmonic energy transport in semiconductor nanowires. Our methods provide a road map for fabricating chains of highly doped and abrupt plasmonic resonators along the length of a Si nanowire.

In additional to well-studied LSPR tuning levers such as electron carrier density, environment permittivity and geometry, in Chapter 3 we show dielectric environment anisotropy to be an additional powerful tool for optimizing LSPR spectral response and neat-field intensity in particle arrays. We demonstrated that embedding resonators along the length of a nanowire can dramatically increase the LSPR coupling interaction strength and thereby, plasmonic spectral extinction and near-field intensity, due to the dielectric environment anisotropy within a nanowire. The near-field interaction length was shown to be 4-5 times larger than the value obtained for the same resonators in isotropic vacuum or isotropic Si surroundings. More generally, our results suggest that LSPR interaction strength within an array of particles can be dramatically increased by designing high

dielectric material based inter-connections or “bridge” for near-field interactions between adjacent LSPRs.

Bottom up grown semiconductor nanowires, with doped segments along the length of the nanowire, inherently benefit from the dielectric anisotropy within of the nanowire geometry. In Chapter 3 we show that this system is uniquely suitable for engineering and exploiting long distance LSPR coupling interactions in the infrared. Our DDA simulations of plasmonic resonators embedded in Ge and GaAs nanowires in this chapter, generally suggest that coupling within an array of plasmonic resonators (in a specific spectral regime) can be optimized via a combination of (1) interconnecting dielectric material permittivity and (2) interconnection geometry parameters.

In Chapter 4, we apply the understanding of LSPR behavior gained in studying doped Si nanowires to harness the infrared LSPR driven photoconduction of Sn doped In_2O_3 nanocrystal films. Here, we first demonstrate the LSPR driven infrared photoconductivity within self-assembled plasmonic ITO nanocrystal films coated with Al_2O_3. Our measurements with a broadband infrared illumination source indicate a photoconductor responsivity of 15 A/W and a detectivity of 1.2×10^8 $cmHz^{1/2}W^{-1}$. Additionally, we show that these films exhibit reliable photoconductive performance over months in ambient and under electrical stress.

We first demonstrate infrared photoconductivity within the Al_2O_3 coated ITO nanocrystal films, and show that infrared photocurrent in these materials exhibits an exclusive relationship with LSPR absorption in the same regime. However, the exact mechanism of photocurrent generation following LSPR absorption remains unknown. As

a first step towards solving puzzle, we characterized photocurrent density as a function of illumination power in the range of 5 – 35 mW/cm^2, and showed a linear relationship. The absence of an Arrhenius dependence on illumination suggests a non-temperature change driven photocurrent generation mechanism under voltage bias. Here, it is important to note that our broadband illumination intensity range is relatively narrow and perhaps insufficient to characterize the underlying non-linear relationship between illumination and photocurrent in the ITO nanocrystal films. Furthermore, our measurements were limited by the broadband nature of the IR source used. In future studies, combining analyses (1) photocurrent as a function of illumination energy and intensity across the infrared with (2) dark current measurements of the nanocrystal films as a function of temperature can yield insight into whether the LSPR heating of the nanocrystals or inter-nanocrystal contacts is driving the infrared photoconductivity measured. In summary, we first demonstrated that low energy near-to-mid infrared LSPR absorption can yield photocurrent in self assembled nanocrystal films. Our results suggest infrared plasmonics based on doped semiconductor nanomaterials as a promising alternative strategy for developing next generation infrared optoelectronic materials and technology.

5.2 Outlook

Phosphorus doped Si nanowires and Sn doped In_2O_3 nanocrystals are highly advantageous plasmonic nanomaterials in the infrared. In this dissertation, we outline how their plasmonic spectral response can be designed (1) bottom-up during using chemical doping and can further be dynamically modulated post synthesis via surface

reactions, photoexcitation and applied bias as discussed in Chapter 1. By the same token, the utility of the doped semiconductor surface plasmons is ultimately limited by the nature of dopant impurities and their interactions with the semiconducting crystal to create and balance free carrier densities in the conduction and valance bands. Although we have made great progress in understanding the synthesis and corresponding plasmonic properties of these materials, the application of doped Si nanowires and ITO nanocrystals in industry-scale optoelectronic devices hinges on several unanswered inquiries under investigation in our group as well as in the broader scientific community.[1-5]

Foremost, the active and inactive dopant content and spatial distribution are key questions unanswered questions for both Si nanowire and ITO nanocrystal materials synthesized in the studies comprising this dissertation, and in the broader field of plasmonic semiconductor nanomaterials research. The direct mapping of active dopant atom distributions, and thereby free-carrier distributions, in semiconductor nanowires and nanocrystals remains challenging due to limited spatial resolution of light and electron microscopic techniques. The difficulty of such measurements is compounded by the fact that (1) overall dopant content and particularly, active dopant content levels, in these materials can be extremely low. And furthermore, (2) the dopant atoms generally exhibit relatively similar size and valence to the host lattice. In the DDA simulations of doped Si nanowires presented in the Chapters 2 and 3, we assumed uniform radial distributions of carriers in doped Si resonators as a simplifying approximation. Similarly, the exact radial distribution of dopants in plasmonic ITO nanocrystals characterized in Chapter 4 remains unknown. However, the general radial dependencies of dopant content distributions and activation in these type of materials is well-documented in the literature. [6-9] A direct

detailed measurement of active dopant distributions in Si nanowires and ITO nanocrystals would enable further optimization of their plasmonic near-field as well far field optical properties.

Furthermore, the relationship between the LSPR spectral response and the nanomaterial crystal facets, surface energies, reconstructions and terminations by molecules during and immediately synthesis largely remains a key unanswered question for (1) doped Si nanowires[10] and (2) ITO nanocrystals[2] :

(1) First, in the VLS synthesis of Si nanowires outlined in Chapters 2 and 3, the use of a eutectic Au catalyst droplet results in a distribution of residual Au atomic clusters on the nanowire sidewalls. Furthermore, the reaction of the Si precursor (Si_2H_6) and the phosphorus dopant precursor (PCl_3), at the catalyst droplet and the nanowire surface, delivers Si, H, P and Cl based molecules to the Si nanowire surface facets. Together with Au, these elements determine the exact Si nanowires surface properties which interact with the doped Si nanowire LSPRs.[11] Fortunately, the effect of Si nanowire sidewall surfaces is strongly minimized for LSPRs embedded along the lengths of a Si due to the dominance the axial-direction LSPR oscillation mode and concentration of the LSPR field within the Si nanowire enabled by the Si dielectric anisotropy as discussed in Chapter 3.

(2) The interactions between the ITO nanocrystal LSPRs and the nanocrystal surface facets and ligands are not well understood particularly in the infrared spectral regime.[12-14] Specifically, the photoconductivity experiments outlined in Chapter 4, utilize ITO nanocrystal films whose surfaces are first cleaned via a UV-ozone treatment and then

passivated by Al_2O_3 ALD at 200 ^oC in vacuum. While the ALD treatment was shown to produce a marginal change in the LSPR response in the infrared, this surface passivation step was found to be critical in permitting the measurement of ITO nanocrystal films photoconductive response. In further studies, investigating the impact of individual ALD precursors ($Al(CH_3)_3$ and H_2O) and of the resulting Al_2O_3 film on ITO nanocrystal surfaces at 200^oC is bound to yield insight into the relationship between the infrared LSPR absorption and photoconductivity in these materials.

Finally, it is important to note that substantial innovation in the synthesis methods are needed to be able to produce an industrially relevant quantity of ITO nanocrystals or doped Si nanowires while retaining control of nanomaterial crystal quality and nanoparticle uniformity as noted for syntheses outlined in this dissertation. Additionally, practical concerns such as cost of raw materials and equipment, toxicity to the environment, and long term chemical stability need to be addressed prior to industrial application. We need further fundamental research, as the investigations outlined in this dissertation, to build up the understanding necessary for industrial scaling and further technology development based on infrared plasmonic Si nanowire and ITO nanocrystal material platforms.

5.3 References

1. Ek, M. and M.A. Filler, *Atomic-scale choreography of vapor-liquid-solid nanowire growth.* Accounts of Chemical Research, 2018. **51**(1): p. 118-126.

2. Agrawal, A., et al., *Localized surface plasmon resonance in semiconductor nanocrystals.* Chemical Reviews, 2018. **118**(6): p. 3121-3207.

3. Zhang, H., et al., *Doped silicon nanocrystal plasmonics.* Acs Photonics, 2017. **4**(4): p. 963-970.

4. Joyce, H.J., et al., *A review of the electrical properties of semiconductor nanowires: Insights gained from terahertz conductivity spectroscopy.* Semiconductor Science and Technology, 2016. **31**(10).

5. Coughlan, C., et al., *Compound copper chalcogenide nanocrystals.* Chemical Reviews, 2017. **117**(9): p. 5865-6109.

6. Perea, D.E., et al., *Direct measurement of dopant distribution in an individual vapour-liquid-solid nanowire.* Nature Nanotechnology, 2009. **4**(5): p. 315-319.

7. Prosa, T.J., et al., *Characterization of dilute species within cvd-grown silicon nanowires doped using trimethylboron: Protected lift-out specimen preparation for atom probe tomography.* Journal of Microscopy, 2010. **239**(2): p. 92-98.

8. Lounis, S.D., et al., *Influence of dopant distribution on the plasmonic properties of indium tin oxide nanocrystals.* Journal of the American Chemical Society, 2014. **136**(19): p. 7110-7116.

9. Crockett, B.M., et al., *Radial dopant placement for tuning plasmonic properties in metal oxide nanocrystals.* Acs Nano, 2017. **11**(8): p. 7719-7728.

10. Chou, L.W., et al., *Influence of dielectric anisotropy on the absorption properties of localized surface plasmon resonances embedded in si nanowires.* Journal of Physical Chemistry C, 2014. **118**(10): p. 5494-5500.

11. Boyuk, D.S., L.W. Chou, and M.A. Filler, *Strong near-field coupling of plasmonic resonators embedded in si nanowires.* Acs Photonics, 2016. **3**(2): p. 184-189.

12. Hu, W., et al., *Reversible tuning of the surface plasmon resonance of indium tin oxide nanocrystals by gas-phase oxidation and reduction.* The Journal of Physical Chemistry C, 2017. **121**(29): p. 15970-15976.

13. Agrawal, A., et al., *Resonant coupling between molecular vibrations and localized surface plasmon resonance of faceted metal oxide nanocrystals.* Nano Letters, 2017. **17**(4): p. 2611-2620.

14. Johns, R.W., et al., *Charge carrier concentration dependence of ultrafast plasmonic relaxation in conducting metal oxide nanocrystals.* Journal of Materials Chemistry C, 2017. **5**(23): p. 5757-5763.